1. Introduction

Tab. 1.1 Abbreviations of the most important characterization methods.

ADES	Angular Distribution Electron Spectroscopy
AES	Auger Electron Spectroscopy
AFM	Atomic Force Microscopy
APS	Appearance Potential Spectroscopy
ARUPS	Angular Resolved UV Photoelectron Spectroscopy
ATR	Attenuated Total Reflection
CEMS	Conversion Electron Mössbauer Spectroscopy
CTEM	Conventional Transmission Electron Microscopy
DRIFTS	Diffuse Reflectance Infrared Fourier Transform Spectroscopy
DRUV	Diffuse Reflectance Ultraviolet Spectroscopy
DSC	Differential Scanning Calorimetry
DTA	Differential Thermal Analysis
EDX	Energy Dispersive X-Ray
EELS	Electron Energy Loss Spectroscopy
ELNES	Energy Loss Near Edge Structure
ENDOR	Electron Nuclear Double Resonance
EPR/ESR	Electron Paramagnetic/Spin Resonance
ESCA	Electron Spectroscopy for Chemical Analysis
ESD	Electron Simulated Desorption
ESEM	Electron Spin Echo Microscopy
EXAFS	Extended X-Ray Absorption Fine Structure
EXELFS	Extended X-Ray Electron Loss Fine Structure
FABMS	Fast Atom Bombardment Mass Spectroscopy
FEM	Field Emission Microscopy
FIM	Field Ion Microscopy
FIR	Far Infrared
FMR	Ferromagnetic Resonance
FTIR	Fourier Transform Infrared
GNR	Gamma Nuclear Resonance
HREELS	High-Resolution Electron Energy Loss Spectroscopy
HREM	High-Resolution Electron Microscopy
INS	Inelastic Neutron Scattering
IR	Infrared
ISS	Ion Scattering Spectroscopy

LAMMA	Laser Microprobe Mass Analysis
LEED	Low-Energy Electron Diffraction
LIF	Laser Induced Fluorescence
LRS	Laser Raman Spectroscopy
MAS-NMR	Magic Angle Spinning Nuclear Magnetic Resonance
MES	Mössbauer Emission Spectroscopy
MS	Mass Spectroscopy
NMR	Nuclear Magnetic Resonance
ND	Neutron Diffraction
NQD	Nuclear Quadrupolar Resonance
PAS	Photoacoustic Spectroscopy
PES/PS	Photoelectron Spectroscopy
RBS	Rutherford Backscattering Spectroscopy
RED	Radial Electronic Distribution
SAM/SAEM	Scanning Auger Electron Microscopy
SANS	Small-Angle Neutron Scattering
SAXS	Small-Angle X-Ray Scattering
SEM	Scanning Electron Microscopy
SEXAFS	Surface Extended X-Ray Absorption Fine Structure
SEXELFS	Surface Extended X-Ray Electron Loss Fine Structure
SIMS	Secondary Ion Mass Spectroscopy
STEM	Scanning Transmission Electron Microscopy
STM	Scanning Tunnel Microscopy
TEM	Transmission Electron Microscopy
TG	Thermogravimetry
TPD, TPO, TPR	Temperature Programmed Desorption/Oxidation/Reduction
TDS	Thermal Desorption Spectroscopy
UPS	Ultraviolet Photoelectron Spectroscopy
UV-Vis	Ultraviolet–Visible Spectroscopy
XANES	X-Ray Absorption Near Edge Spectroscopy
XAS	X-Ray Absorption Spectroscopy
XRD	X-Ray Diffraction
XPS	X-Ray Photoelectron Spectroscopy

Tab. 1.2 Classification of characterization methods according to the incident and emitted beams and particles.

Emitted beams	Incident beams					
	Neutral	Ions	Electrons	Photons	Thermal effect	Magnetic, electric fields or sonic wave
Neutral	INS			Photo-desorption	TPD TG	
Ions	FABMS	SIMS ISS				FIM
Electrons			TEM, Electron diffraction, STEM, SEM AES, EELS, HREELS LEED	ADES, ESCA or XPS, PES PS, UPS		FEM
Photons			APS, EDX, microprobe	ATR, UV-Visible, IR, FTIR, Raman, Mössbauer, (GNR), XRD, EXAFS/XANES		
Thermal effect, magnetic, electric fields or sonic wave	Calorimetry			PAS	DSC DTA	FMR, ENDOR, EPR, NMR, Magnetism, Electric conductivity, STM, AFM

Interaction of probes with:	Incident probe					
	Radiation ions	X-rays electrons	Photons			
	Nuclei	Electrons inner layer	Electrons outer layer	Molecules	Electron spin	Nuclear spin
Energy (eV)	10^9 10^7	10^5 10^3	10^1	10^{-1}	10^{-3} 10^{-5}	10^{-7}
Wavelength (μm)	10^{-8}	10^{-3}	10^{-2}	10^2	10^4	
Techniques	SIMS-ISS Mössbauer	ESCA, XPS AES, Electron diffraction Electron microscopy Microprobe EXAFS, EELS	UV-visible UPS, LEED APS	IR PAS Raman	Microwave EPR	NMR

Fig. 1.1 Ranges of energies and wavelengths for the most important characterization methods.

Tab. 1.3 Comparison of the parameters of the most important characterization methods.

| | Technique | | | | | | | |
| | Molecular spectroscopy | | | Resonances | | | | |
Characteristic	IR PAS	Raman	UV-visible	EPR FMR	NMR	Mössbauer	Neutrons	Thermal methods
Thickness analyzed	mm	mm	mm	mm	mm	100 μm	0.1 mm	mm
Area analyzed	cm^2	μm^2	cm^2	cm^2	cm^2	cm^2	mm^2	mm^2
Sample degradation	no	possible	no	no	no	no	possible	possible
Sample preparation	easy	easy	easy	easy	easy	easy	difficult	easy
Quantitative measurements	possible	possible	possible	yes	yes	yes	yes	yes
Gaseous atmosphere	yes	yes	yes	yes	yes	yes	yes	possible
Temperature range (°C)	$\frac{-196}{300}$	$\frac{-196}{300}$	$\frac{-196}{300}$	$\frac{-269}{1000}$	$\frac{-196}{200}$	$\frac{-269}{400}$	$\frac{-269}{800}$	No limit
Information	functional groups	functional groups	degree of oxidation	para. species	functional groups	degree of oxidation	adsorbing species	energies of formation and adsorption
	adsorbing species	adsorbing species	ion symmetry	degree of oxidation		symmetry of environment	atomic structure	
			adsorbing species	symmetry				

| | Surfaces | | | | X rays | | | | |
Characteristic	EELS	XPS	AES	SIMS	Diffr.	EXAFS	Radial distribution	Magnetism	Electrical conductivity
Thickness analyzed	μm	20–50 Å	10–20 Å	2–3 Å	mm	mm	mm	mm	mm
Area analyzed	cm^2	cm^2	cm^2	cm^2	mm^2	mm^2	mm^2	cm^2	cm^2
Sample degradation	very small	possible	possible	no	no	no	no	no	no
Sample preparation	difficult	easy	easy	easy	easy	easy	easy	easy	easy
Quantitative measurements	—	yes	possible	possible	yes	yes	yes	yes	yes
Gaseous atmosphere	no	difficult	difficult	no	yes	yes	yes	possible	possible
Temperature range (°C)	ambient	$\frac{-180}{600}$	$\frac{-180}{600}$	ambient	$\frac{-196}{1000}$	$\frac{-196}{1000}$	$\frac{-196}{1000}$	$\frac{-271}{500}$	$\frac{-196}{800}$
Information	metal-ligand bonds	degree of oxid. surface composition	surface composition	surface composition	crystallite structure crystallite size	near environment number of ligands	near environment	magnetic degree crystallite size	conduction type ionosorbed species

2. Microscopy methods
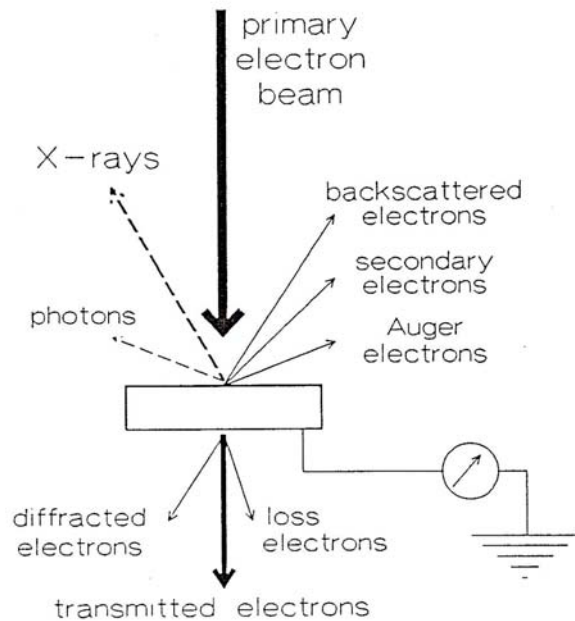
Fig. 2.1 Interactions between the primary electrons and the sample in an electron microscope.
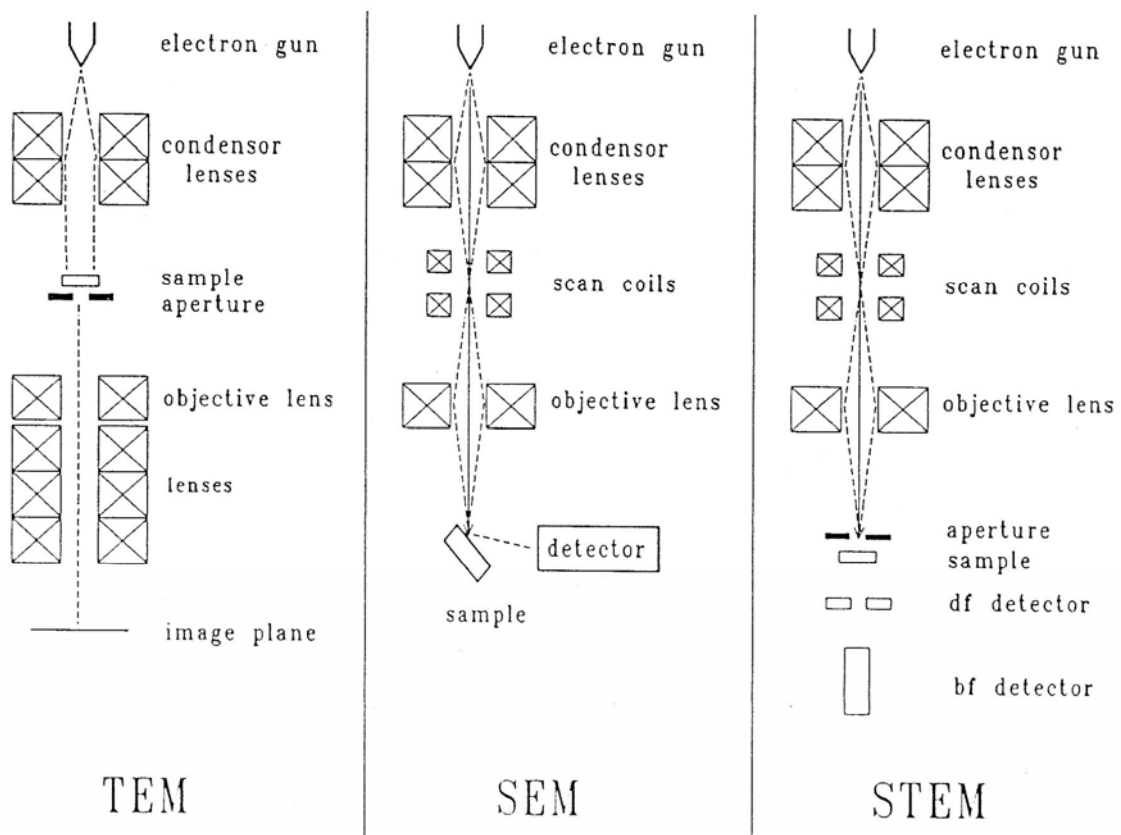
Fig. 2.2 Set up of electron microscopes working in the transmission (TEM), scanning (SEM), and combined mode (STEM).
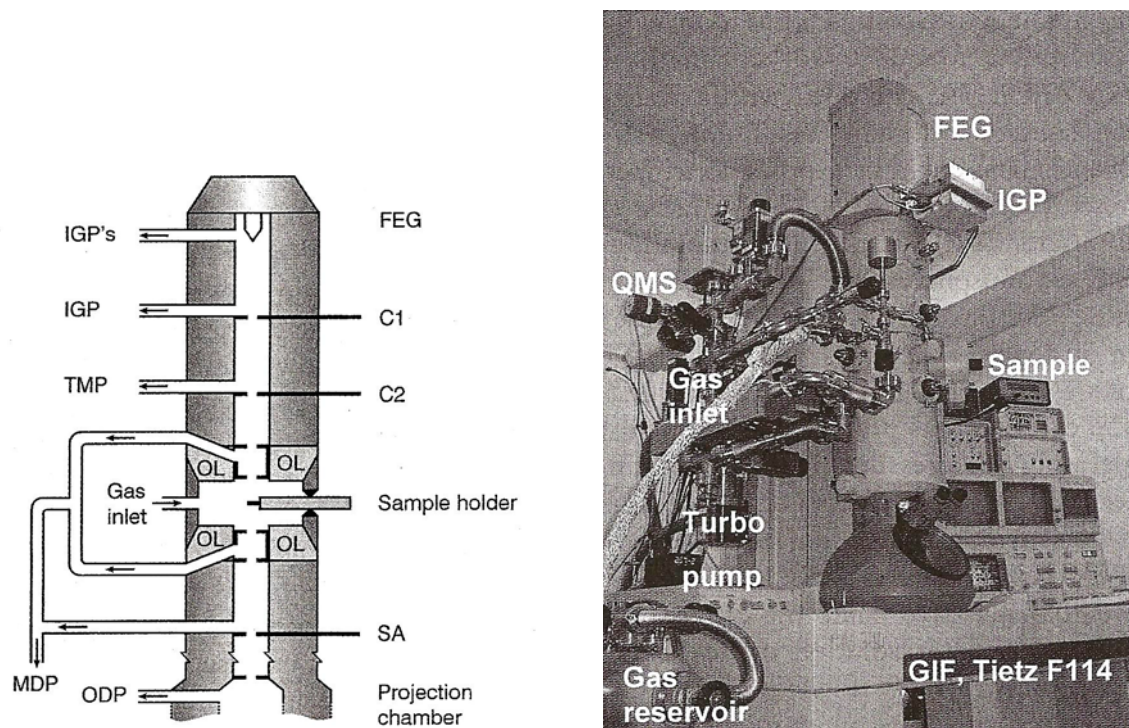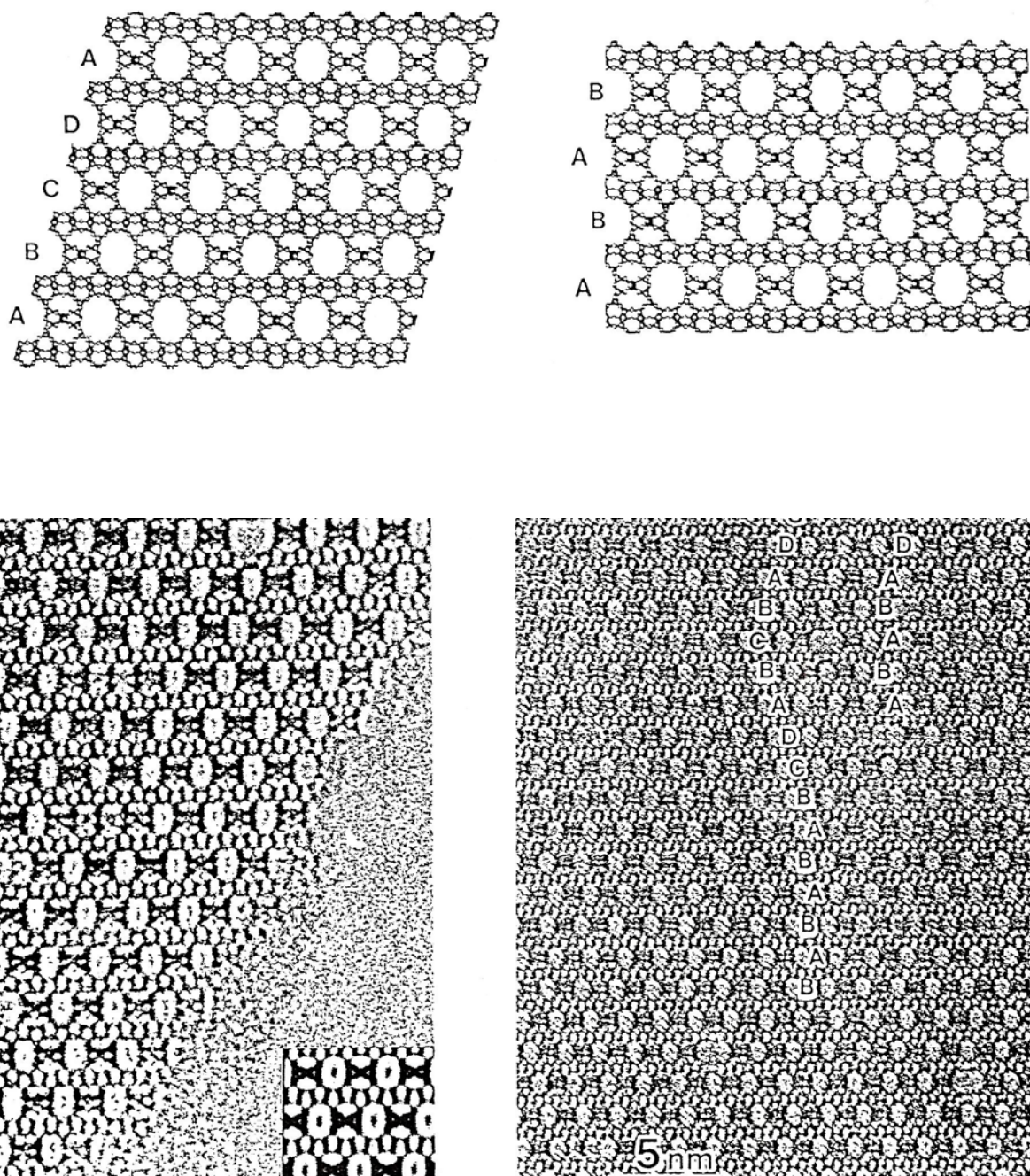
Fig. 2.3 Scheme and photo of a HRTEM microscope equipped with a field emission gun (FEG), quadrupole mass spectrometer (QMS), Gatan image filter (GIF), and Tietz F144 CCD for data acquisition.
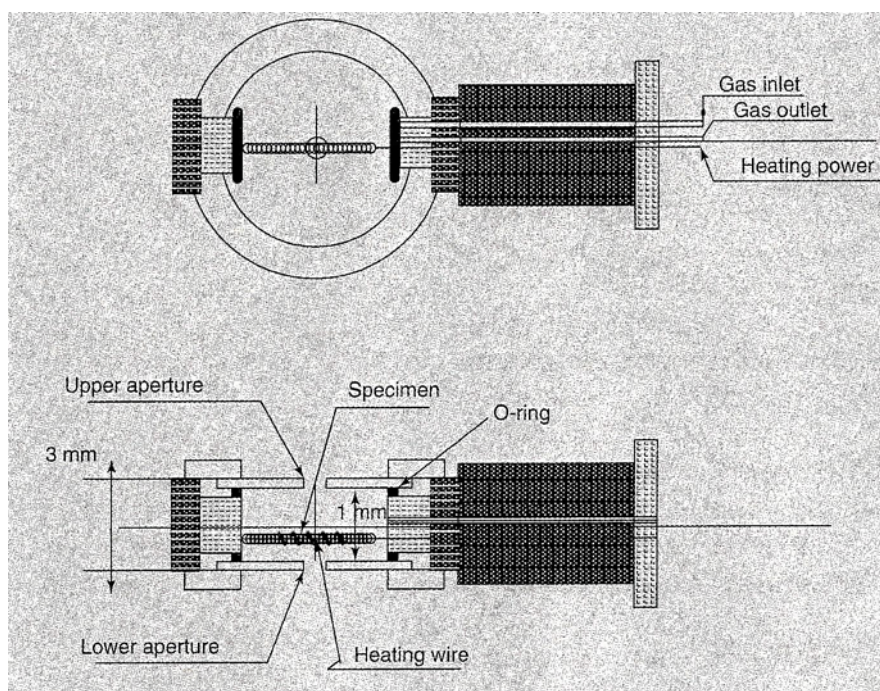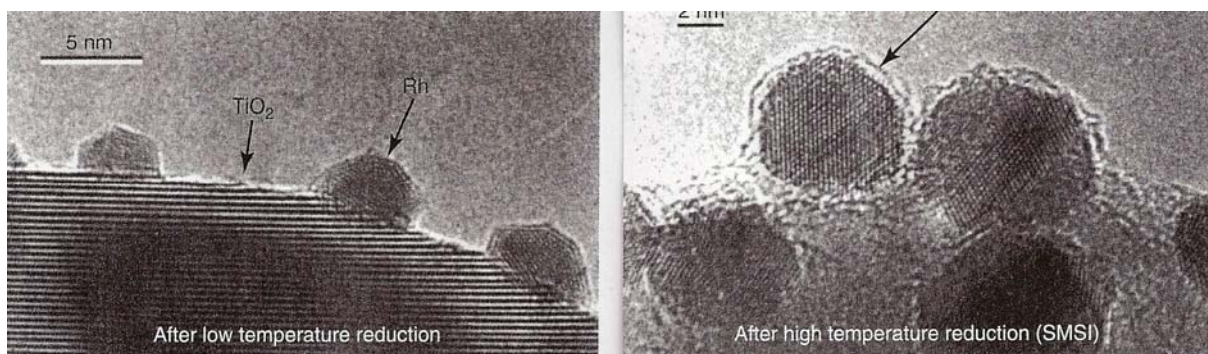

Fig. 2.4 Sample holder of a HRTEM microscope in top and profile view.

Fig. 2.5 Schemes (top) and SEM images (bottom) showing the stacking-sequence of zeolite ETS-10 (polymorph A: ABCD, polymorph B: ABAB).

Fig. 2.6 HRTEM image of Rh/TiO$_2$ after low temperature (473 K) reduction (left) and high temperature (773 K) reduction (right). In the latter case, the Rh particles are covered with amorphous overlayers.
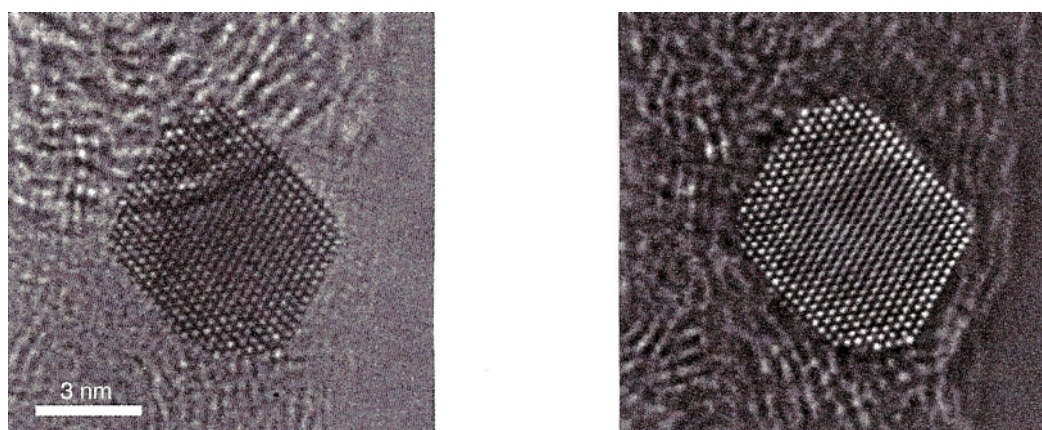
Fig. 2.7 HRTEM image of a Pt particle on amorphous carbon acquired with a 200 kV microscope (left) and the aberration corrected image (right).
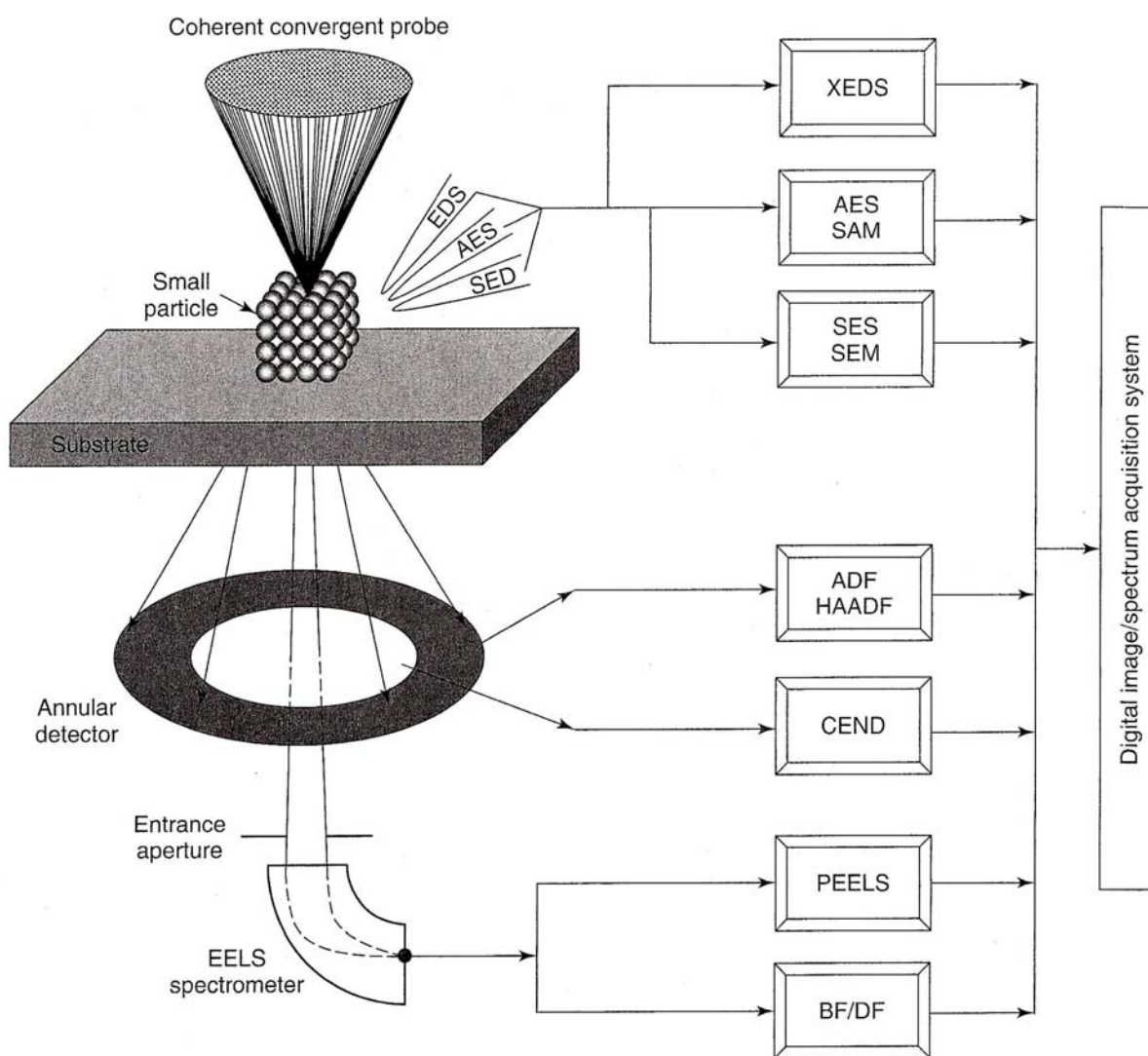
Fig. 2.8 Scheme of the various signals generated inside a transmission electron microscope suitable for producing high-resolution images and for chemical analysis (XEDS: X-ray energy-dispersive spectroscopy, AES: Auger electron spectroscopy, SAM: scanning Auger microscopy, SES: secondary electron spectroscopy, SEM: secondary electron microscopy, ADF: annular dark-field, HAADF: high-angle annular dark-field, CEND: coherent electron nano-diffraction, PEELS: parallel electron energy-loss spectroscopy, BF: bright field, DF: dark field)
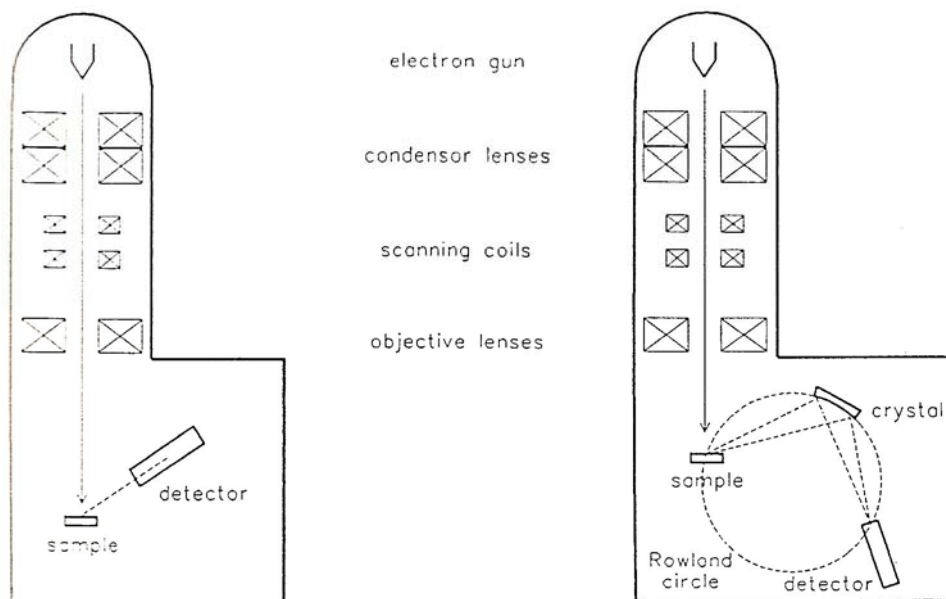
Fig. 2.9 Set up for measuring X-ray fluorescence with an energy-dispersive detector as in EDX (left) or with a wave-length dispersive spectrometer (right).
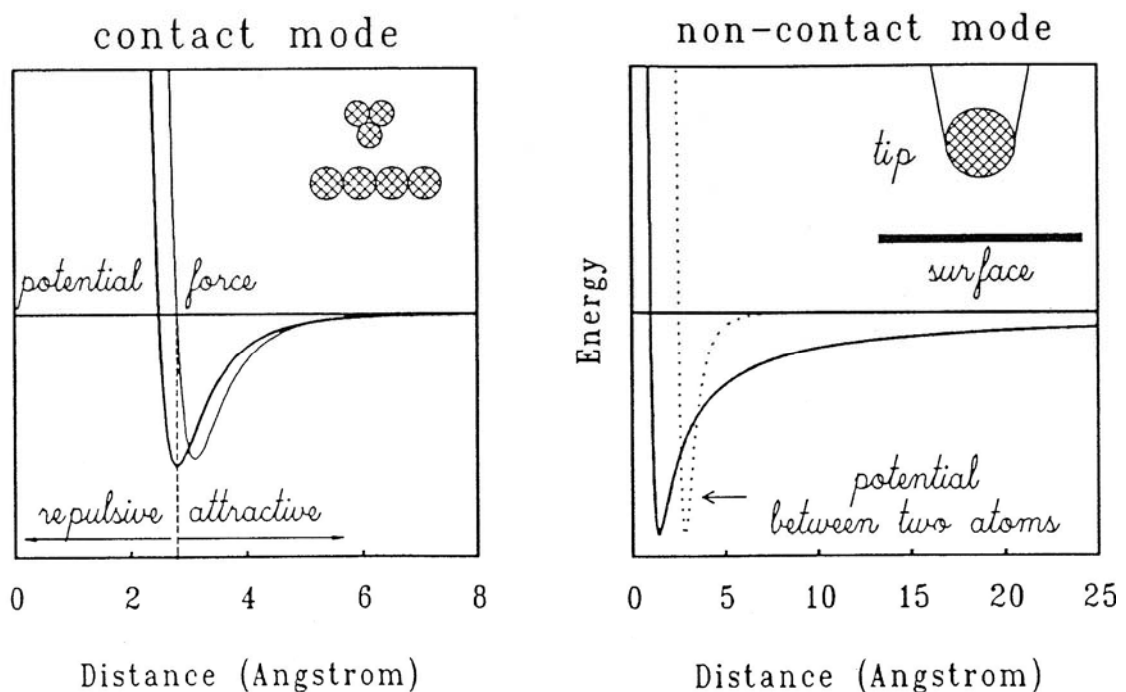
Fig. 2.10 Principles of atomic force microscopy (AFM): Contact mode (left) with sharp tip and non-contact mode (right) with spherical tip. In the latter case, the dotted curve corresponds to the Lennard-Jones interaction potential between two atoms.
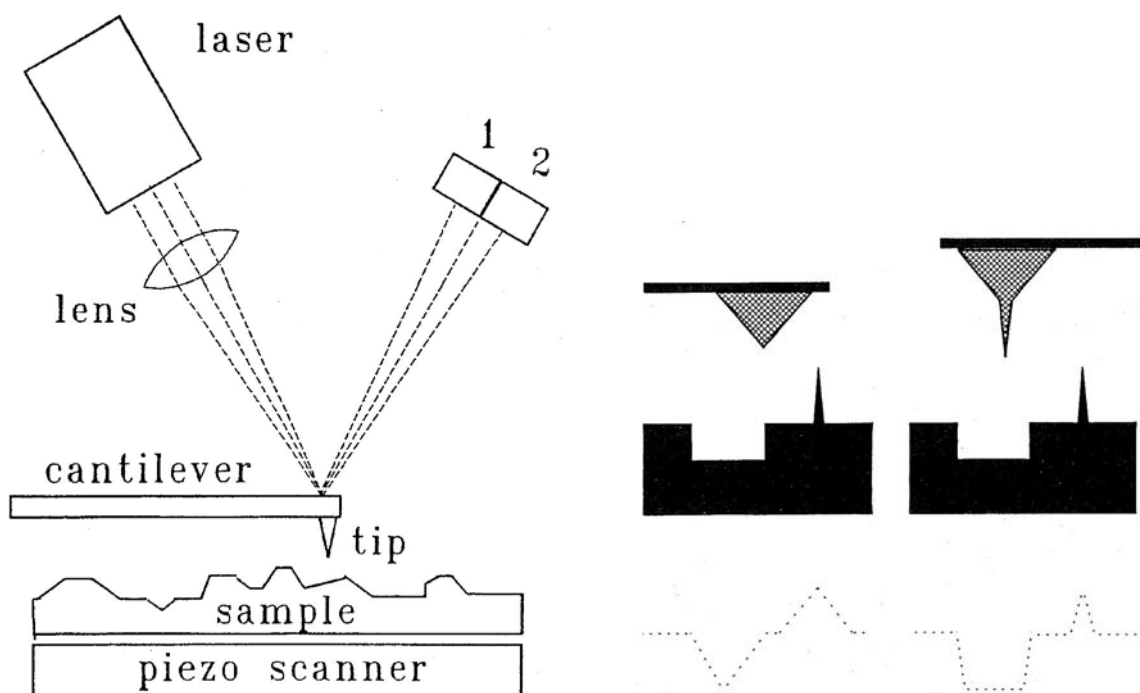
Fig. 2.11 Set up of an atomic force microscope (left) and effect of the tip shape on the obtained images (right). The blunt tip is suitable to image the morphology of rough particles, while the sharp tip is utilized to make images with atomic details.
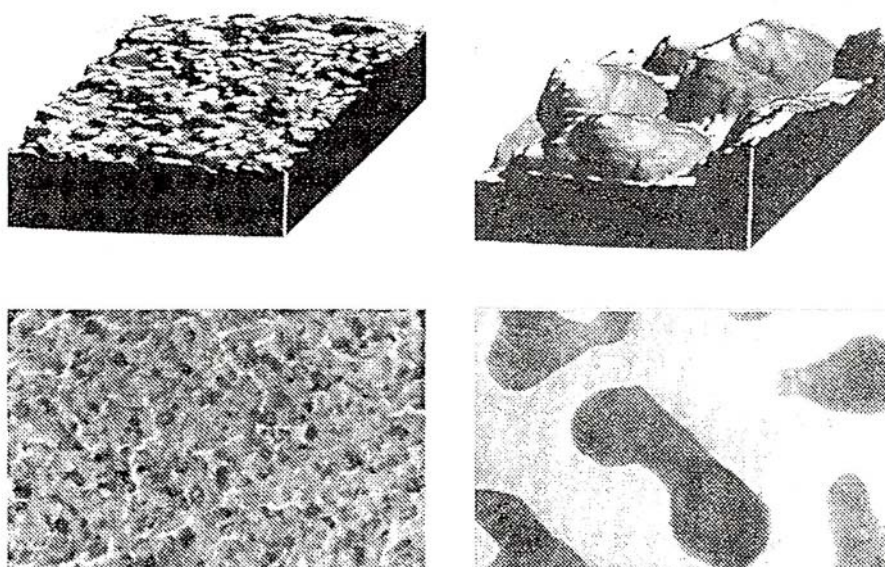
Fig. 2.12 AFM (top) and TEM (bottom) images of platinum particles on a flat SiO_2 layer obtained before (left) and after (right) heating in oxygen and hydrogen at 475 K.
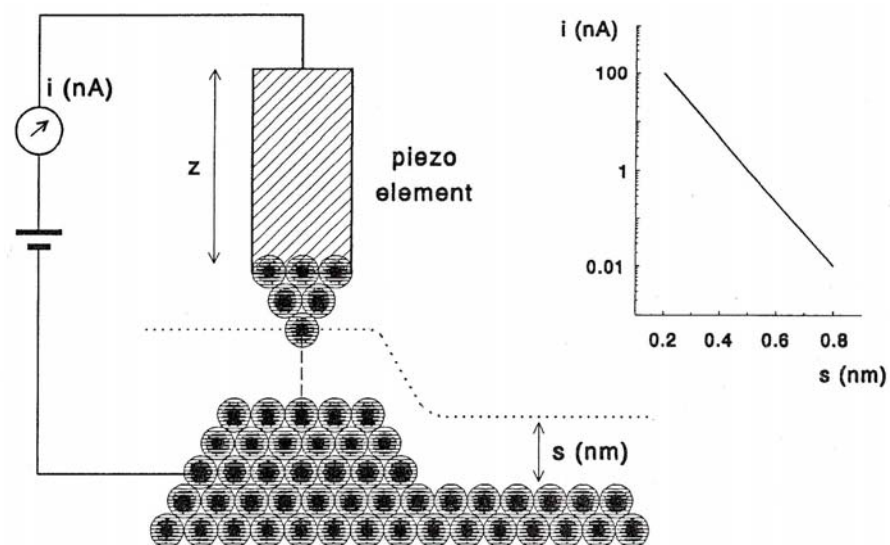
Fig. 2.13 Principle of scanning tunnelling microscopy (STM) basing on the tunnelling of electrons between the surface and an atomically sharp tip (left). A control system keeps the tunnelling current constant (right) via regulating the tip-surface distance.
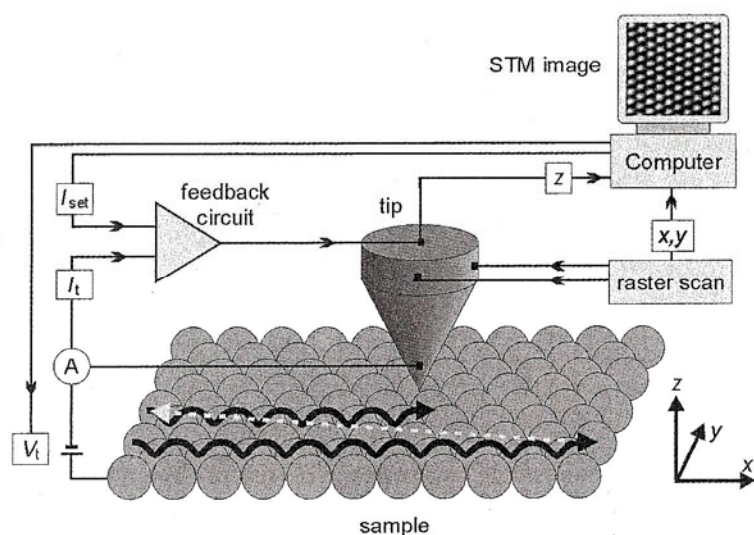
Fig. 2.14 Scheme of a scanning tunnelling microscope (STM).
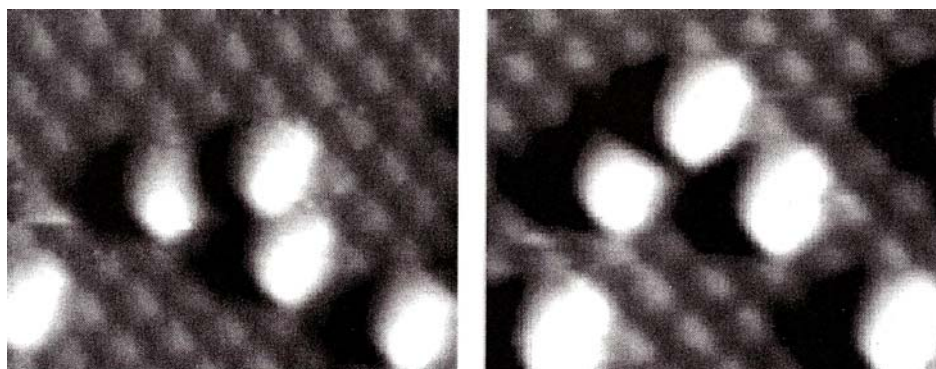
Fig. 2.15 STM images of an Pd(111) surface covered with H atoms. The bright spots are moving H vacancies.

3. Diffraction methods
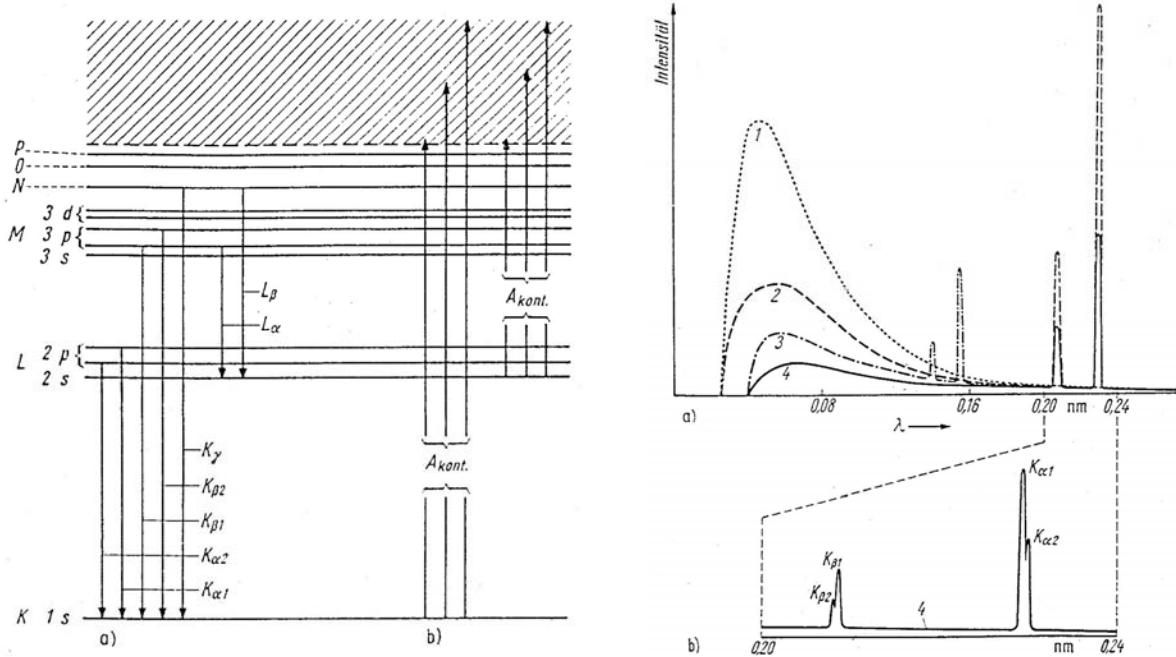
Fig. 3.1 Energy levels, resulting X-ray emissions due to electron transitions (a, left) and X-ray absorption (b, left). On the right-hand side, X-ray spectra of (1) tungsten (1), chromium (2), copper (3), and chromium (4) are shown.
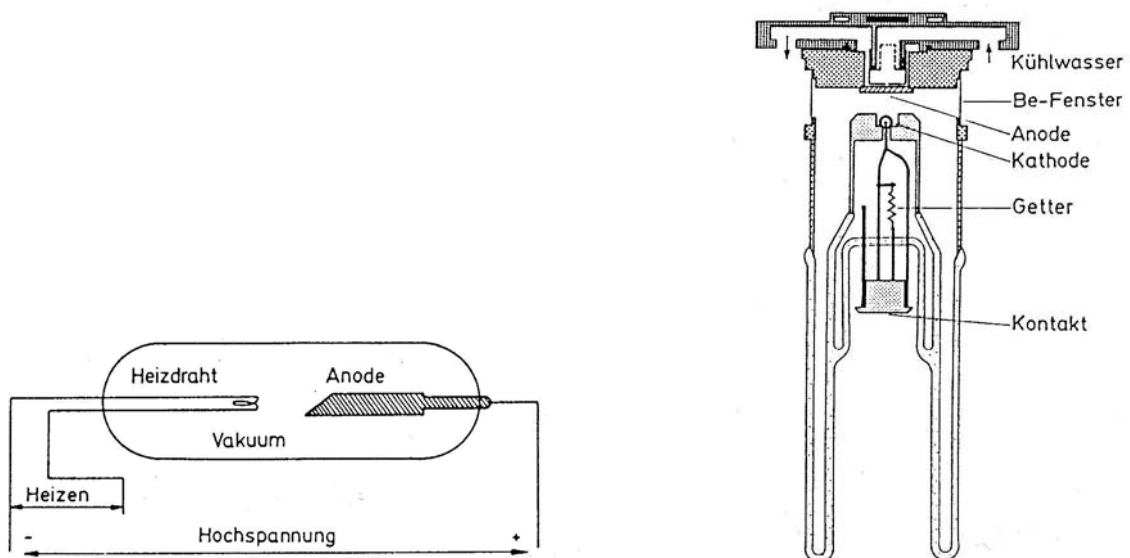
Fig. 3.2 Scheme (left) and construction of a X-ray tube (right).

Tab. 3.1 Materials used for anodes of X-ray tubes.

Element	Z	λ_{ch} in nm			U_{min} in kV	λ_{AK} in nm	Filter[1]
		$K_{\alpha 1}$	$K_{\alpha 2}$	K_β			
W	74	0,0209	0,0214	0,0184	69,3	0,0178	Hf
Ag	47	0,0559	0,0564	0,0497	25,5	0,0485	Rh
Mo	42	0,0709	0,0714	0,0632	20,0	0,0620	Zr
Cu	29	0,1541	0,1544	0,1392	9,0	0,1380	Ni
Ni	28	0,1658	0,1662	0,1500	8,3	0,1487	Co
Co	27	0,1789	0,1793	0,1621	7,7	0,1607	Fe
Fe	26	0,1936	0,1940	0,1757	7,1	0,1743	Mn
Cr	24	0,2290	0,2294	0,2085	6,0	0,2070	V

$$n\lambda = 2d\sin\theta$$
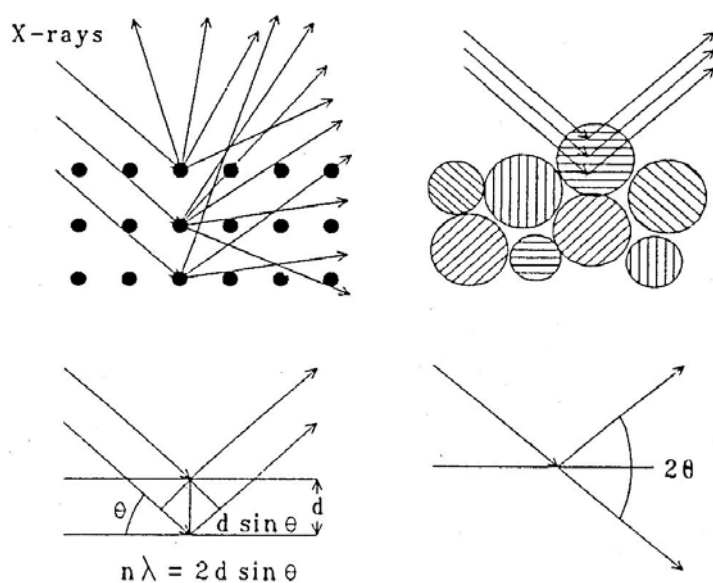
Fig. 3.3 Scheme of X-rays scattered by atoms in an ordered lattice.
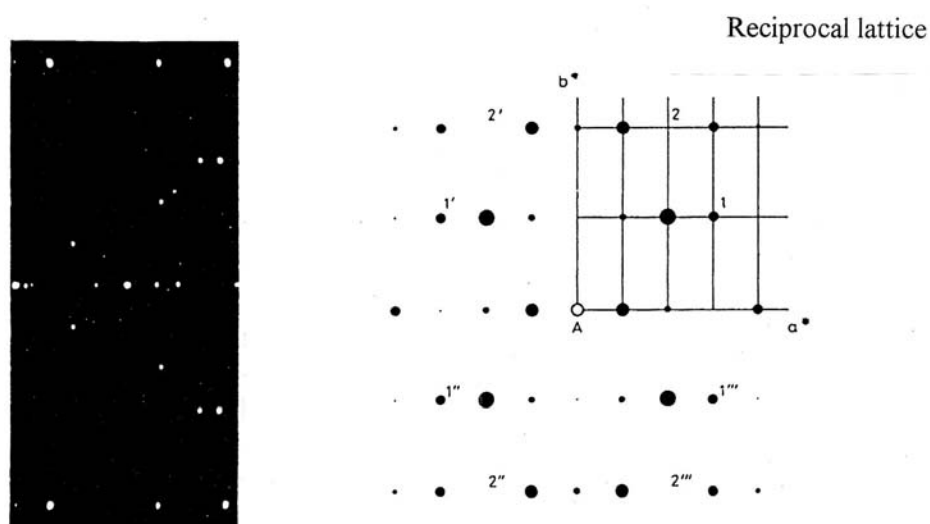
Fig. 3.4 Laue diagram of X-ray reflections (left) on a single crystal (ZSM-5) and scheme of a reciprocal lattice (right).

Fig. 3.5 Scheme of the reflections obtained for powder (random orientation) X-ray diffraction leading to circles at angles of 2 ν.

Fig. 3.6 Set up for recording X-ray powder diffraction by the Debye-Scherrer method.

Fig. 3.7 Film obtained for powder X-ray diffraction according to the Debye-Scherrer method.
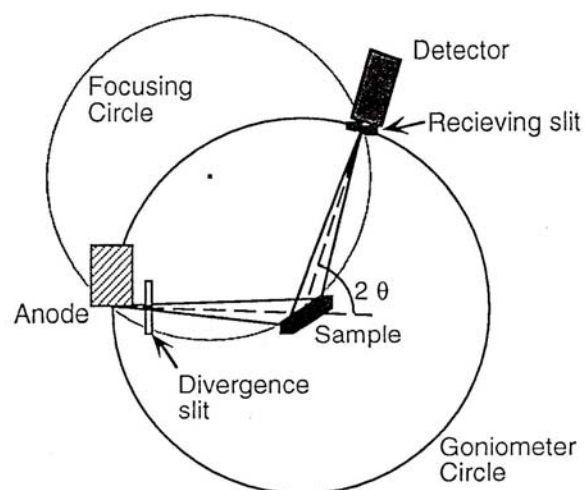
Fig. 3.8 Bragg-Brentano geometry of a powder X-ray diffractometer.
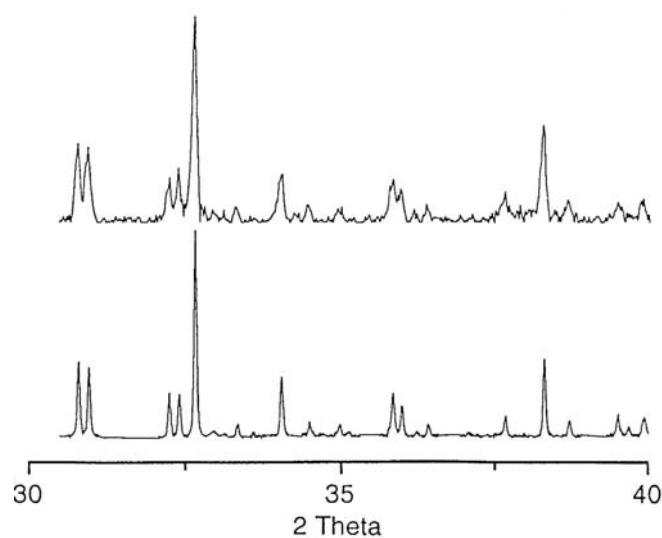
Fig. 3.9 Comparison of powder diffraction data collected on a well-calibrated laboratory (top) and a synchrotron facility (bottom).
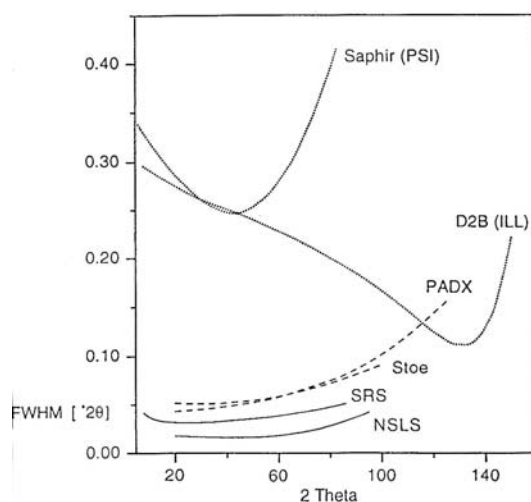
Fig. 3.10 Full width at half maximum (FWHM) of reflections measured at several diffractometers. The solid curves were obtained via synchrotrons, while the dashed curves were due to neutron instruments.
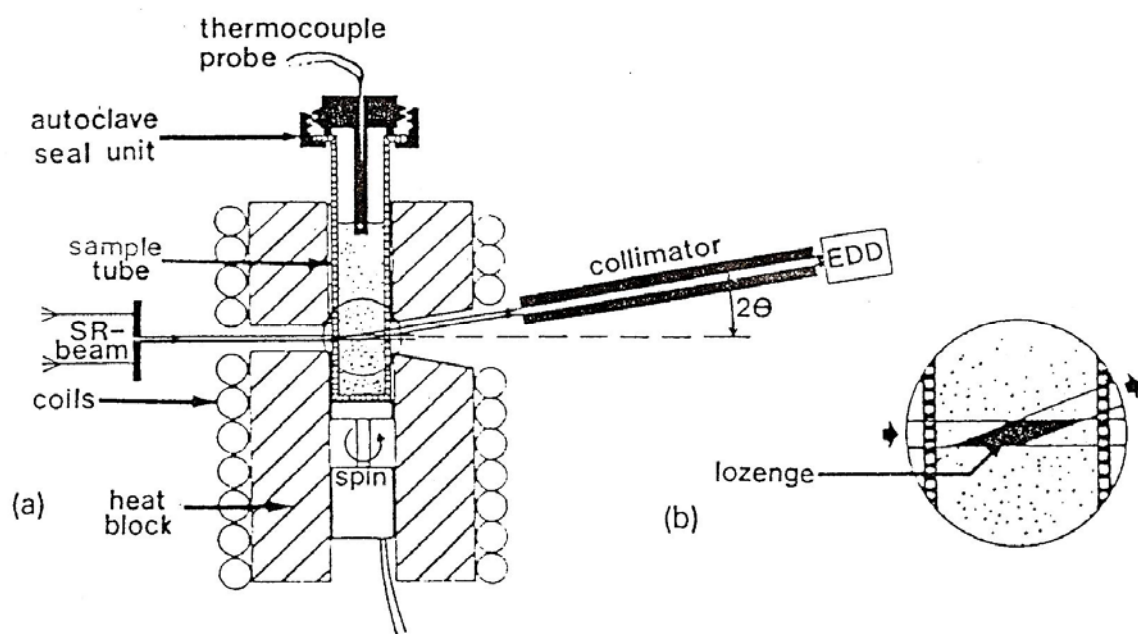
Fig. 3.11 Set up of an X-ray cell used for studying the synthesis and phase transitions of materials (a) at a synchrotron (SR) via an energy-dispersive detector (EDD). The enlarged region (b) shows the volume within the sample tube, where the X-rays are diffracted.
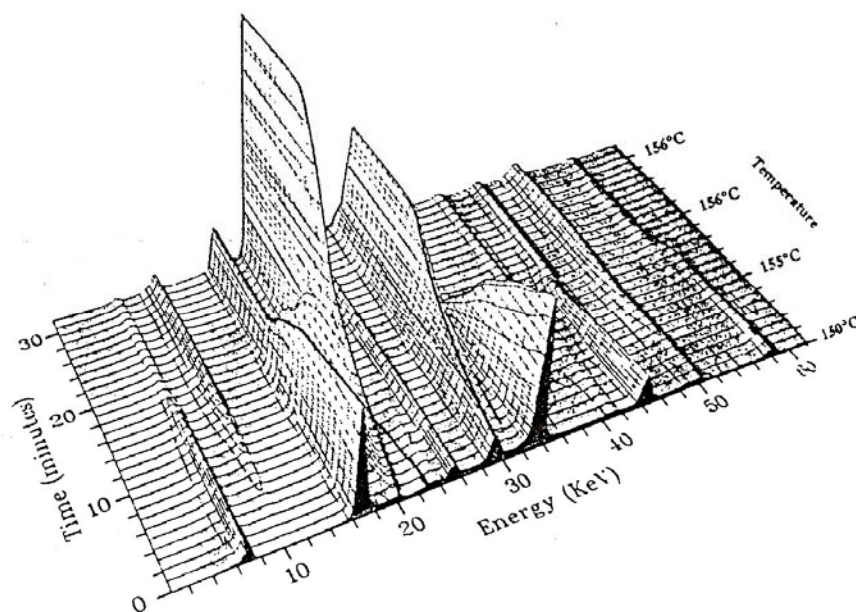
Fig. 3.12 In situ SR-EDD investigation of the transformation of an aluminophosphate VPI-5 to $AlPO_4$-8.
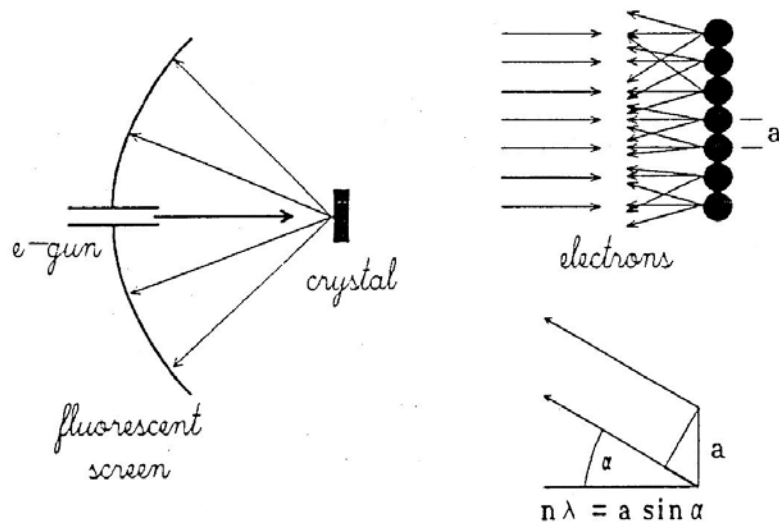
Fig. 3.13 Principle of low energy electron diffraction (LEED) of a beam of mono-energetic electrons. The directions of the interferences are made visible on a fluorescence screen.

definition: $\vec{a}_i \cdot \vec{a}_j^* = \delta_{ij}$

directions: $\vec{a}_1^* \perp \vec{a}_2 \; ; \; \vec{a}_2^* \perp \vec{a}_1$

length: $|\vec{a}_i^*| = \dfrac{1}{|\vec{a}_i| \cdot \sin\gamma}$

angle: $\angle(\vec{a}_1^*, \vec{a}_2^*) = 180^0 - \gamma$

area unit cell: $A^* = |\vec{a}_1^* \times \vec{a}_2^*|$

$= \dfrac{1}{|\vec{a}_1 \times \vec{a}_2|} = \dfrac{1}{A}$
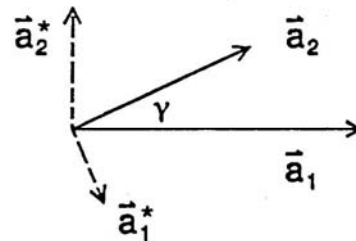
Fig. 3.14 Definition and properties of the reciprocal lattice with basis vectors marked by *.
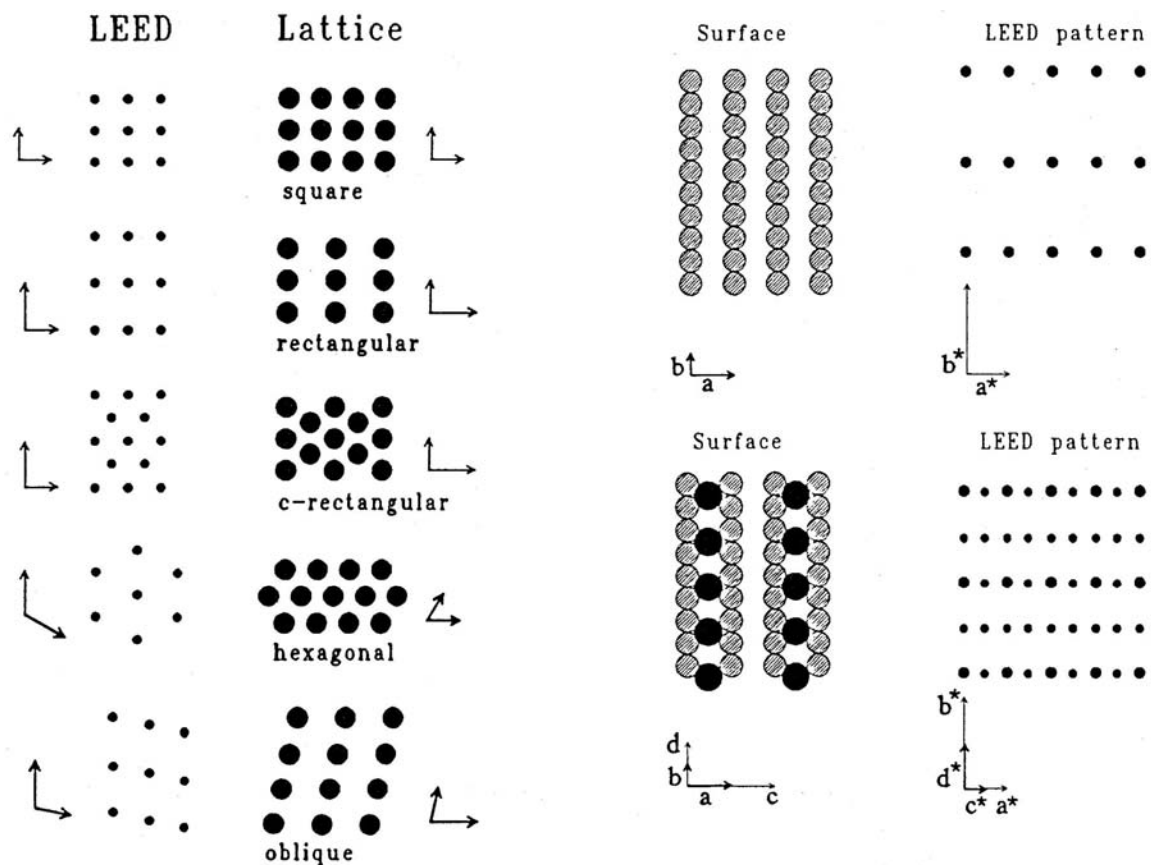
Fig. 3.15 Five different surface lattices with basis vectors of the real and reciprocal lattices (left) and a hypothetical surface covered by an ordered adsorbate layer with the corresponding LEED patterns (right).
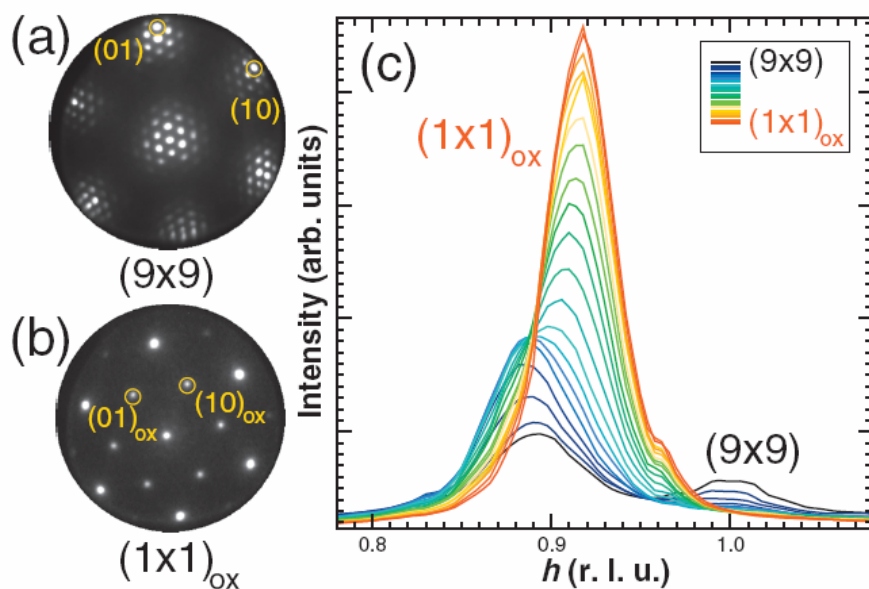
Fig. 3.16 In situ LEED patterns obtained before (a) and after (b) the phase transition during the oxidation of rhodium with NO_2 (p = 1 x 10^{-5} Torr) at 790 K. In (c), the time-resolved evolution of the (01) reflex is shown.

Tab. 3.2 Neutron scattering length and coherent, incoherent as well as absorption cross sections (in barns) for some common elements.

Element	$\langle b \rangle$ $\times 10^{-14}$ m	σ_{coh}	σ_{inc}	σ_{abs}
H	-0.37	1.8	80	0.19
D	0.67	5.6	2	0
B	$0.53{-}0.02i$	3.54	1.7	426
C	0.66	5.6	0	0
N	0.94	11.01	0.49	1.1
O	0.58	4.23	0	0
Al	0.35	1.5	0	0.13
Si	0.42	2.2	0	0.1
V	-0.04	0.02	5.18	2.82
Ni	1.03	13.3	5.2	2.5
Cd	$0.51{-}0.70i$	3.3	2.4	1400
Pt	0.95	11.6	0.13	5.7

[a] σ_{abs} is proportional to λ, and it corresponds here to $\lambda = 1$ Å.
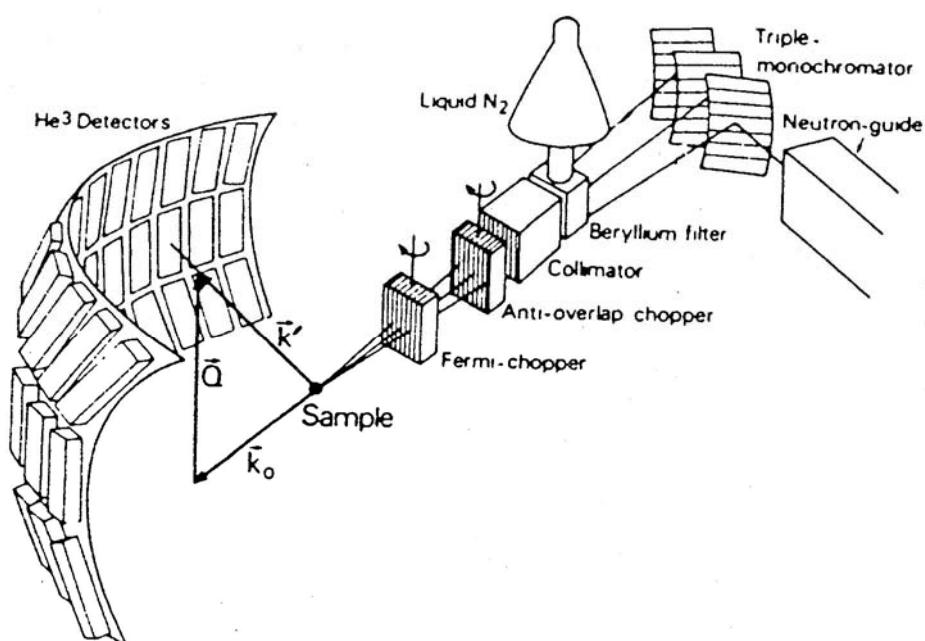
Fig. 3.17 Scheme of the time-of-flight neutron spectrometer IN6.
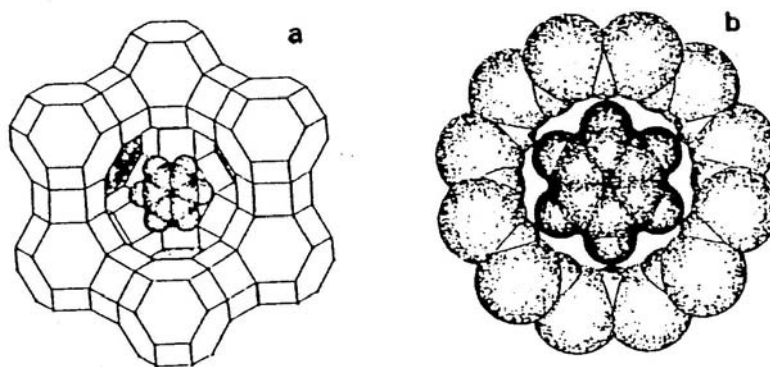
Fig. 3.18 Scheme showing two benzene molecules adsorbed inside the supercage (a) and the 12-ring window (b) of a zeolite Na-Y.
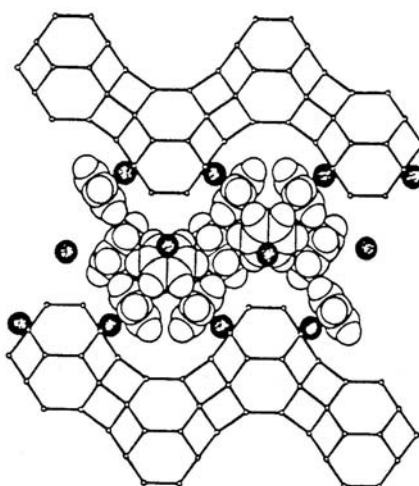
Fig. 3.19 Scheme of a zeolite Na-Y showing the clustering of adsorbed benzene molecules.
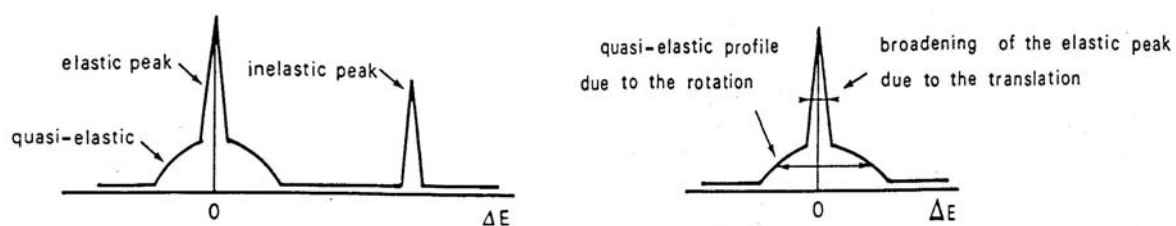
Fig. 3.20 Scheme of neutron reflections caused by elastic, quasi-elastic, and inelastic scattering.
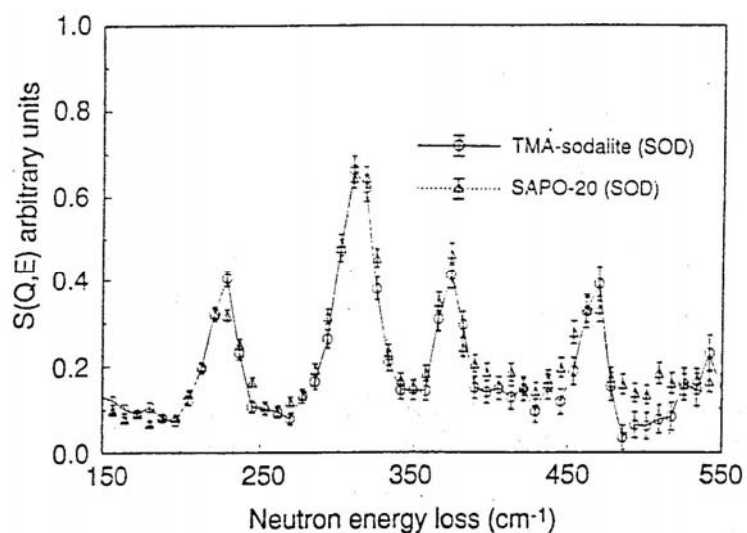
Fig. 3.21 Comparison of the INS spectra of tetramethylammonium cations (TMA$^+$) in the sodalite cages of an aluminosilicate-type sodalite and the silicoaluminophosphate SAPO-20.
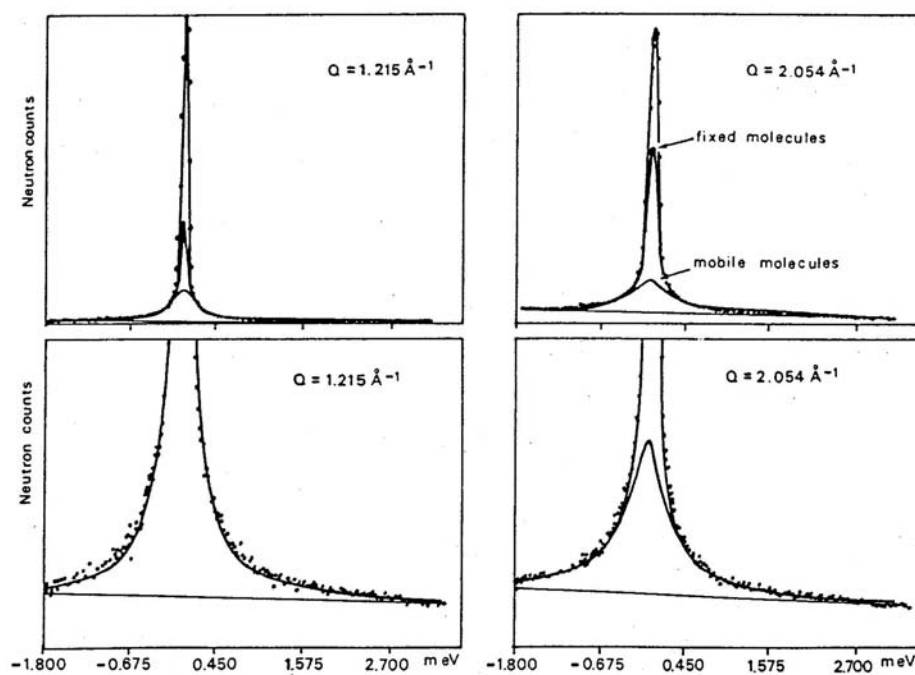
Fig. 3.22 QENS profiles of CH_3OH adsorbed in zeolite H-ZSM-5, recorded at 335 K with two different diffraction angles.

4. X-ray absorption spectroscopy (XAS)
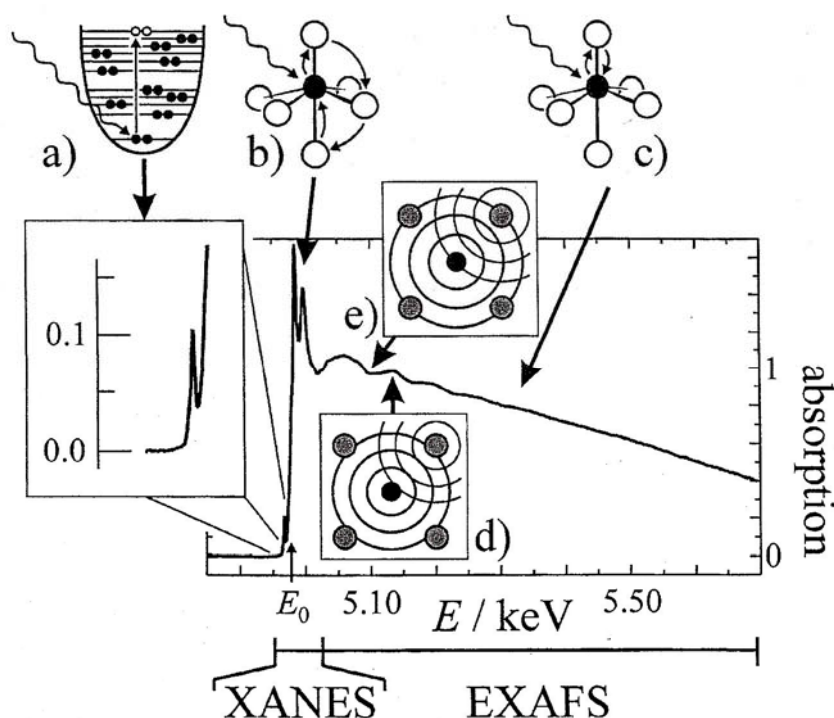
Fig. 4.1 Ti K edge X-ray absorption spectrum of the (dense) titanosilicate mineral aenigmatite in the XANES and EXAFS regions.
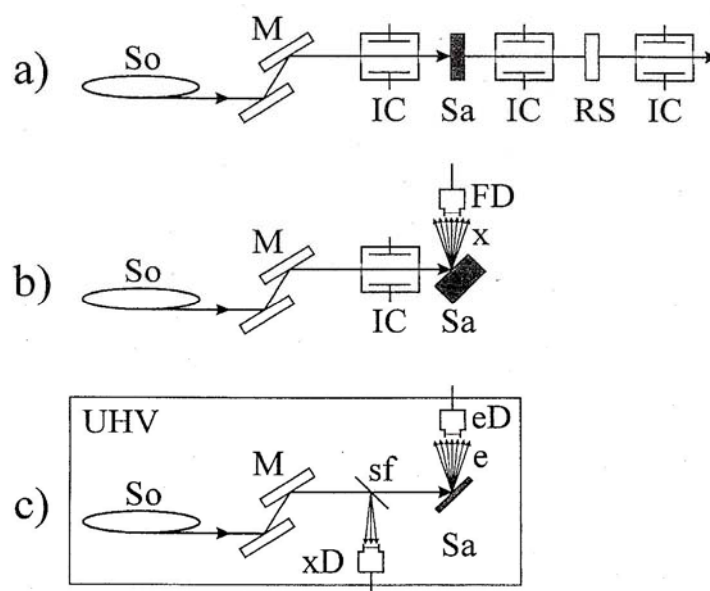
Fig. 4.2 Set ups for measuring XAS spectra: standard transmission experiment (a), fluorescence yield experiment (b), and electron yield experiment (c), the latter placed in a ultra-high vacuum chamber. So: synchrotron X-ray source, M: double-crystal monochromator, IC: ionization chamber, Sa: sample, RS: reference sample, x: fluorescence X-rays, FD: fluorescence detector, e: emitted electrons, eD: electron detector, sf: scattering foil, xD: X-ray detector for intensity calibration.
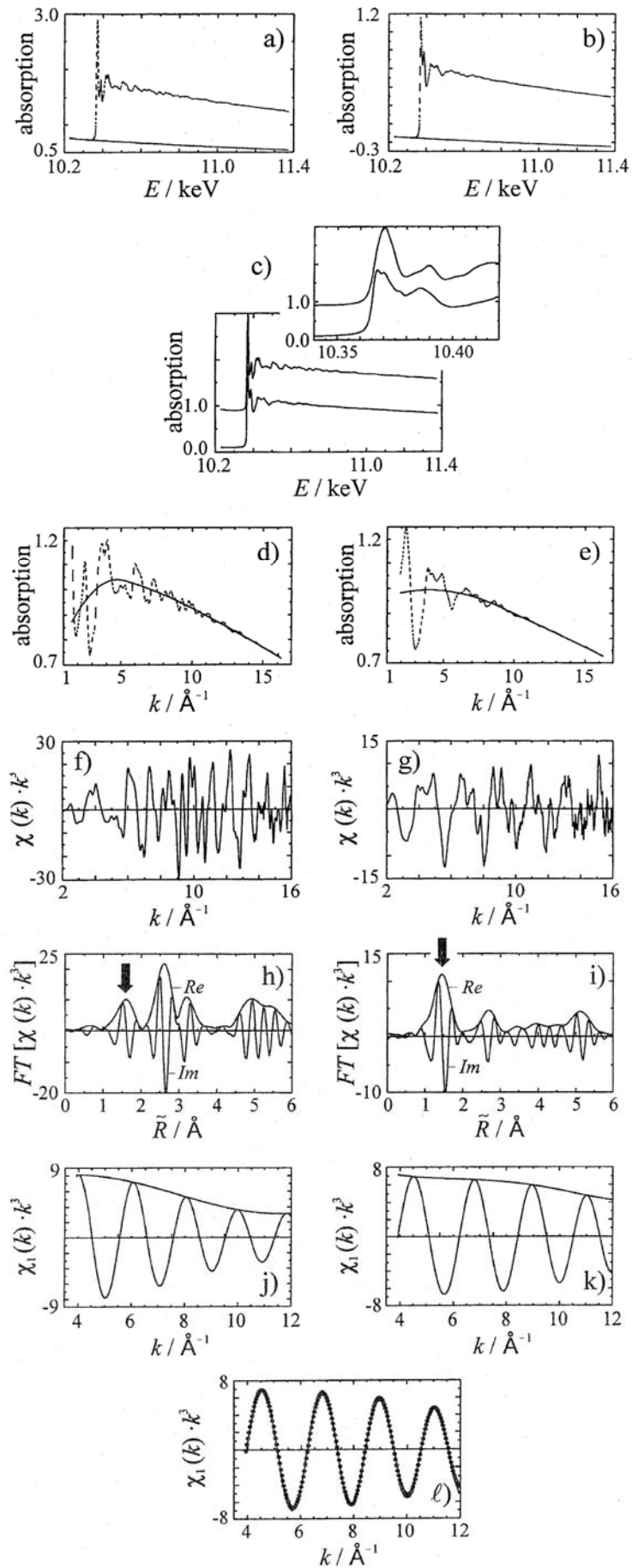
Fig. 4.3 Data analysis procedure for EXAFS studies of [Ga]-SOD and ZnGa$_2$O$_4$.
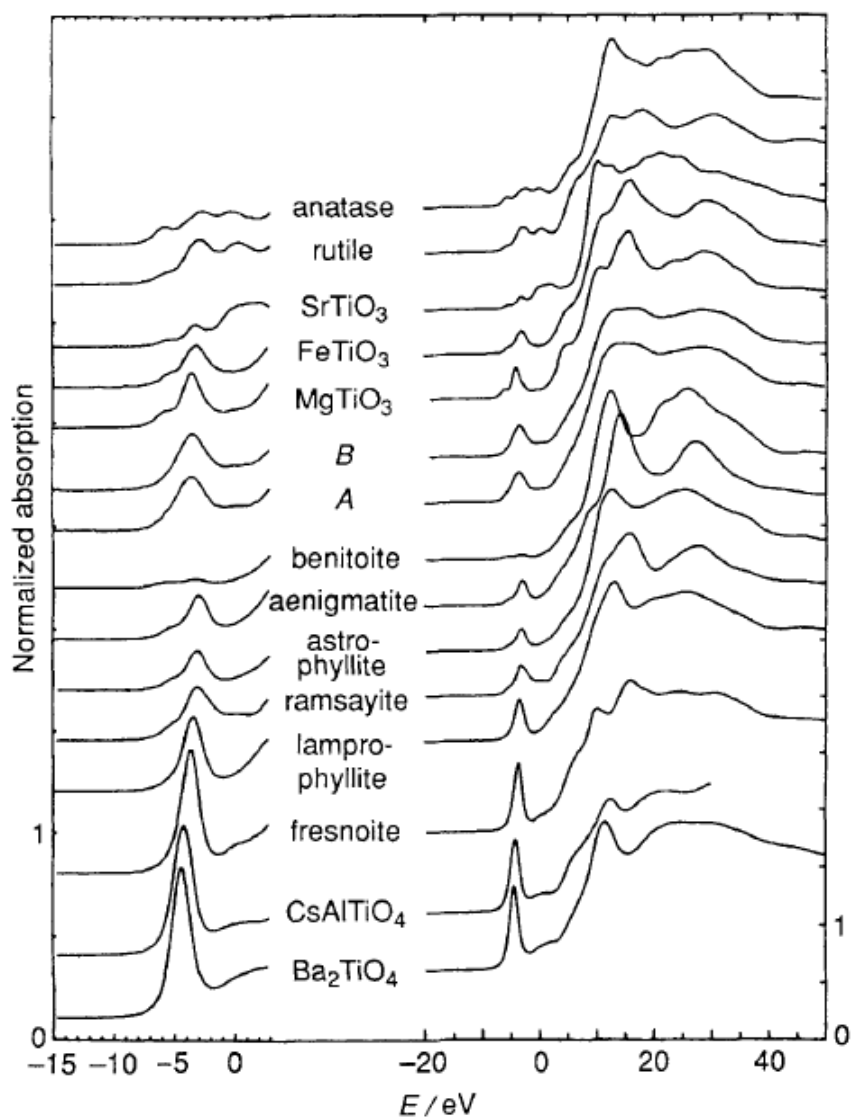
Fig. 4.4 Ti K edge XANES spectra of the titanosilicate TS-1 (samples A and B) together with those of reference compounds.
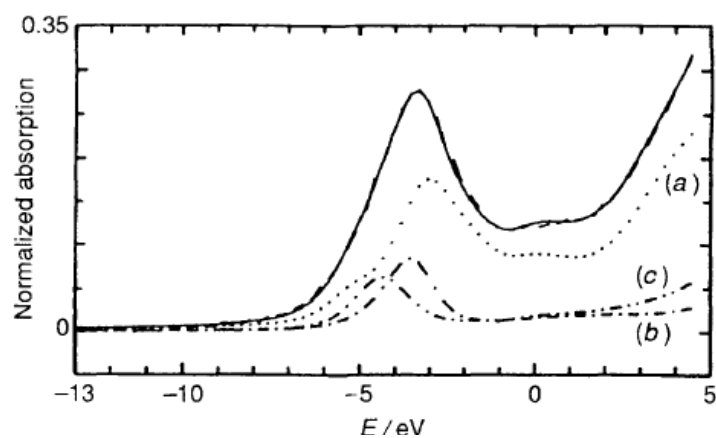
Fig. 4.5 Linear combination fit of the pre-peak region of the Ti K edge XANES spectra of titanosilicate TS-1 samples A and B (same shape) using the signals for octahedral coordination in ramsayite (a), square-pyramidal coordination in fresnoite (b), and tetrahedral coordination in Ba_2TiO_4 (c).
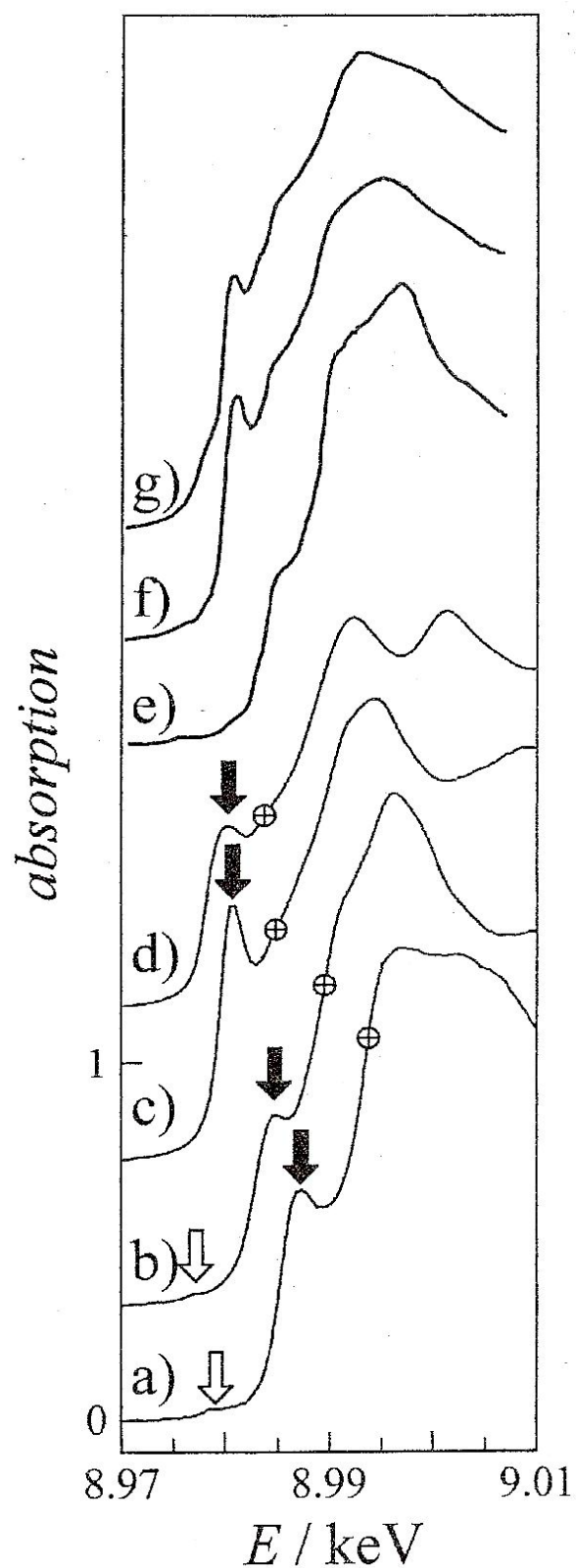
Fig. 4.6 Cu K edge XANES spectra of copper in different oxidation states in reference materials (a to d) and copper in zeolite Y (e to g). Reference materials are Cu^{3+} in $K_5[Cu(IO_5OH)_2]$ (a), Cu^{2+} in CuO (b), Cu^+ in Cu_2O (c), Cu^0 in elemental copper (d). For explanation of (e) to (g), see text.
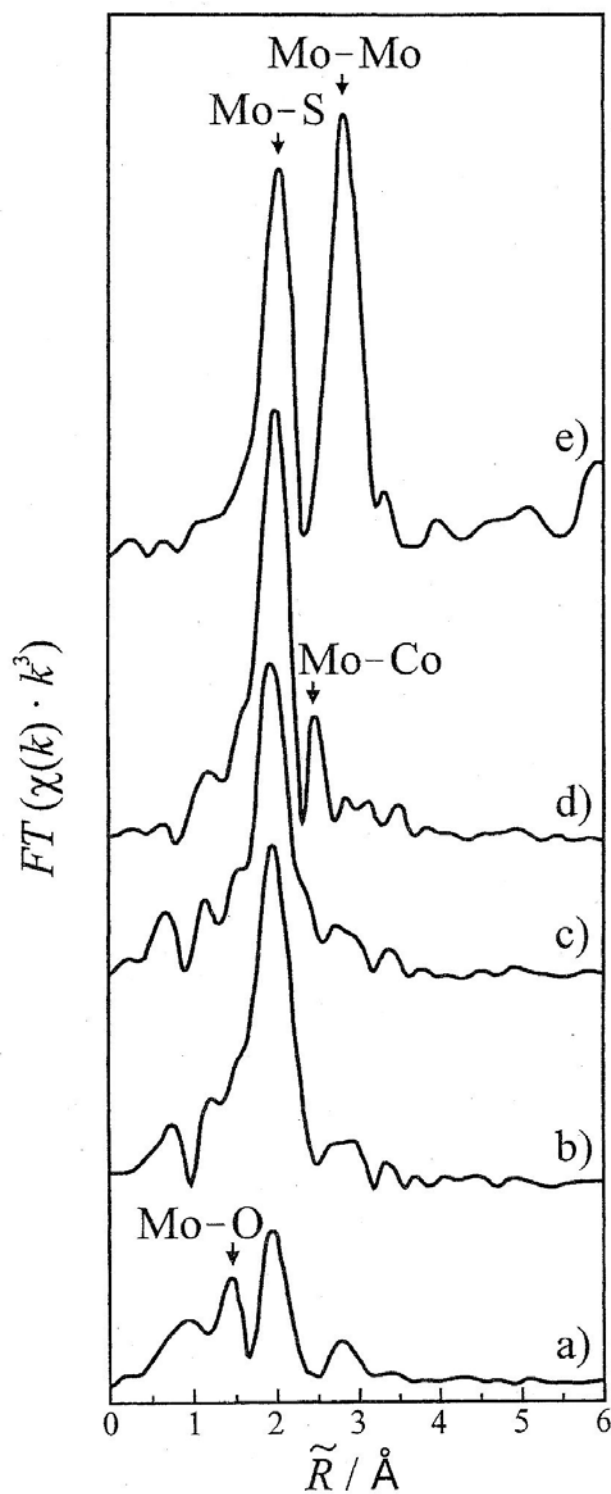
Fig. 4.7 Fourier transformed EXAFS functions of the Mo K edge of hydrodesulfurization catalysts and model compounds: Mo/S-Y zeolite prepared by impregnation (a), Mo/S-Y zeolite prepared by loading with $Mo(CO)_6$ (b), Fe/Mo/S-Y zeolite prepared by loading with $Mo(CO)_6$ and $Fe(CO)_5$ (c), Co/Mo/S-Y zeolite prepared by loading with $Mo(CO)_6$ and $Co(NO)(CO)_3$ (d), and polycrystalline MoS_2 (e).

Fourier transform of the EXAFS spectra
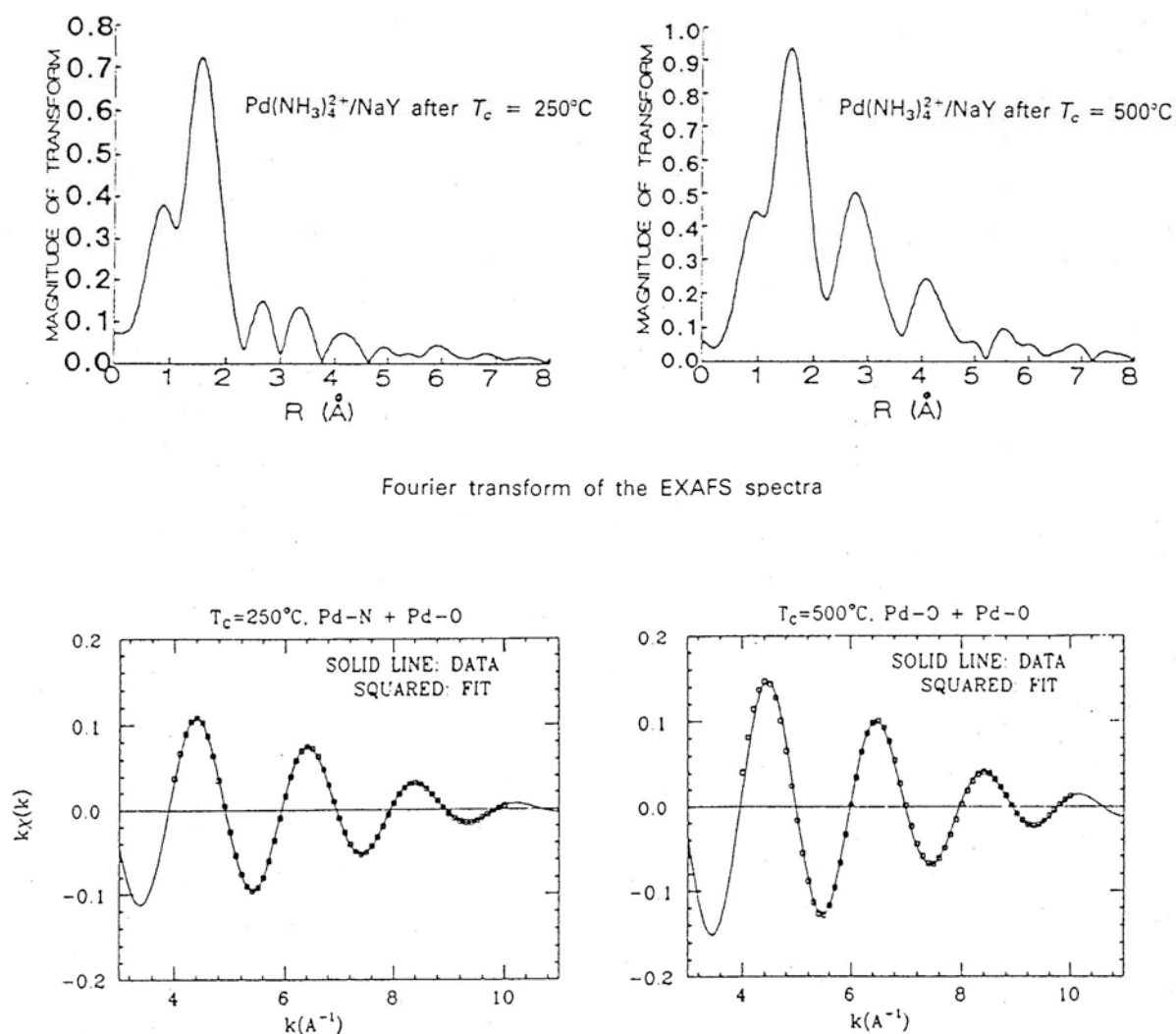
Fig. 4.8 Radial distribution functions (top) and fit of the back-transformed k^2-weighted EXAFS curves (bottom) obtained for zeolite Pd(NH$_3$)$_4^{2+}$/Na-Y upon treatment at 250°C (left) and 500°C (right).

Tab. 4.1 Results of the fit of the EXAFS curves shown in Figure 4.7, bottom.

Fitted EXAFS parameters

	Two-shell fits								
	T_c = 250°C			T_c = 300°C			T_c = 500°C		
	N	R(Å)	$\Delta\sigma^2$(Å^2)	N	R(Å)	$\Delta\sigma^2$(Å^2)	N	R(Å)	$\Delta\sigma^2$(Å^2)
Pd—N	2.6	2.01	0						
Pd—O$_1$	2.2	2.06	0	2.7	2.06	0	3.2	2.06	0
Pd—O$_2$				2.0	1.92	0	2.2	1.92	0

5. Electron spectroscopy
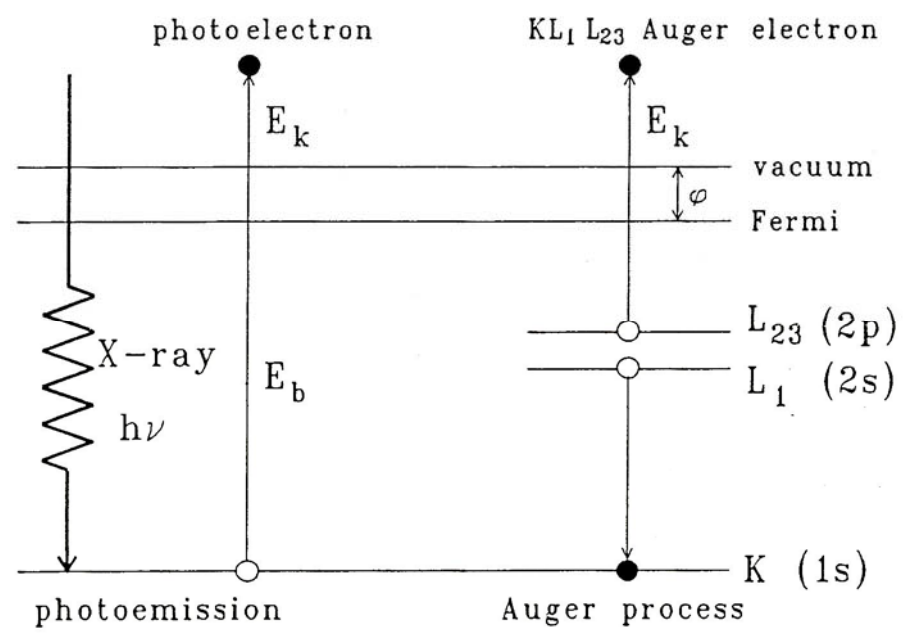
Fig. 5.1 Scheme explaining the photoemission (left) and Auger process (right).
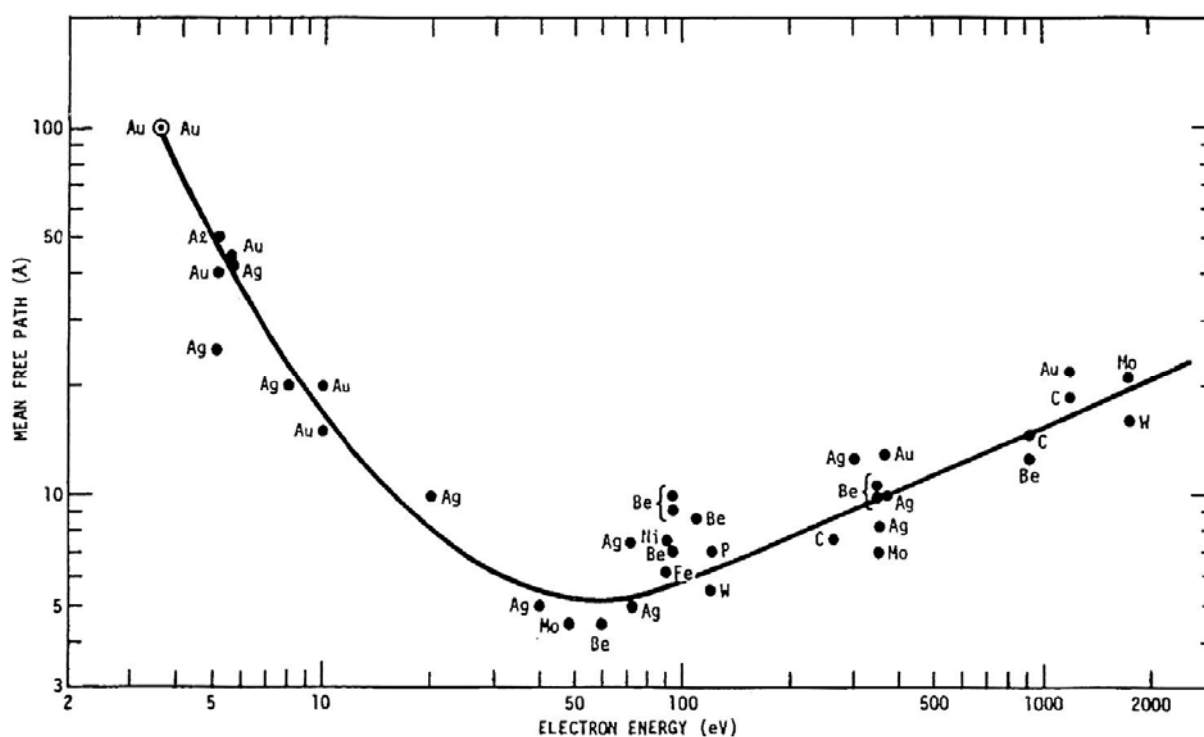
Fig. 5.2 The mean free path of electrons in different metals plotted as a function of the kinetic electron energy.
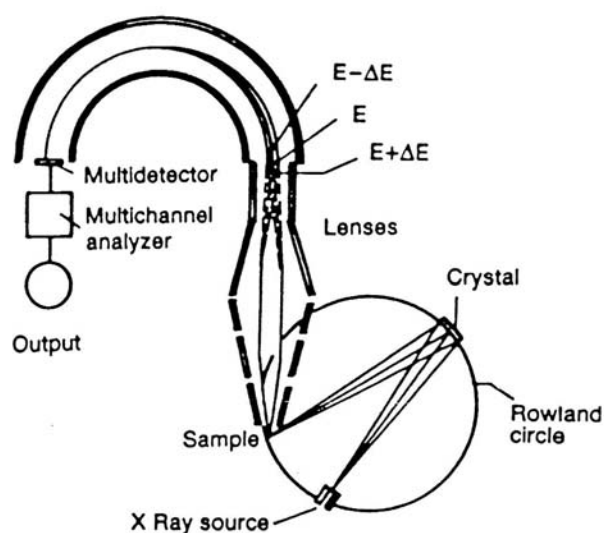
Fig. 5.3 Experimental set up of X-ray photoelectron spectroscopy (XPS).

Tab. 5.1 Chemical shifts of photoelectrons emitted by metal atoms in different oxidation states.

Element	Electronic level	Compounds	Chemical shifts (eV)
Al	$2p$	$Al^0-Al_2O_3$	2.7
Si	$2p$	Si^0-SiO_2	4.0
Co	$2p_{3/2}$	Co^0-CoO	2.1
		$Co^0-Co_3O_4$	1.8
Ti	$2p_{3/2}$	Ti^0-TiO	0.9
		$Ti^0-Ti_2O_3$	3.7
		Ti^0-TiO_2	5.1
W	$4f_{7/2}$	W^0-WO_2	1.2
		W^0-CrWO_4	2.6
		W^0-WO_3	4.2
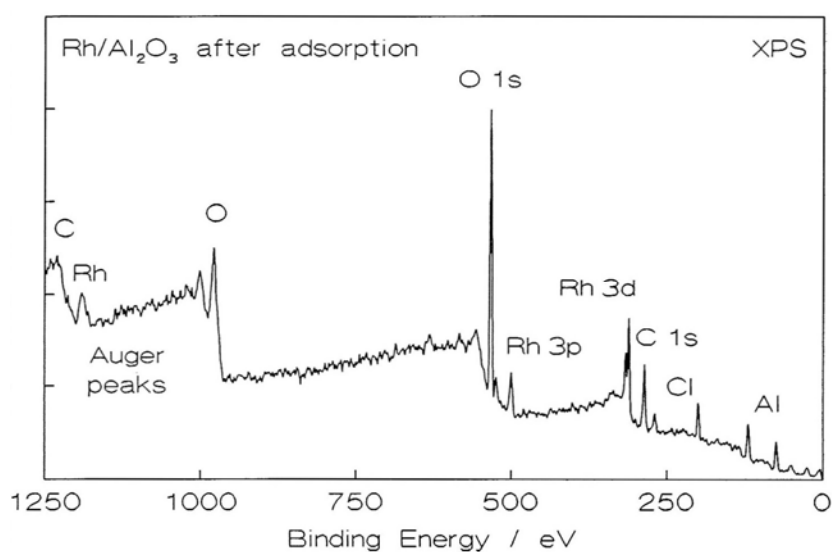
Fig. 5.4 XPS spectrum of a Rh/Al$_2$O$_3$ catalyst prepared by impregnating a thin film of Al$_2$O$_3$ with a solution of RhCl$_3$.
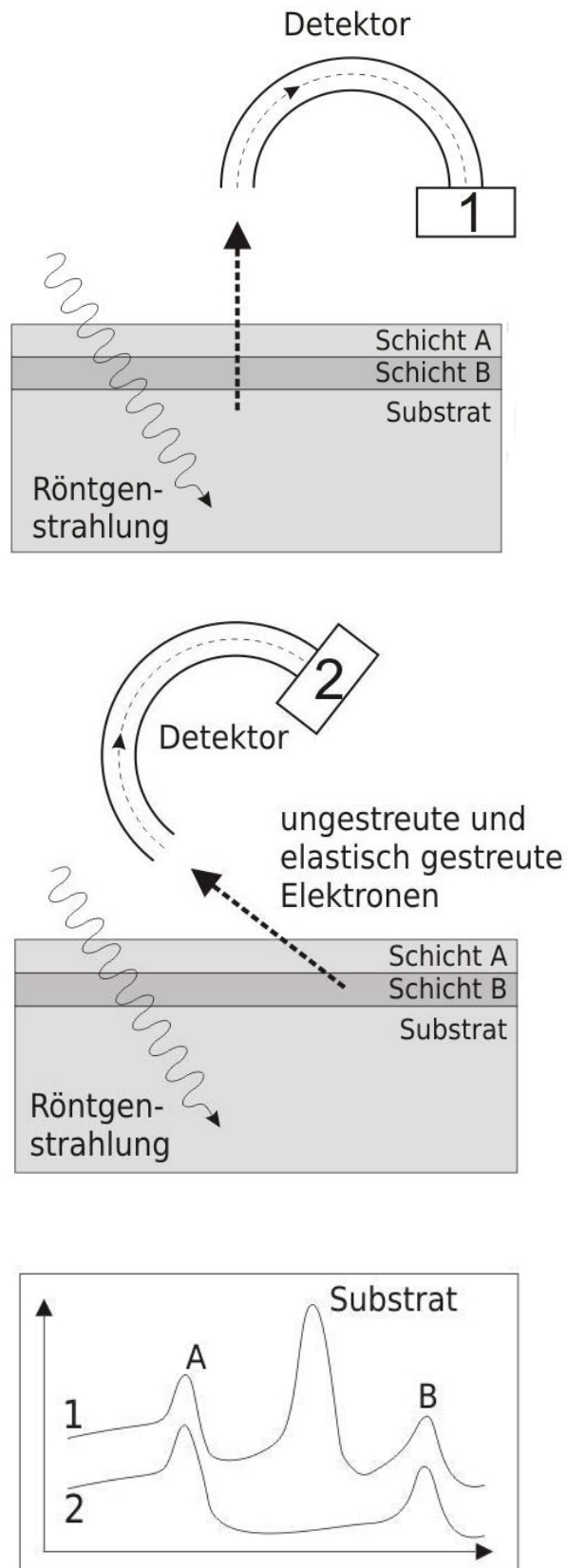
Fig. 5.5 Scheme explaining the principle of angle-resolved XPS.
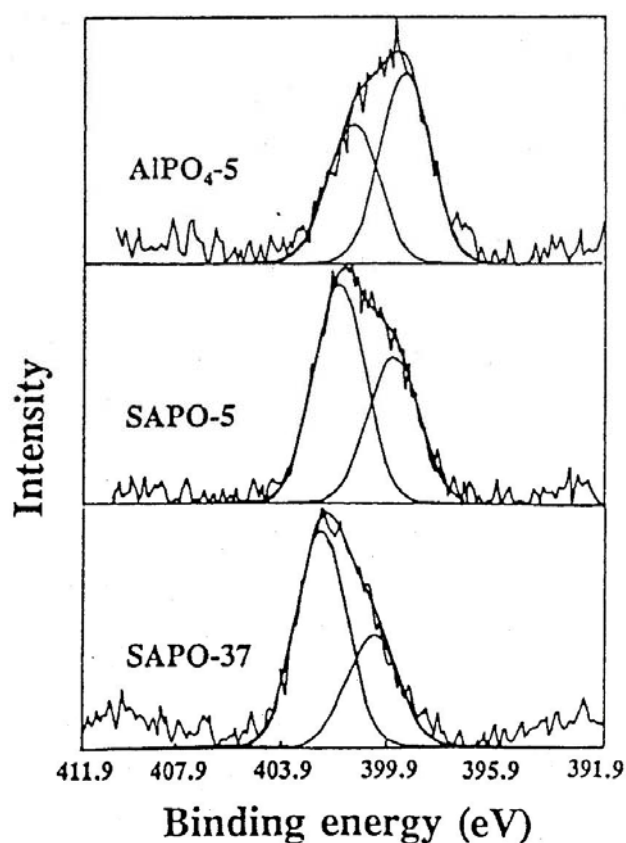
Fig. 5.6 N_{1s} XPS spectra of pyridine loaded on the microporous aluminophosphate $AlPO_4$-5 and the silicoaluminophosphates SAPO-5 and SAPO-37.

Tab. 5.2 Binding energies intensities of N_{1s} photoelectrons of pyridine loaded on various aluminophosphates and silicoaluminophosphates.

Sample	N_{1s} binding energy, eV		Relative intensity	
	(I)	(II)	(I)	(II)
$AlPO_4$-5	401.6	399.6	42.1	57.9
SAPO-5	402.1	400.0	60.1	39.9
SAPO-11	401.8	400.8	56.6	43.3
SAPO-34	401.5	398.8	67.3	33.0
SAPO-37	402.7	400.7	65.7	34.3

Tab. 5.3 Sample assignment of zeolites NH₄-Beta treated with an NH₄F solution of 0.1 mol/l.

sample	NH$_4$F soln./ml[a]	F (wt.%)[b]
A	0.0	0.00
B	3.5	0.32
C	5.0	0.64
D	10.0	1.00
E	15.0	1.29
F	20.0	1.60
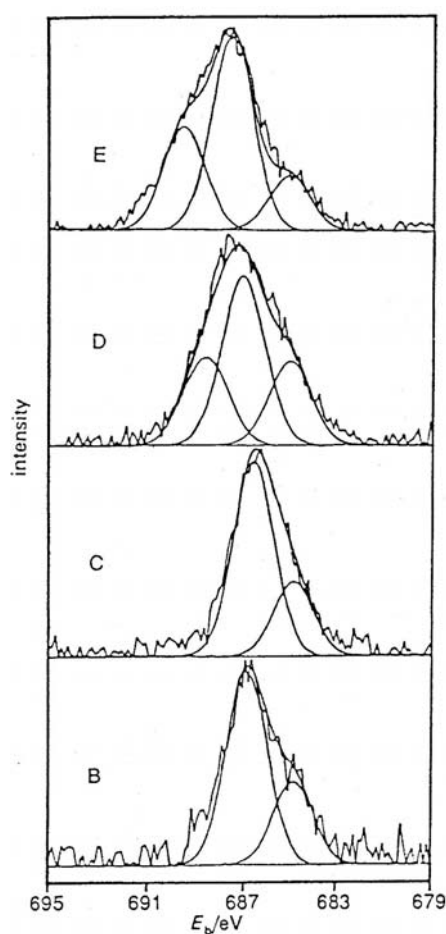
Fig. 5.7 F$_{1s}$ XPS spectra of fluorinated zeolites Beta treated according to Table 5.3.

Tab. 5.4 Fit results of the F$_{1s}$ XPS spectra of zeolites Beta in Figure 5.7.

sample	E_b/eV		
	I	II	III
B		686.7	684.7
C		686.6	684.6
D	688.4	686.8	684.9
E	689.1	687.3	685.0

main Cu 2p₃/₂ peak — rendered as: main Cu $2p_{3/2}$ peak

shake up satellite

Sample/ Treatment [a]	BE (eV) FWHM (eV)	I_S/I_P [b] % Cu reduced
calcined	935.3	0.57
air, 773 K	4.5	0
N₂,	934.9	0.44
623 K, 350 mbar	4.8	20
Heating a fresh, calcined sample in:		
vacuum,	933.6	0.16
713 K	3.9	80
NO,	934.3	0.31
298 K, 50 mbar	4.5	50
O₂,	934.8	0.52
633 K, 350 mbar	4.8	0
NO/propene [d]	934.2	0.3
633 K	4.6	50
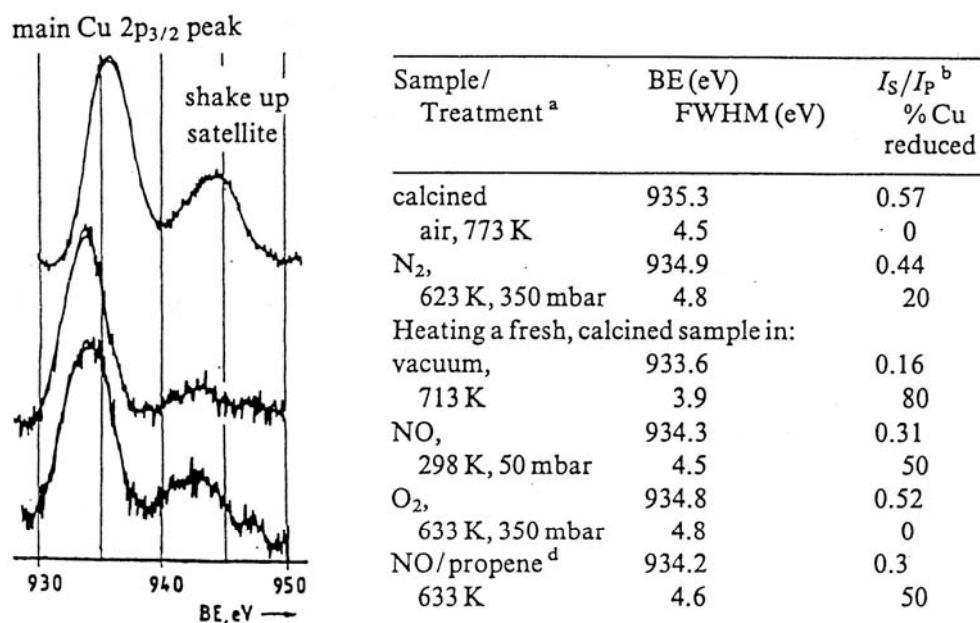
[a] Length of each treatment, 30 min; samples were cooled to ambient temperature in the treatment atmosphere; treatments were successive if not stated otherwise.

[b] The ratio of the shake up satellite intensity to that of the main Cu $2p_{3/2}$ peak. A contribution of $I_S/I_P \approx 0.05$ is due to the X-ray satellite of the Cu $2p_{1/2}$ component.

Fig. 5.8 Cu$_{2p3/2}$ XPS spectra and summary of the observed bindings energies of photoelectrons of extra-framework copper species in zeolite ZSM-5.
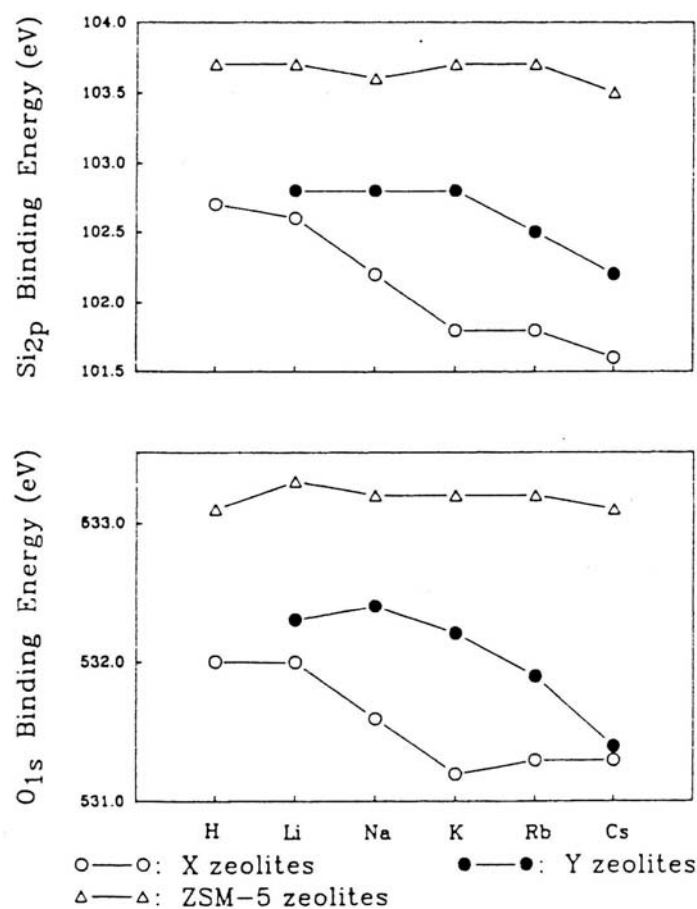
Fig. 5.9 Plot of the Si$_{2p}$ and O$_{1s}$ binding energies of photoelectrons emitted by zeolites X, Y, and ZSM-5 exchanged with different extra-framework cations.
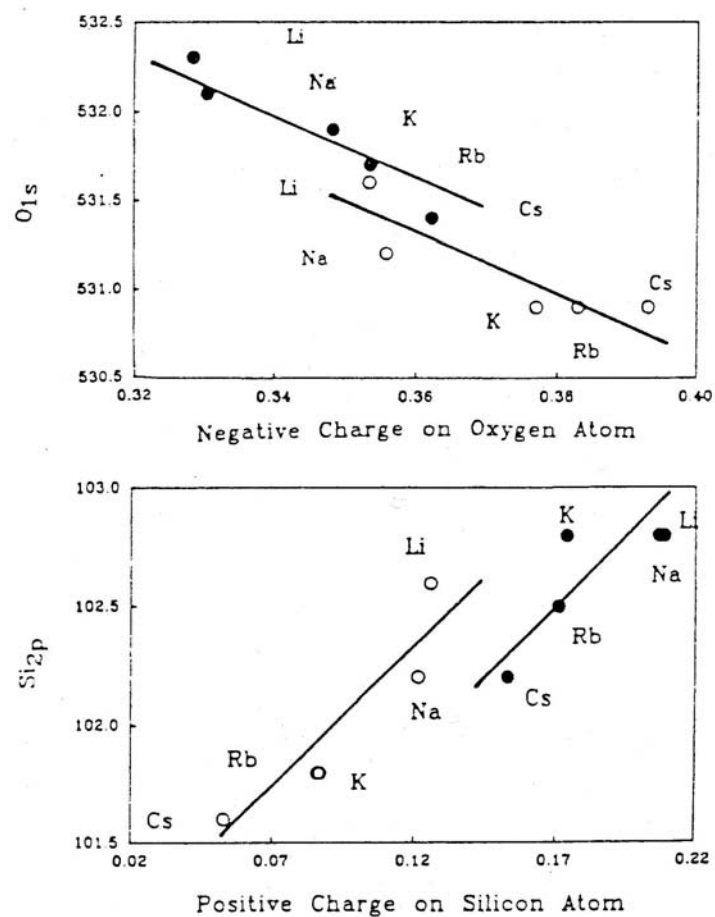
Fig. 5.10 O_{1s} and Si_{2p} binding energies of photoelectrons plotted as a function of the calculated partial charges at the framework oxygen and silicon atoms.
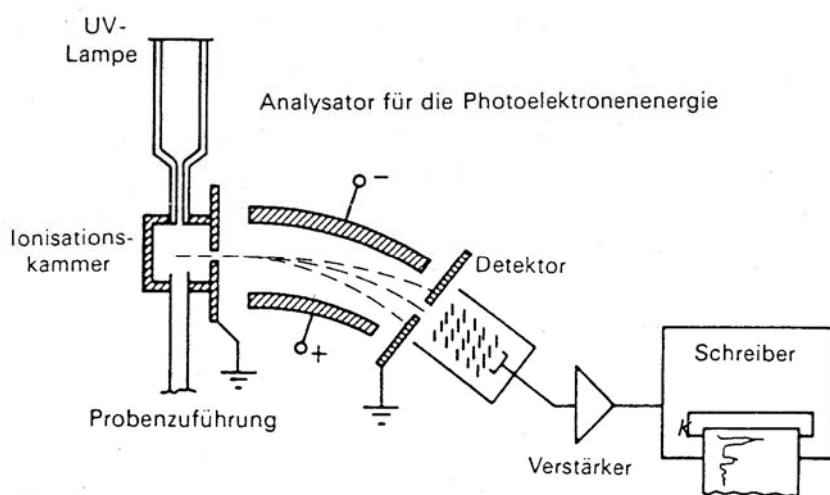
Fig. 5.11 Experimental set up of ultraviolet photoelectron spectroscopy (UPS).
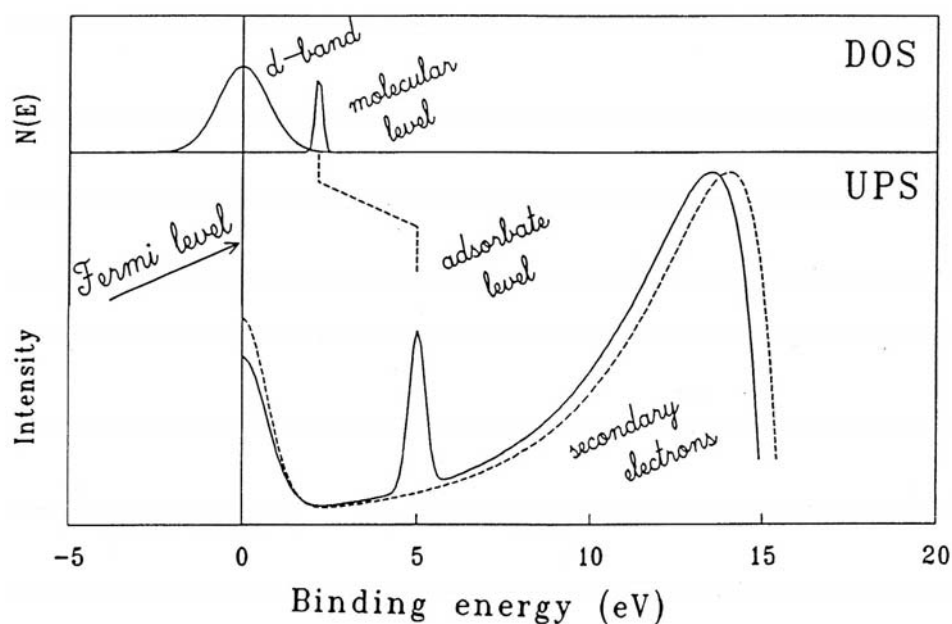
Fig. 5.12 Scheme of UPS spectra (bottom) of d-metals and adsorbed species and the density of states (top).
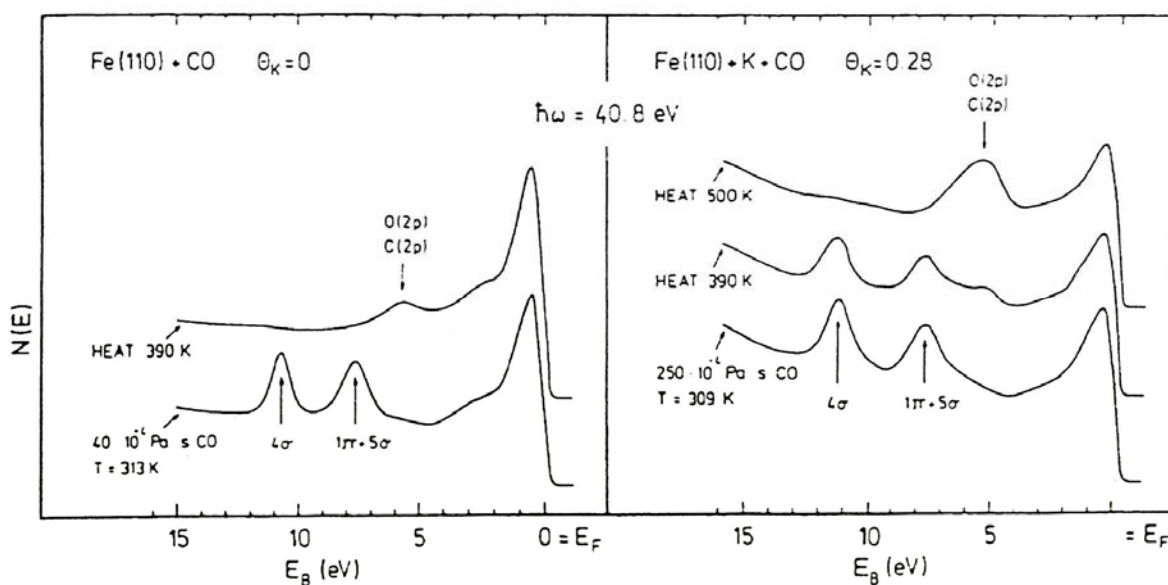
Fig. 5.13 UPS spectra of carbon monoxide chemisorbed on iron showing the shift of the 5s orbital (bottom, left), the stabilizing effect of potassium species (bottom, right)), and the dissociation of CO at higher temperatures (top).
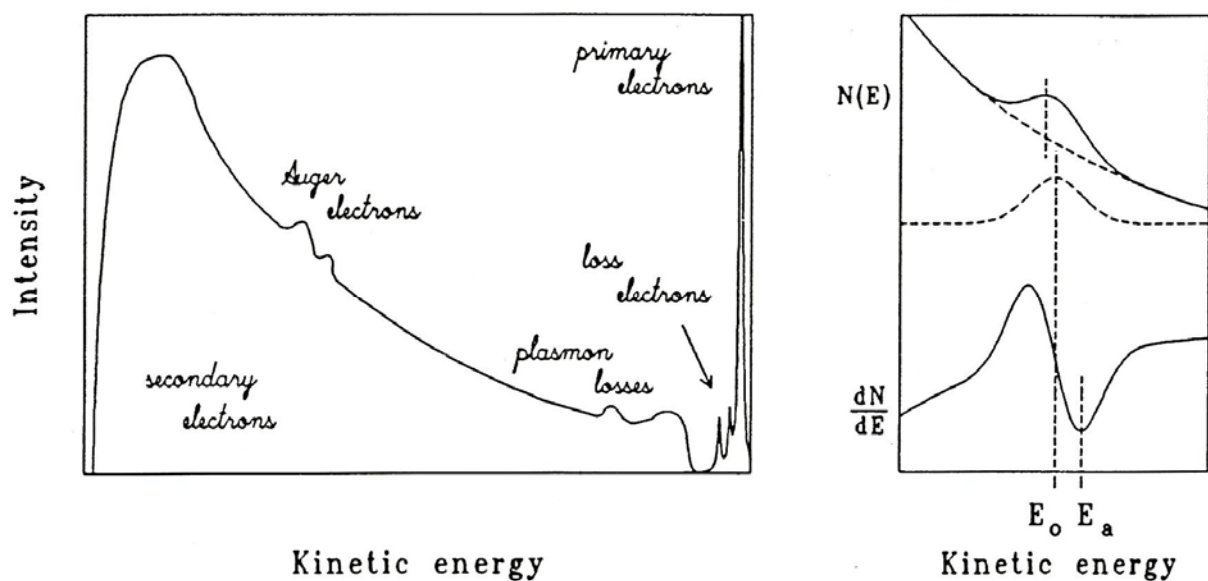
Fig. 5.14 Scheme of an AES spectrum (left) and the derivative spectrum for better visibility (right).
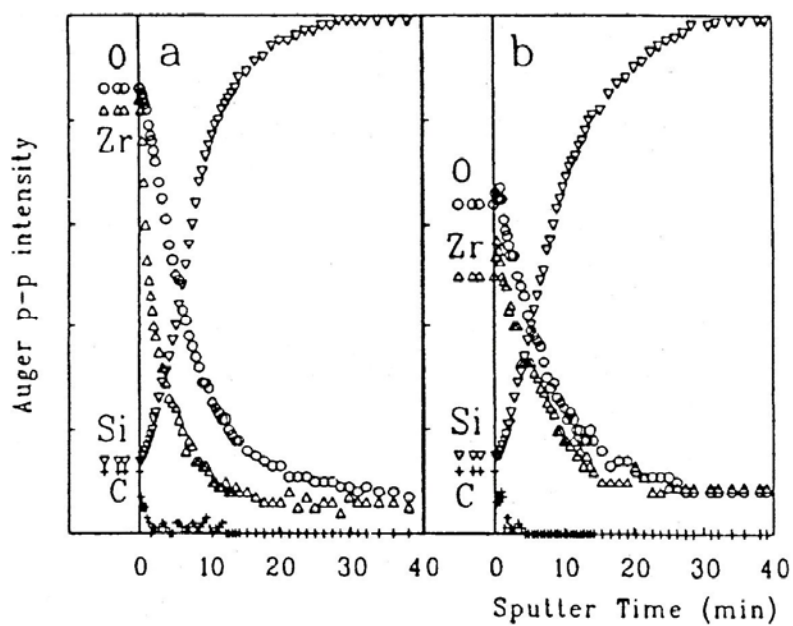
Fig. 5.15 AES sputter depth profile of a layered $ZrO_2/SiO_2/Si$ catalyst. The left profile (a) indicates a zirconium-rich surface layer over the SiO_2, while the right profile (b) is characteristic for the composition of larger particles.
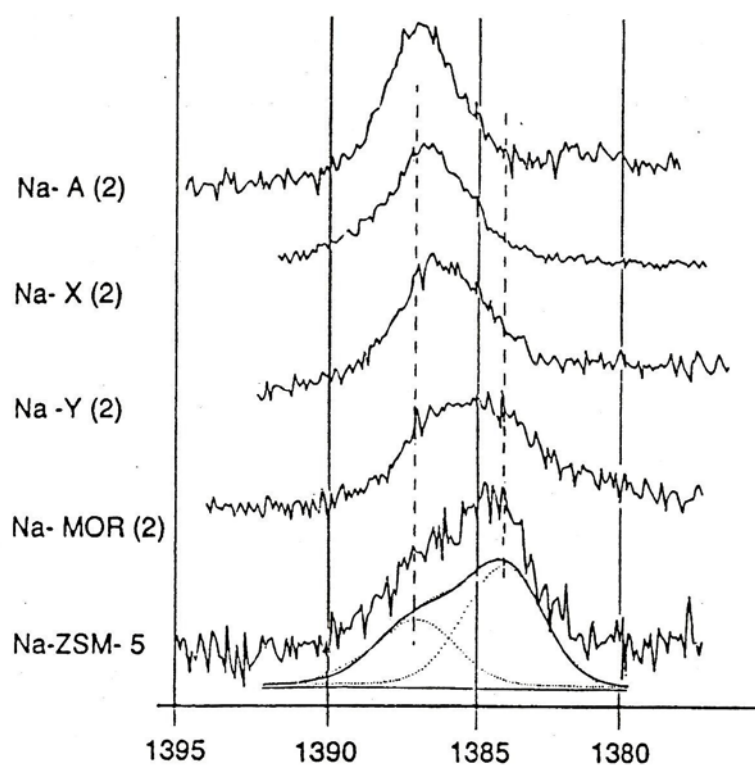
Fig. 5.16 Al KLL Auger lines of zeolites with different aluminum contents responsible for the shifting of the centre of gravity.
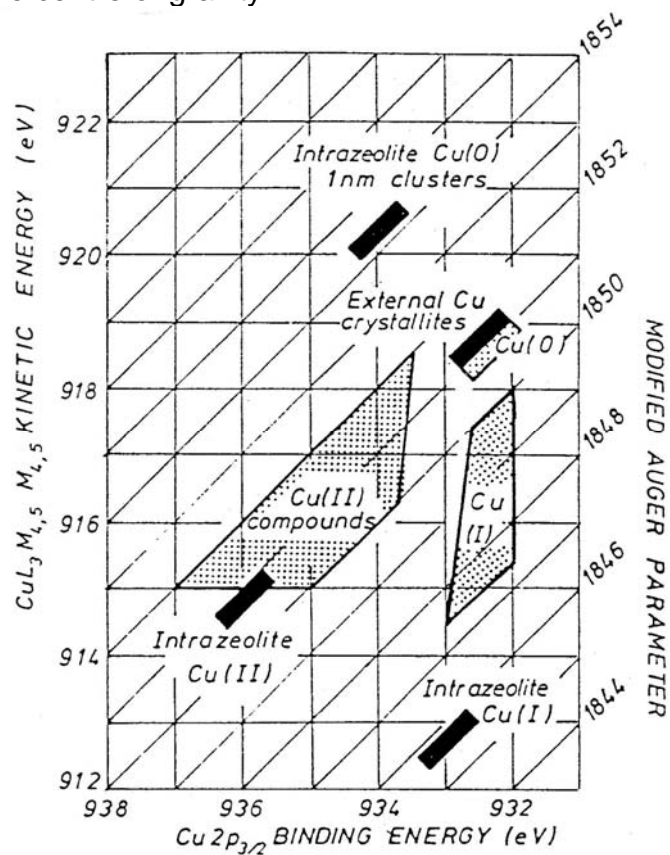
Fig. 5.17 Wagner plot for copper in Cu-exchanged zeolites A, X, and Y in the ionic and reduced states. Hatched areas represent known data for copper compounds.

6. Ion spectroscopy
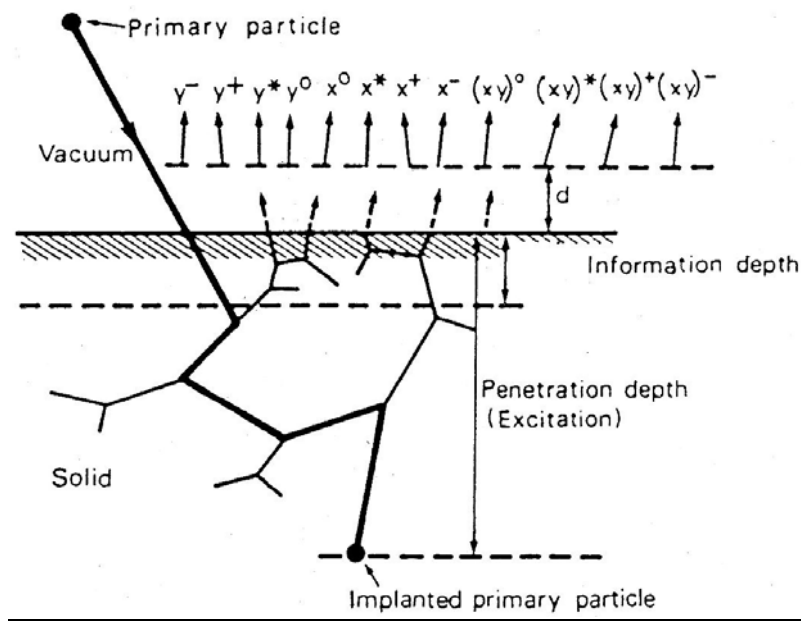
Fig. 6.1 Scheme of the effects occurring in a sample studied by ion spectrometry.
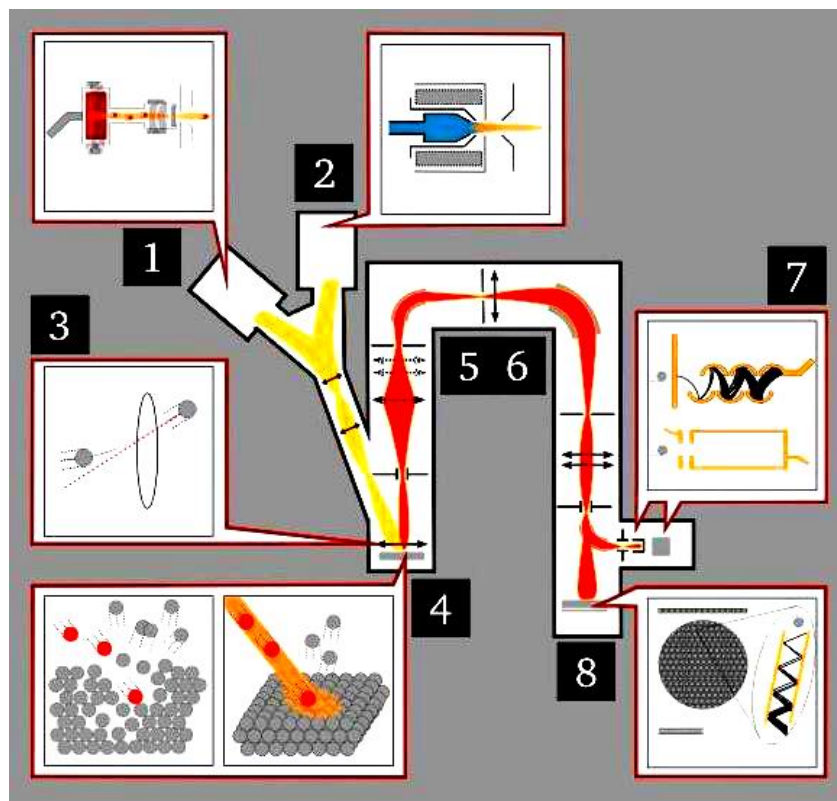
Fig. 6.2 Set up of secondary ion mass spectrometry with ion guns (1 and 2) focusing on the target sample (3), which ionizes and sputters ions from the surface (4). The secondary ions are collected by ion lenses (5), filtered according to their mass (6), and projected on an electron multiplier (7, top), Faraday cup (7, bottom) or CCD screen (8).

Tab. 6.1 Advantages and disadvantages of secondary ion mass spectrometry.

Advantages	Disadvantages
The uppermost layers are analyzed	Large sensitivity differences: function of
Analysis of all the atomic elements,	the surface structure and of presence of
including hydrogen	contaminants (partly hamper quantitative
Detection of molecules	analysis)
(see molecular SIMS)	Difficulties in interpretation of molecular
Lateral resolution	fragmentation patterns
Isotope separation	Surface reactions induced by ions
High sensitivity — Quantitative analysis	Modification of signal intensity by
possible	presence of pores in the bombarded solid
Weak surface destruction	
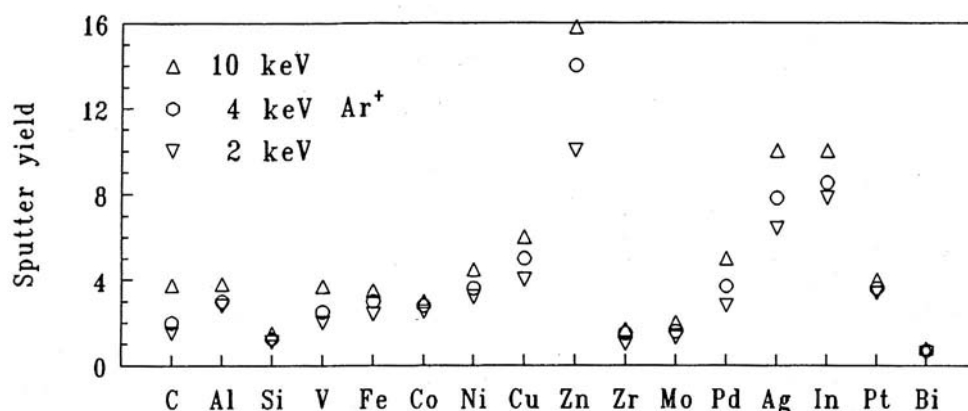
Fig. 6.3 Sputter yields Y of selected elements under bombardments with Ar^+ ions of an energy of 2, 4, and 10 keV.
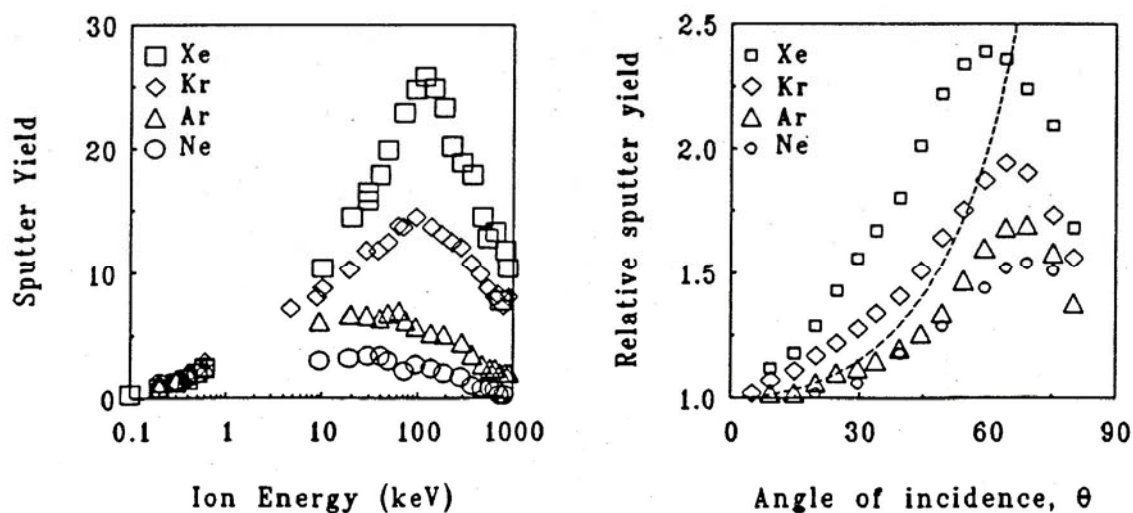
Fig. 6.4 Sputter yields Y of copper under bombardment with Ne^+, Ar^+, Kr^+, and Xe^+ ions as a function of the energy (left) and relative sputter yields of copper as a function of the incident beam angle (to the surface normal) for an primary ion energy of 1.05 keV. Dashed line corresponds to $1/\cos \Theta$.

Tab. 6.2 Ionization potential *I*, work function φ, sputter yield *Y*, and secondary ion yield R^+Y (R^+ for positive ions) of selected elements and their oxides.

Element	I	φ	Y	R^+Y	R^+Y_{oxide}
Mg	7.64	3.66	4.5	0.01	0.9
Al	5.98	4.28	2.8	0.007	0.7
Si	8.15	4.85	1.1	0.0084	0.58
Ti	6.28	4.33	1.2	0.0013	0.4
V	6.74	4.3	2.0	0.001	0.3
Cr	6.76.	4.5	3.0	0.0012	1.2
Mn	7.43	4.1	4.0	0.0006	0.3
Fe	7.87	4.5	2.4	0.0015	0.35
Ni	7.63	5.15	3.2	0.0006	0.045
Cu	7.72	4.05	4.0	0.0003	0.007
Mo	7.13	4.6	1.3	0.00065	0.4
Ta	7.70	4.25	1.25	0.00007	0.02
W	7.98	4.55	1.25	0.00009	0.035
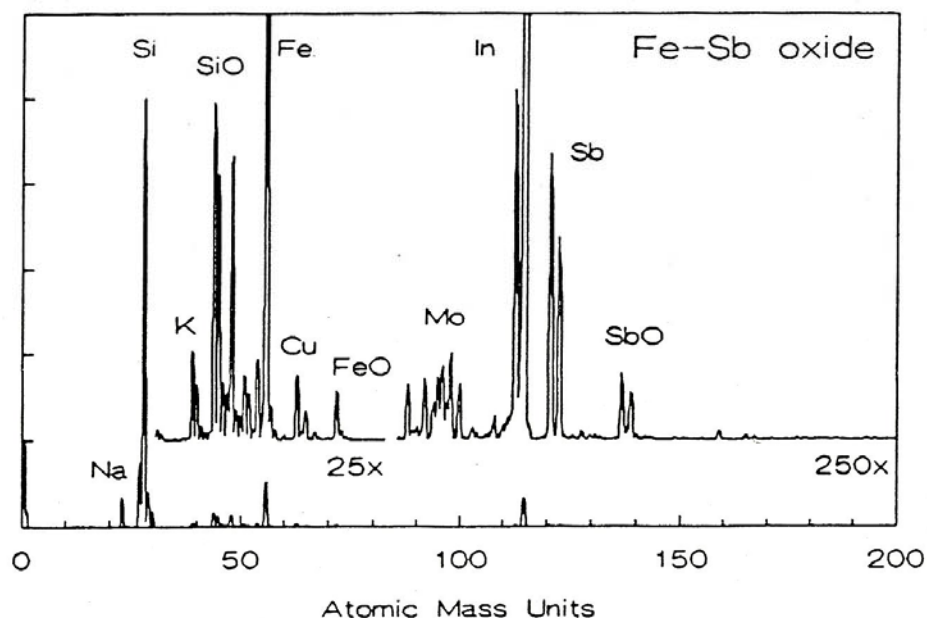
Fig. 6.5 SIMS spectrum of a promoted Fe-Sb oxide catalyst. The spectrum was recorded with a 5 keV beam of Ar^+ ions under dynamic conditions.
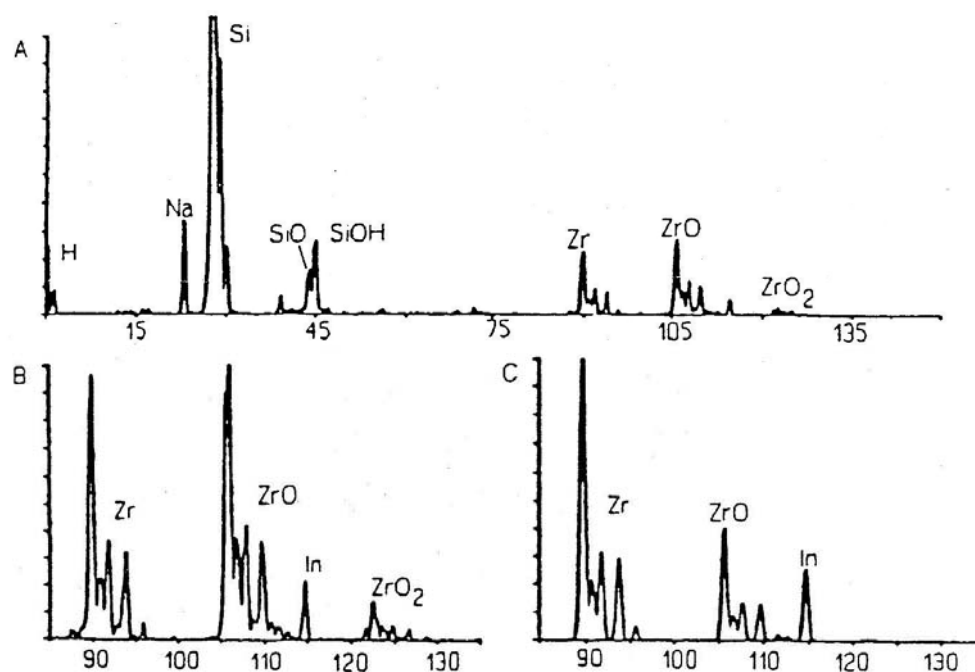
Fig. 6.6 Positive SIMS spectrum of a 9wt%ZrO$_2$/SiO$_2$ catalyst prepared from zirconium ethoxide after drying (A, B) and calcination at 673 K (C). ZrOH$^+$ occurs at 107 (^{90}ZrOH$^+$ and ^{91}ZrO$^+$) and 111 amu (^{94}ZrOH$^+$).
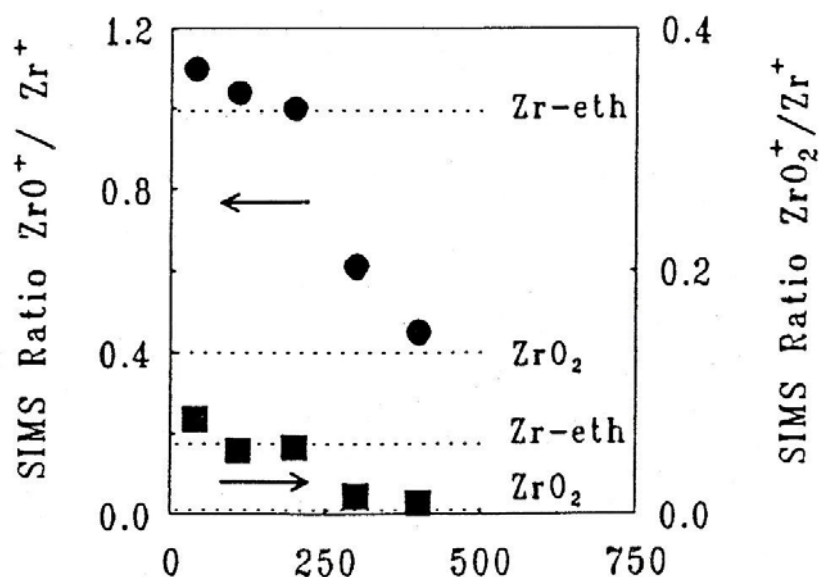
Fig. 6.7 SIMS intensity ratios of ZrO$^+$/Zr$^+$ (●) and ZrO$_2^+$/Zr$^+$ (■) plotted as a function of the calcination temperature for the materials in Figure 6.6 in comparison with model compounds (dotted lines).
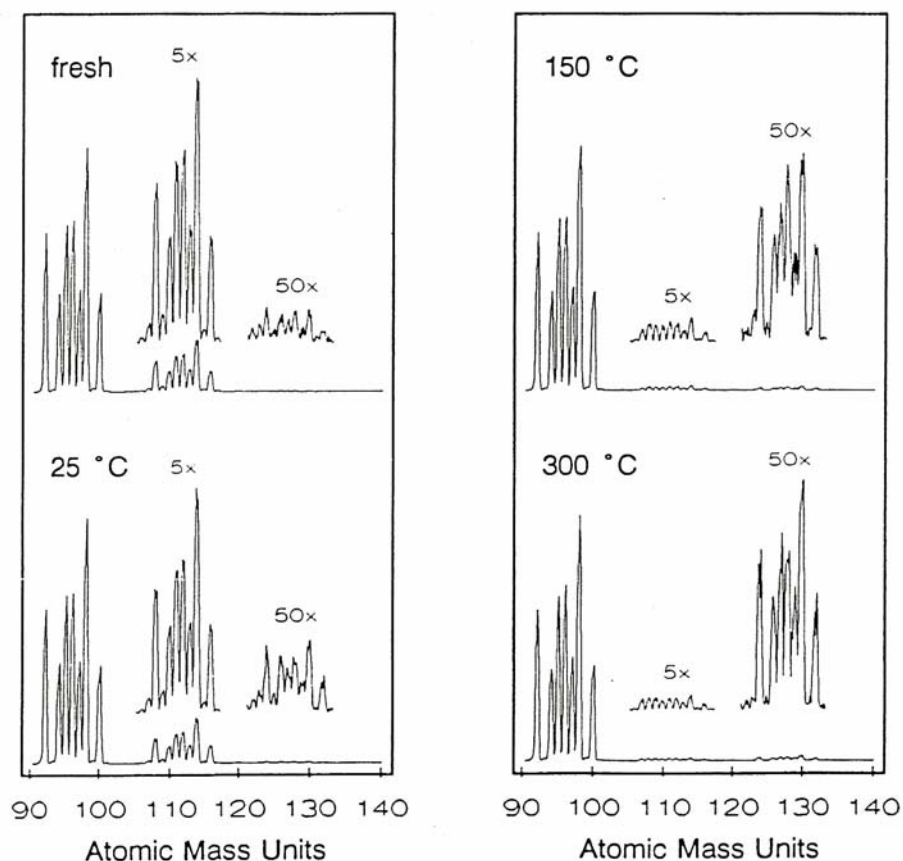
Fig. 6.8 Positive SIMS spectra of MoO$_3$/SiO$_2$/Si(100) catalysts recorded after impregnation (fresh) and after sulfurization in 10% H$_2$S in H$_2$ and additional calcination at 298, 423, and 573 K.
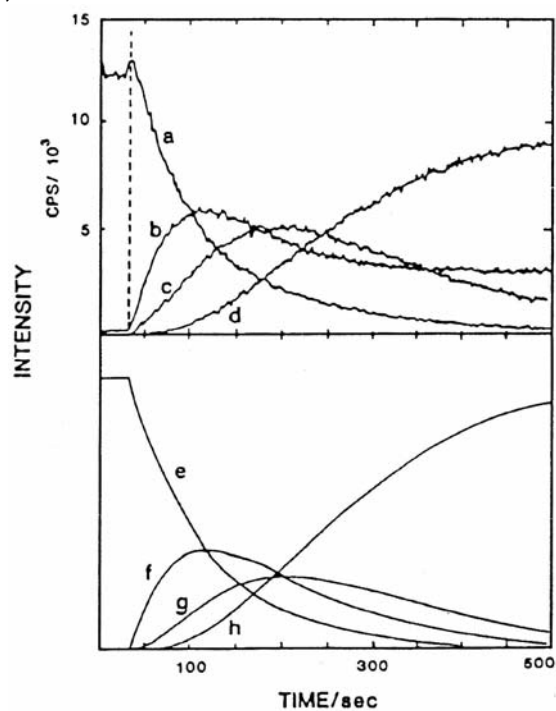
Fig. 6.9 SIMS intensities of ethylidyne ($\equiv$CCH$_3$) on platinum (111) recorded during reaction with D$_2$. Curves a, b, c, and d are the experimental intensities of the CH$_n^+$ fragments at 15, 16, 17, and 18 amu. Curves e-h are the corresponding simulations.
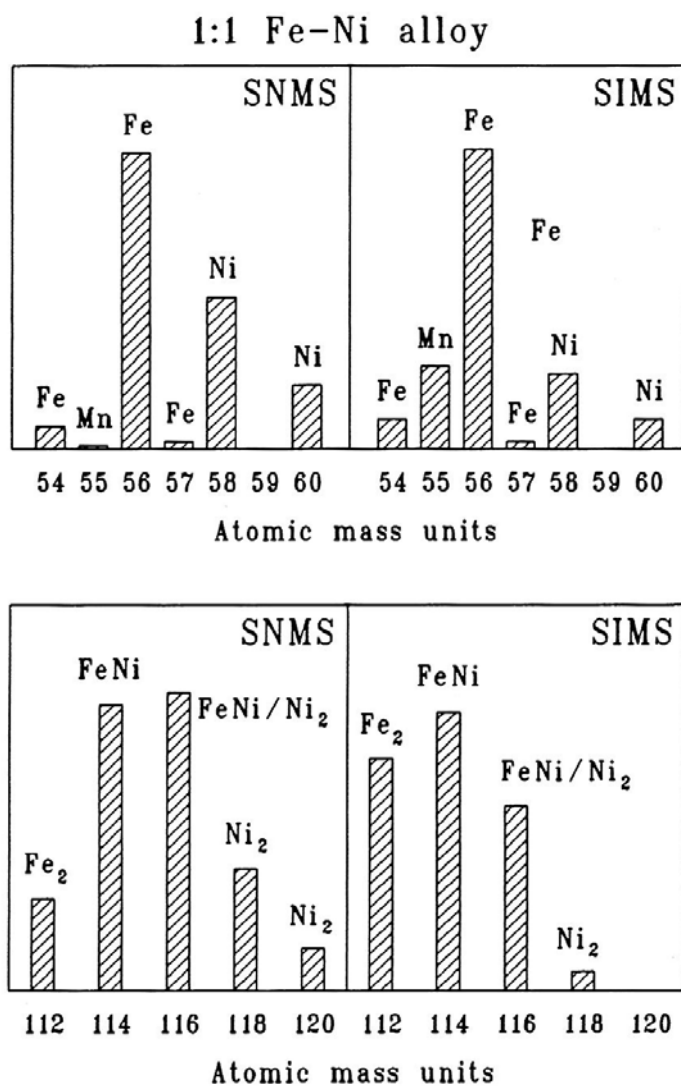
1:1 Fe-Ni alloy

Fig. 6.10 SNMS intensities of a Fe-Ni alloy (1 : 1) in the mass region of monomers (top) and dimers (bottom) in comparison with the results of SIMS studies.
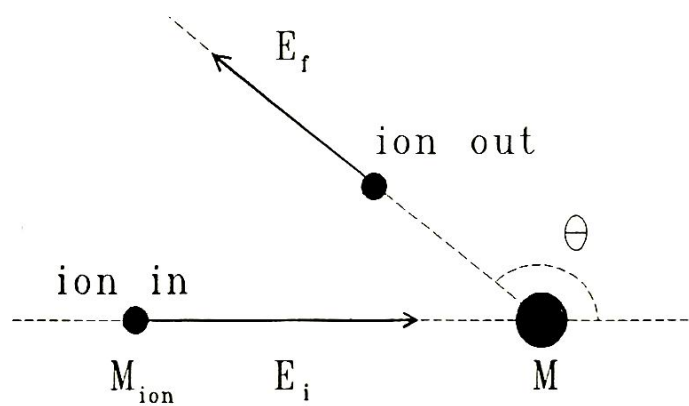
Fig. 6.11 Geometry of an ion scattering experiment with mass M_{ion} and energy E_i of the incident ions and energy E_f of the ions scattered in the angle of Θ. The mass of the target atoms is M.
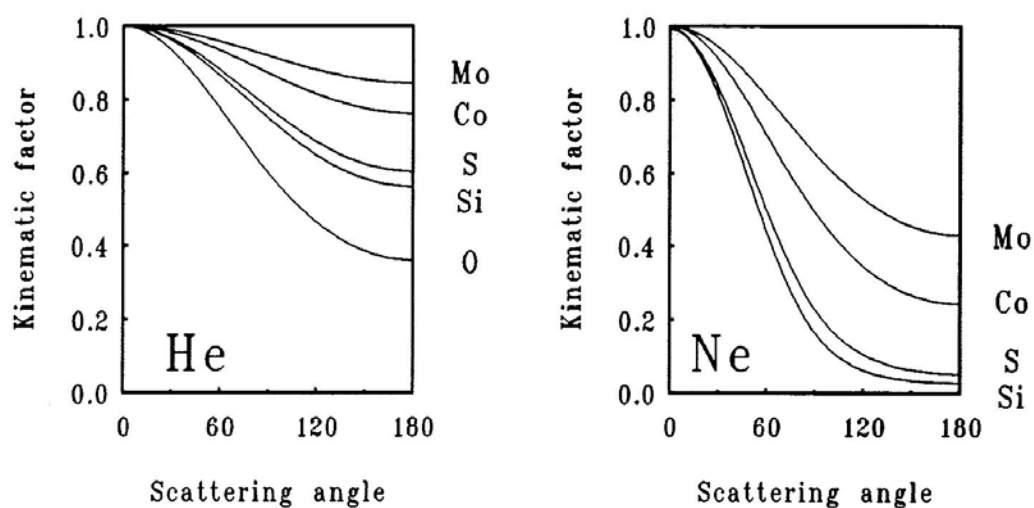
Fig. 6.12 Kinetic factor E_f/E_i for He$^+$ and Ne$^+$ ions as a function of the scattering angle Θ for various elements.
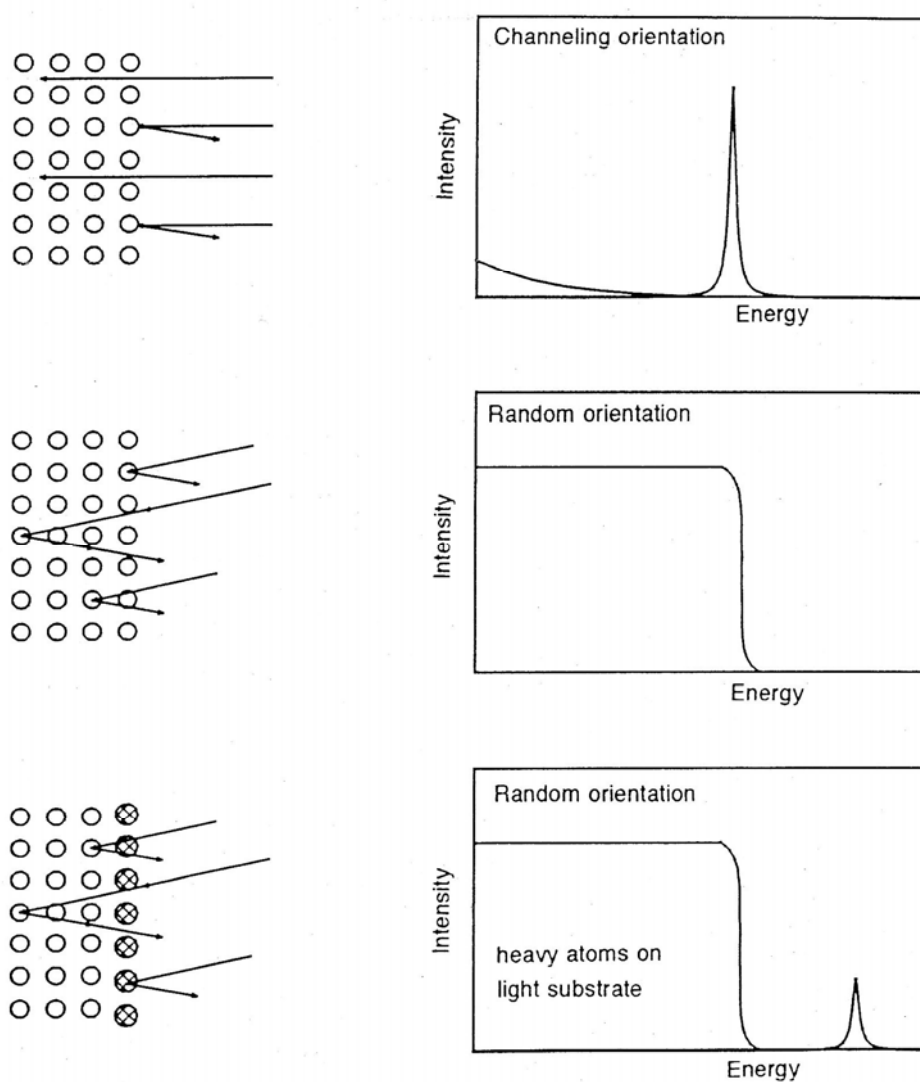
Fig. 6.13 Scheme of RBS spectra obtained for oriented single crystals (top), randomly oriented crystals without (middle), and with (bottom) surface layers consisting of heavy atoms or complexes.
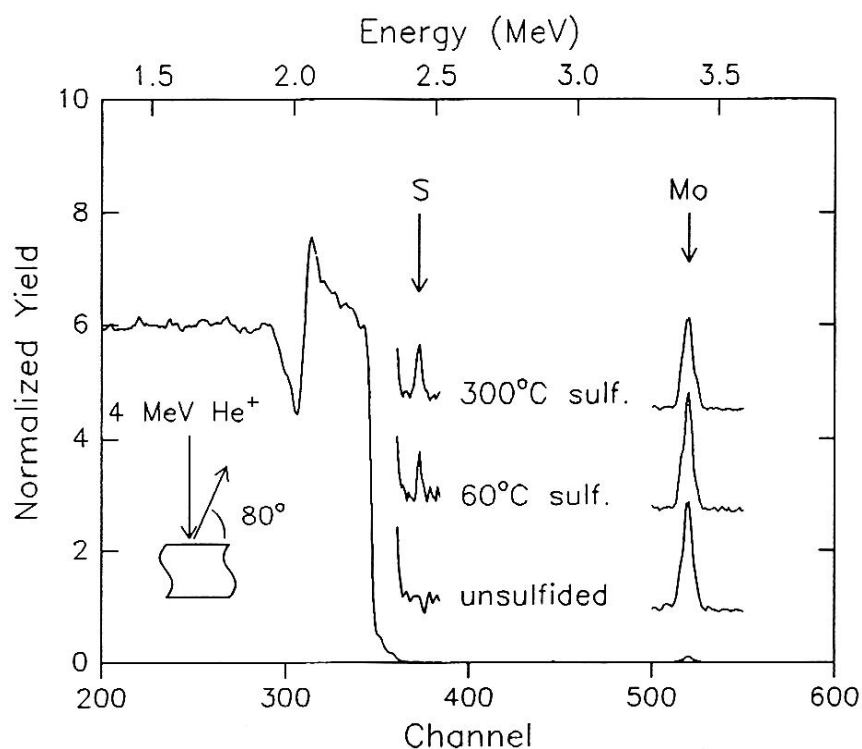
Fig. 6.14 RBS spectra of MoO_3 model catalysts supported on a $SiO_2/Si(100)$ material recorded before (bottom) and after sulfurization in a mixture of H_2S and H_2 at 333 K (middle) and 573 K (top).
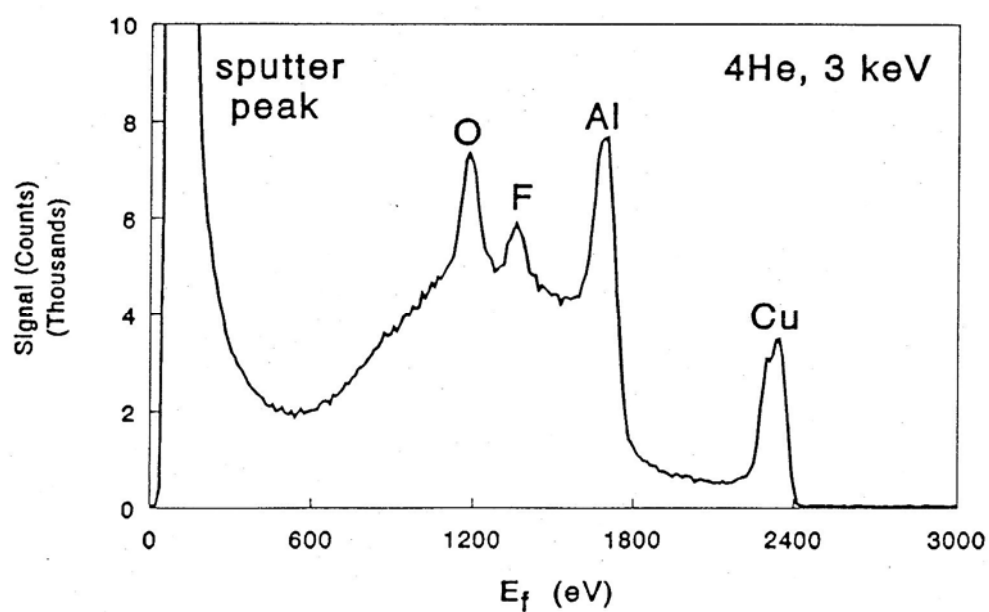
Fig. 6.15 LEIS spectrum of a Cu/Al_2O_3 catalyst. The high peak at low energies is due to sputtered fragments.

7. Vibrational spectroscopy
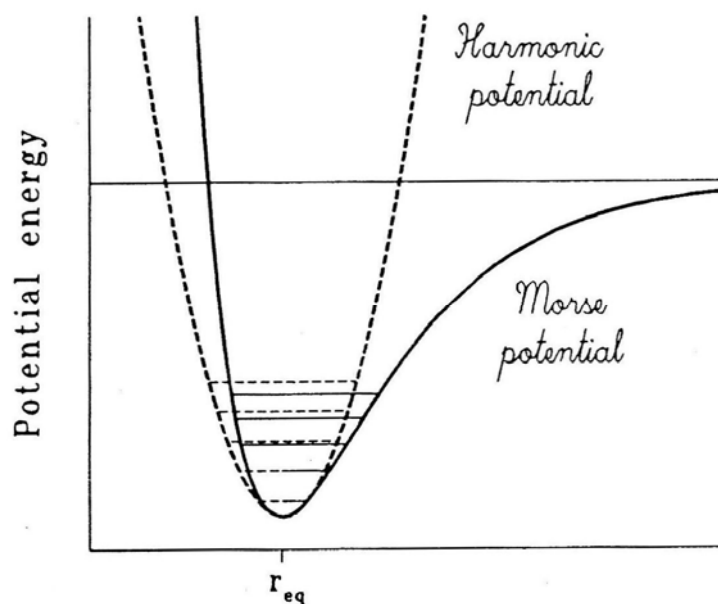
Fig. 7.1 Scheme of the harmonic potential and the Morse potential of vibrating molecules.

Fig. 7.2 Position of vibration spectroscopy in the general spectral and energetic range of spectroscopic methods.
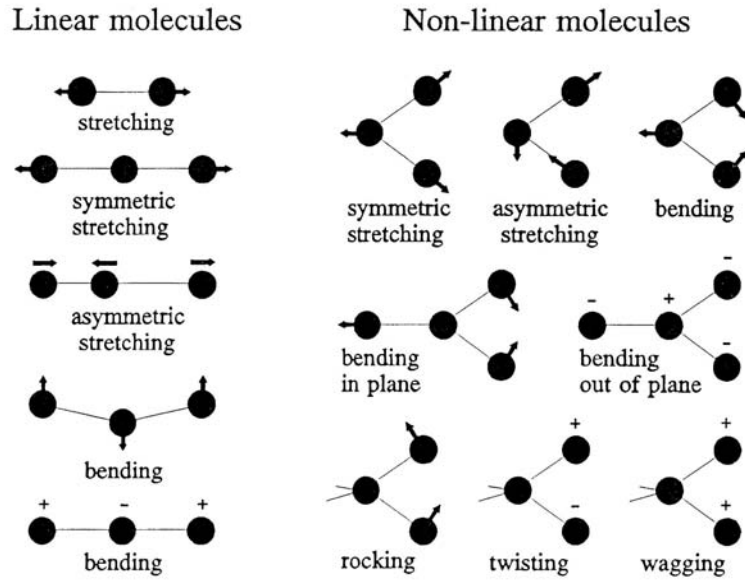
Fig. 7.3 Fundamental vibrations of molecules.

Tab. 7.1 Survey on the abbreviations of fundamental vibrations.

1. Bond deformation	
Stretching of one bond	
stretching	ν
Stretching of two bonds	
Symmetric	ν_s
Antisymmetric	ν_a
2. Angle deformations	
Bending (used only when the group is simple,	
otherwise the following notations are used)	δ
Scissor	δ
Wagging	γ
Twisting	ρ
Rocking	β

Tab. 7.2 Spectral ranges of infrared spectroscopy.

Region	Wavelength (μm)	Energy (meV) [a]	Wavenumber (cm^{-1})	Detection of
Infrared	1000 - 1	1.2 - 1240	10 - 10000	
Far	1000 - 50	1.2 - 25	10 - 200	Lattice Vibrations
Mid	50 - 2.5	25 - 496	200 - 4000	Molecular Vibration
Near	2.5 - 1	496 - 1240	4000 - 10000	Overtones
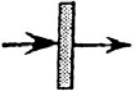
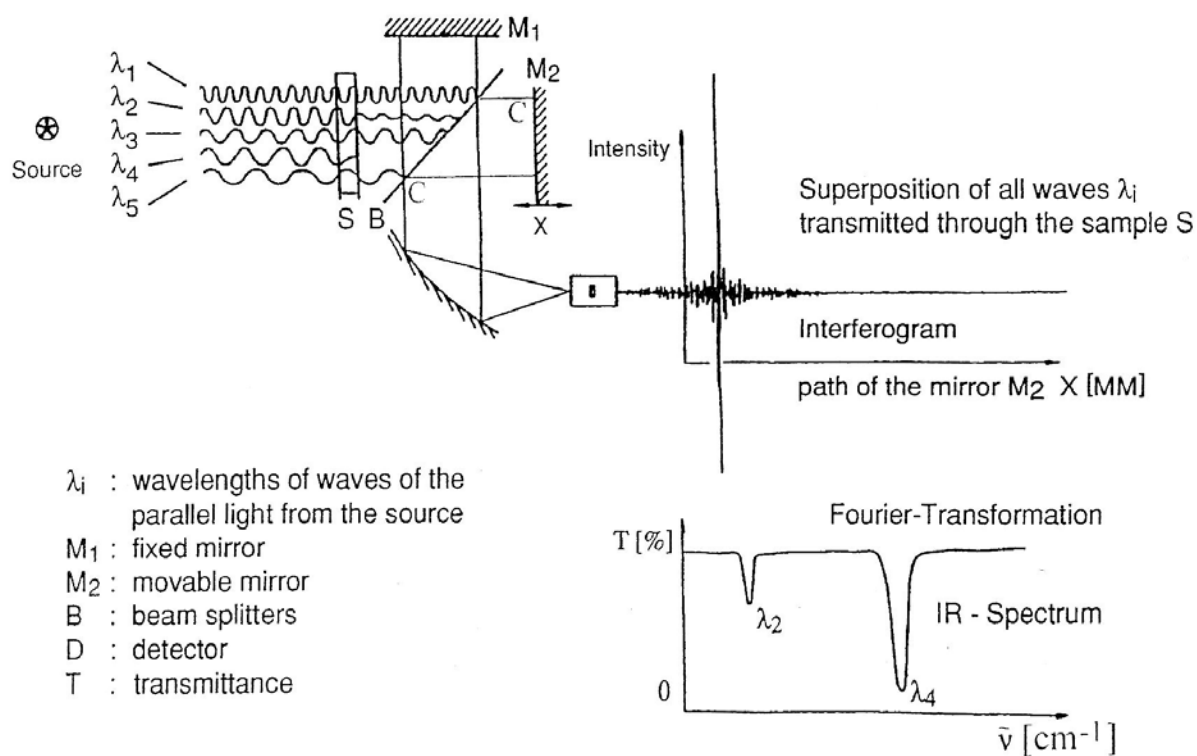a) $1\ meV = 8.0655\ cm^{-1}$

Tab. 7.3 Vibrations of typical compounds in heterogeneous catalysis.

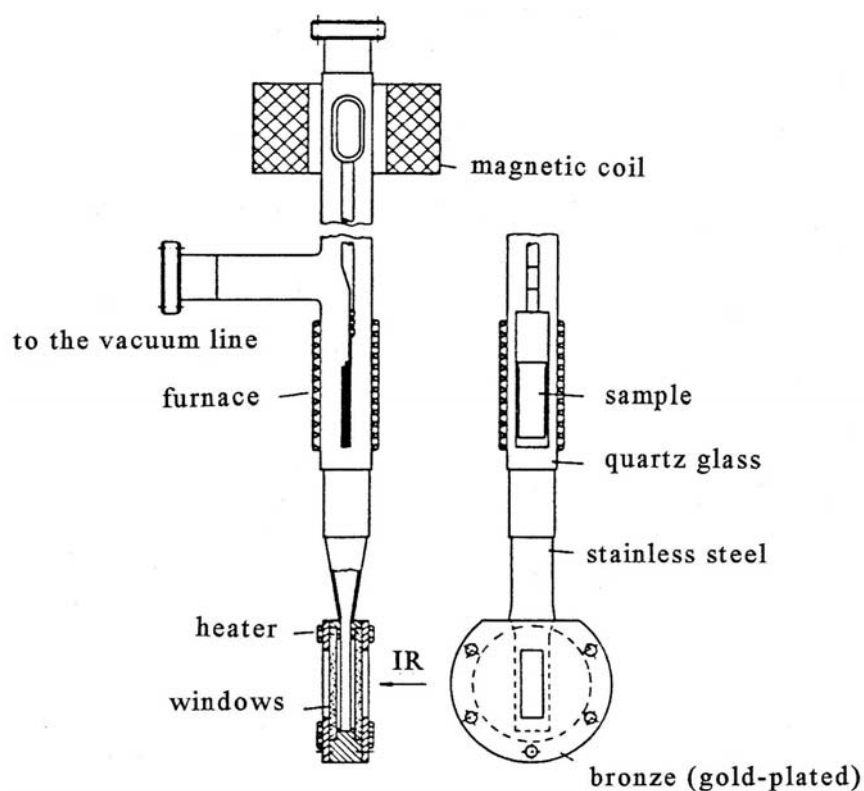| Stretching vibration functional group	Frequency range (cm^{-1})	Examples (cm^{-1})
O—H organic	3700–3500	Benzyl alcohol: 3618
O—H inorganic	3750–3300	Si—OH: 3740
N—H	3500–3200	CH_3NH_2: 3361 and 3427
C—H	3300–2800	CH_4: 3020
C=C olefinic, aromatic	1690–1500	C_2H_4: 1623
C—O	1430–900	$CH_3—O—CH_3$: 1103 and 932
Si—O organic	1100–1000	Siloxanes
Si—O inorganic	1100–700	Olivine: 1100–1000 and 830
		Benitoïte: 1035, 930, and 761
		Y zeolite: 1020 and 720

**Tab. 7.4** Experimental methods of infrared spectroscopy.

Method	Transmission	Diffuse reflectance	Reflection – absorption	Emission
Samples	thin wafers single crystals	powders	metal foils or	metal powders
Range [cm⁻¹]	4000–1000	8000–1000 400–<10	4000–<10	2500–ca. 100 at 475 K (dependent on T)
Advantages	simple well-proven	surface sensitivity gas-solid contact less scattering losses	possibility of using metals	sample versatility spatial resolution
Dis-advantages	limited to semi-transparent materials, pressing of wafers required	lower re-producibility dilution	smooth samples required long signal pathway	low signal to noise ratio background radiation

Fig. 7.4 Scheme of a Fourier transform infrared (FTIR) spectrometer.

λ_i : wavelengths of waves of the parallel light from the source
M_1 : fixed mirror
M_2 : movable mirror
B : beam splitters
D : detector
T : transmittance

Fig. 7.5 Set up of a transmission cell for Fourier transform infrared (FTIR) spectroscopy of calcined samples in vacuum and loading of probe molecules.
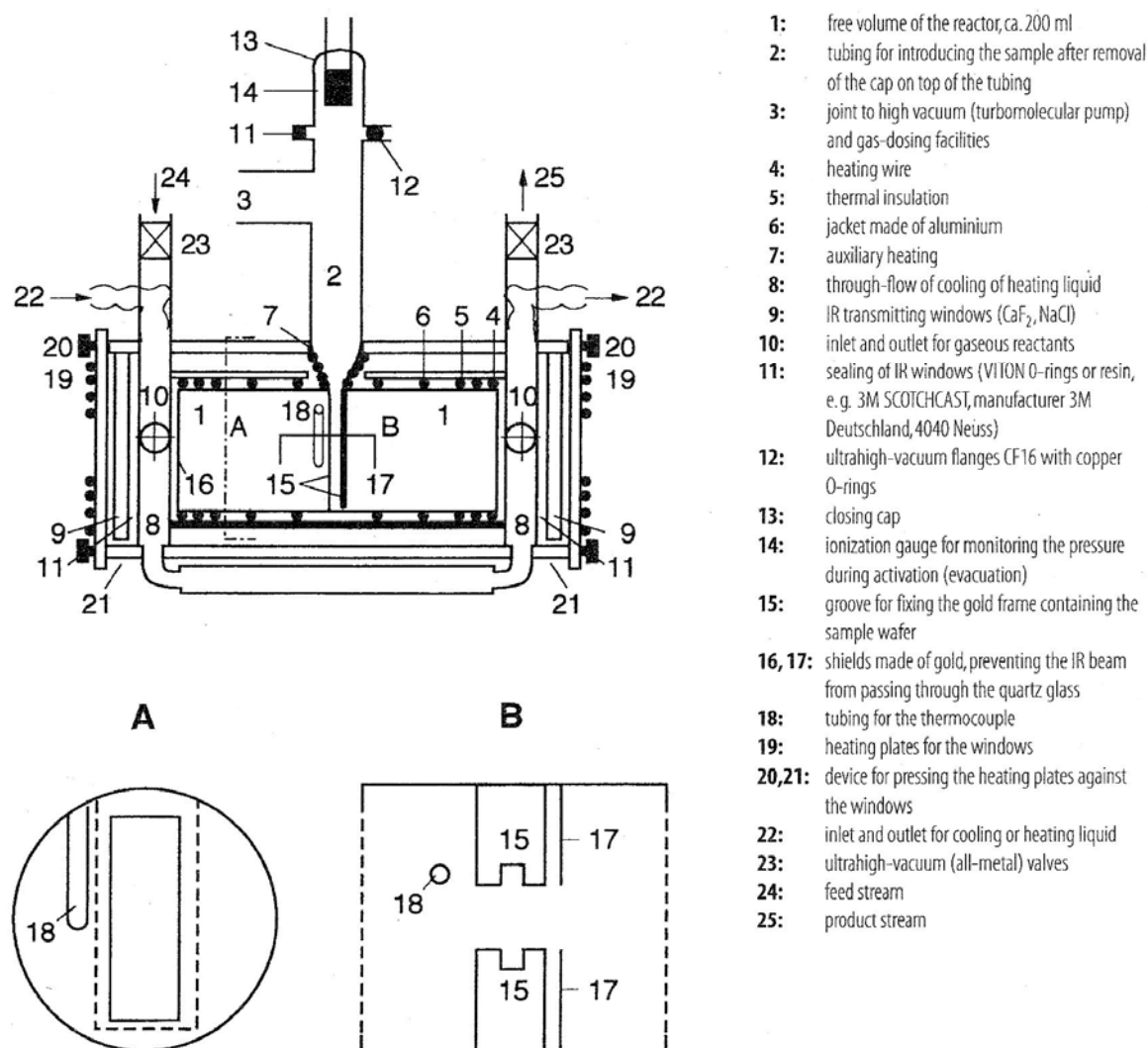
Fig. 7.6 Set up of a transmission cell for in situ Fourier transform infrared (FTIR) spectroscopic studies of calcined catalysts under reaction conditions.

1: free volume of the reactor, ca. 200 ml
2: tubing for introducing the sample after removal of the cap on top of the tubing
3: joint to high vacuum (turbomolecular pump) and gas-dosing facilities
4: heating wire
5: thermal insulation
6: jacket made of aluminium
7: auxiliary heating
8: through-flow of cooling of heating liquid
9: IR transmitting windows (CaF_2, NaCl)
10: inlet and outlet for gaseous reactants
11: sealing of IR windows (VITON O-rings or resin, e.g. 3M SCOTCHCAST, manufacturer 3M Deutschland, 4040 Neuss)
12: ultrahigh-vacuum flanges CF16 with copper O-rings
13: closing cap
14: ionization gauge for monitoring the pressure during activation (evacuation)
15: groove for fixing the gold frame containing the sample wafer
16, 17: shields made of gold, preventing the IR beam from passing through the quartz glass
18: tubing for the thermocouple
19: heating plates for the windows
20, 21: device for pressing the heating plates against the windows
22: inlet and outlet for cooling or heating liquid
23: ultrahigh-vacuum (all-metal) valves
24: feed stream
25: product stream

Tab. 7.5 Window materials and their spectral ranges.

Window	Spectral range (cm^{-1})	Sensitivity toward H_2O	Price
CaF_2	10,000–1000	Slightly soluble	
NaCl	10,000–500	Soluble	
KBr	10,000–300	Very soluble	
CsI	10,000–170	Very soluble	Very expensive
KRS$_5$ (TlBr, TlI)	10,000–200	Very soluble	Very expensive
Irtran 4	10,000–500	Insoluble	Very expensive
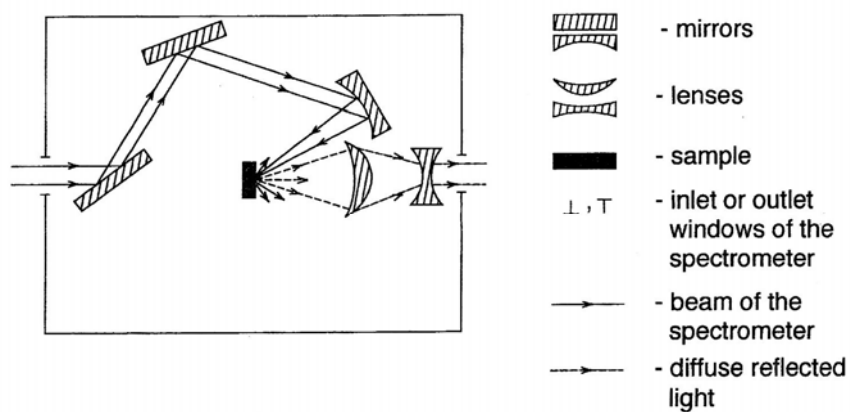
Fig. 7.7 Set up of a diffuse reflectance Fourier transform infrared (DRIFT) spectrometer with integrating lenses system.
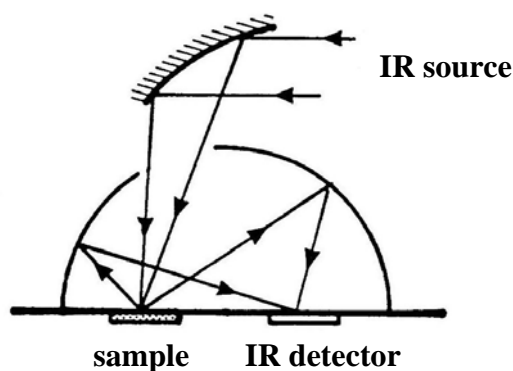

Fig. 7.8 Set up of a diffuse reflectance Fourier transform infrared (DRIFT) spectrometer with integration sphere.

Diffuse reflectance cell

(1) KBr window, (2) sample,

(3) heater, (4) circulation,

(5) thermocouple, (6) vacuum line
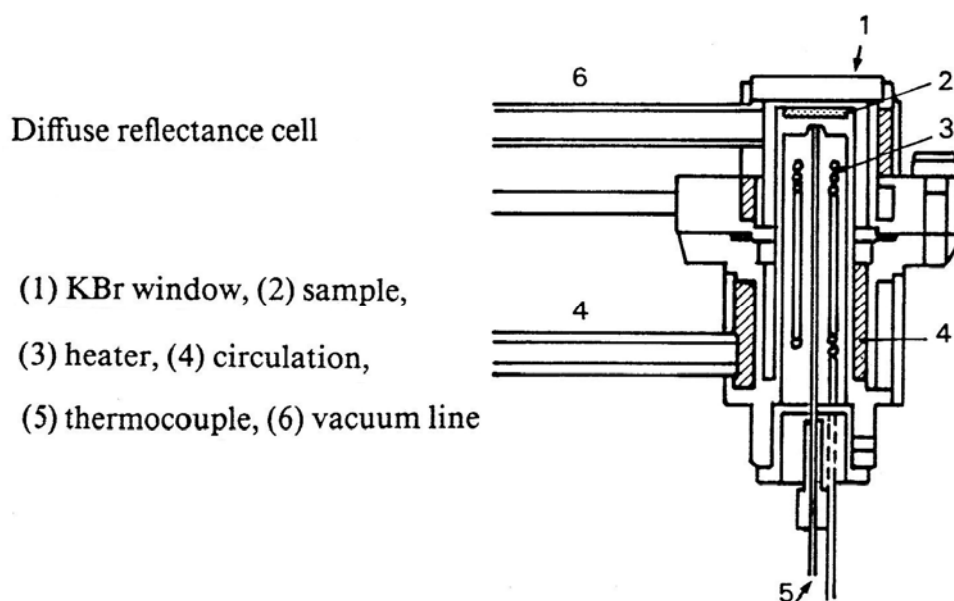
Fig. 7.9 Sample chamber at the bottom of the diffuse reflectance cell shown in Figure 7.8.
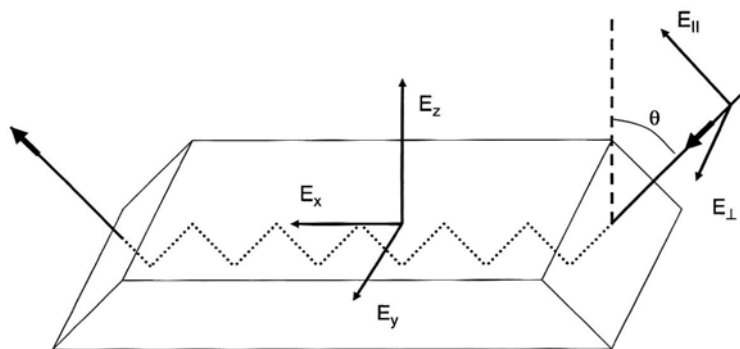
Fig. 7.10 ATR crystal with the electric field components of the incident light ($E_\perp$, $E_\parallel$) and of the internal refractive elements (E_x, E_y, E_z).
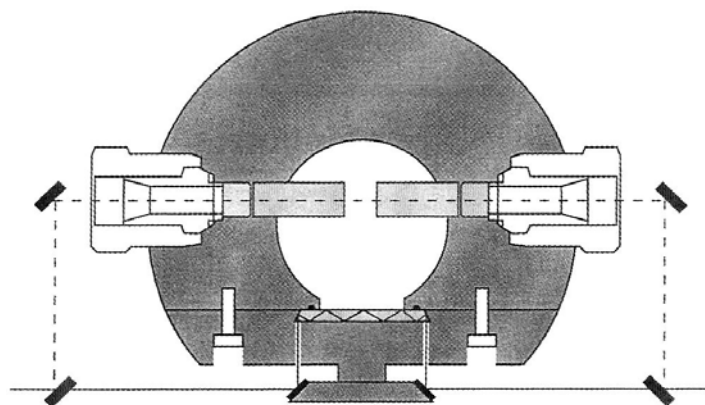
Fig. 7.11 Scheme of an ATR cell. The IR beam can be directed either through the ATR crystal (solid line) or through the transmission windows (dashed line).
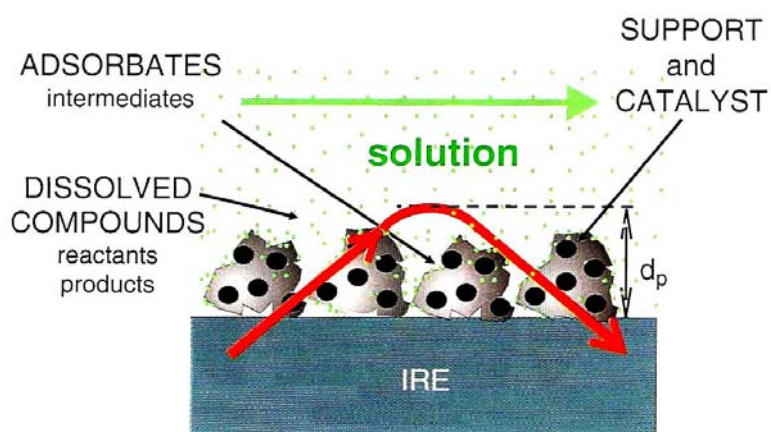
Fig. 7.12 Scheme explaining simultaneous ATR and IR investigations of solid and liquid compounds of a heterogeneous reaction system.

Tab. 7.6 Survey on extinction coefficients, ε, of surface groups and adsorbate complexes on solid catalysts.

Species	Zeolite, adsorbent	Extinction coefficients[a,b] (cm µmol^{-1})[a] or (cm^{2}µmol^{-1})[b]	Remarks	Band (cm^{-1})
Hydroxyl group	H-Y	3.1	HF Brønsted acid site,	3625
		5.3	Y-type zeolite	3650
		7.5		3635
		12.2		3640
Hydroxyl group	H-Y[e], H-X[e]	68.2[b]	HF Brønsted acid site, X-and Y-type zeolite	3640
Hydroxyl group	H-Y	3.1	LF Brønsted acid site,	3550
		3.5	Y-type zeolite	3550
		5.6		3547
		19.9		3550
	H-Y[e]	32.6[b]	Y-type zeolite	3550
	H-X[e]	40.3[b]	X-type zeolite	3550
Hydroxyl group	H-MOR	8.5	Brønsted acid sites in the main channels	3612
	H-MOR	4.25[c]		3605
	H-MOR	3.5		3602
	H-MOR	1.55	Brønsted acid sites in the side pockets	3584
Hydroxyl group	H-FER	4.05	Brønsted acid sites	3604
Hydroxyl group	H-MFI	3.7	Brønsted acid sites	3605
Ammonia (NH$_3\rightarrow$B)	H-Y	0.147[b]	Ammonia bound to Brønsted acid sites, NH$_4^+$	1460
Ammonia (NH$_3\rightarrow$L)	H-Y	0.022[b]	Ammonia bound to Lewis acid sites	1622
Ammonia (NH$_3\rightarrow$B)	H-[Al]MCM-41	1.47	Ammonia bound to Brønsted acid sites, NH$_4^+$	1450
Ammonia (NH$_3\rightarrow$L)	H-[Al]MCM-41	1.98	Ammonia bound to Lewis acid sites	1620
Carbon monoxide (CO$\rightarrow$B)	H-MOR	2.7	Carbon monoxide bound to HF (3612 cm^{-1}) and LF (3585 cm^{-1}) hydroxy groups	2177 (HF) 2169 (LF)
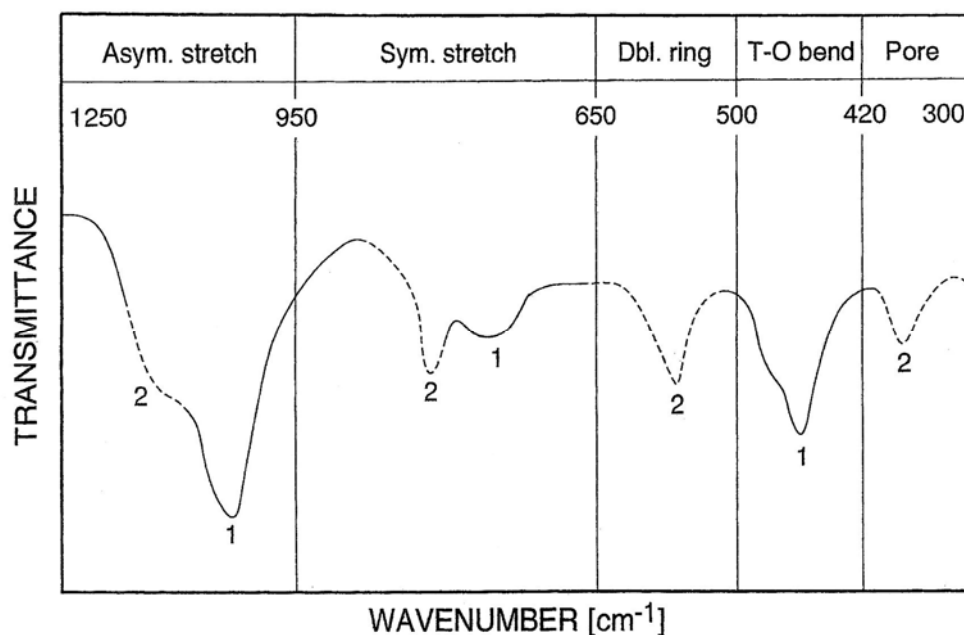
Fig. 7.13 Framework vibrations of crystalline aluminosilicates (solid lines (1): inter-tetrahedral vibrations; broken lines (2): intra-tetrahedral vibrations).
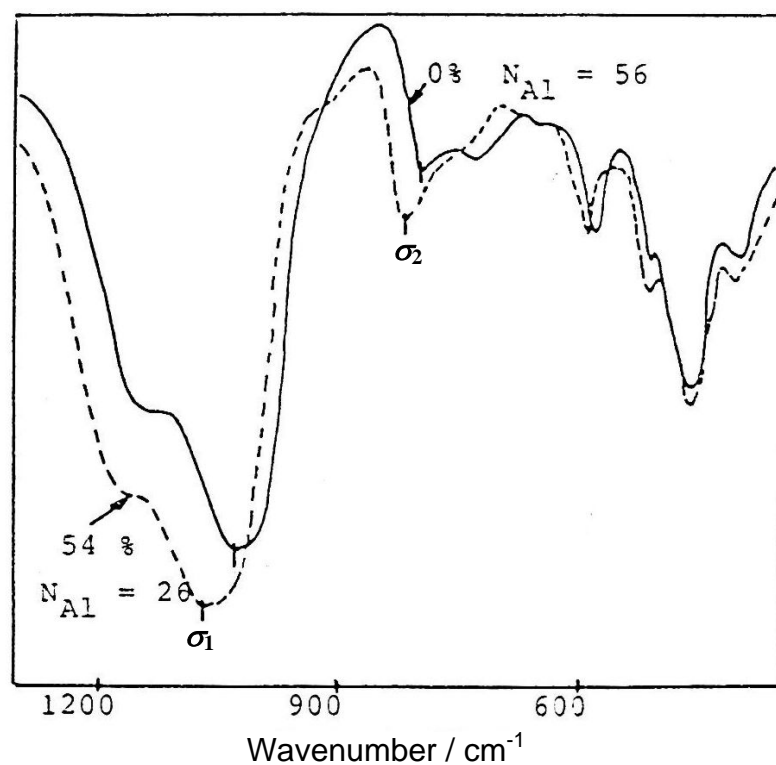
Fig. 7.14 Framework vibrations of zeolites Y with 20 (broken line) and 56 (solid line) aluminum atoms per unit cell.
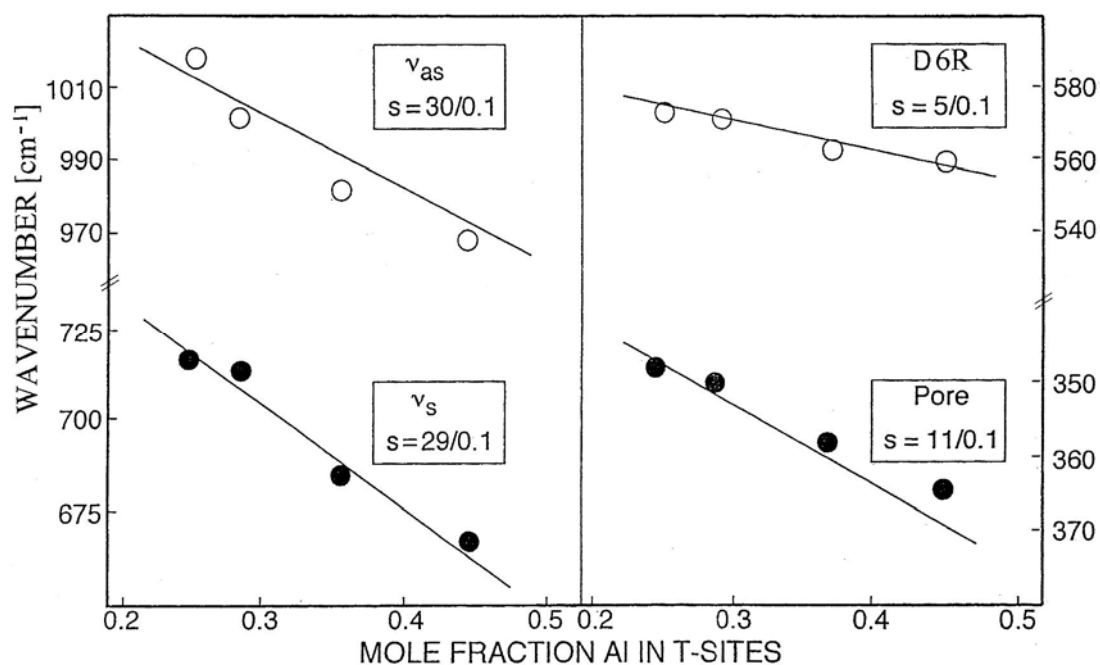

Fig. 7.15 Asymmetric ($\tilde{v}_{as}$) and symmetric ($\tilde{v}_{s}$) stretching vibrations as well as double-6-ring (D6R) and pore opening (Pore) vibrations of faujasite-type zeolites plotted as a function of the aluminum mole fraction.
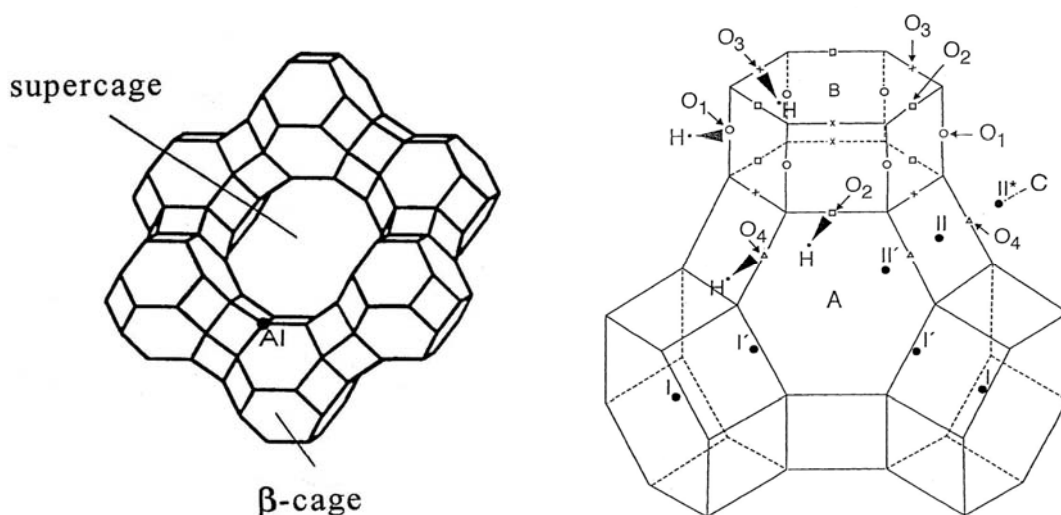
Fig. 7.16 Positions of framework oxygen atoms in faujasite-type zeolites and hydroxyl protons bound to these sites (bridging OH groups).

(1) ν_{OH}; (2) δ_{OH}; (3) γ_{OH}; (4) δ_{OTO}; (5) ν_{TO}, symmetrical; (6) ν_{TO}, asymmetrical; T = Si, Al
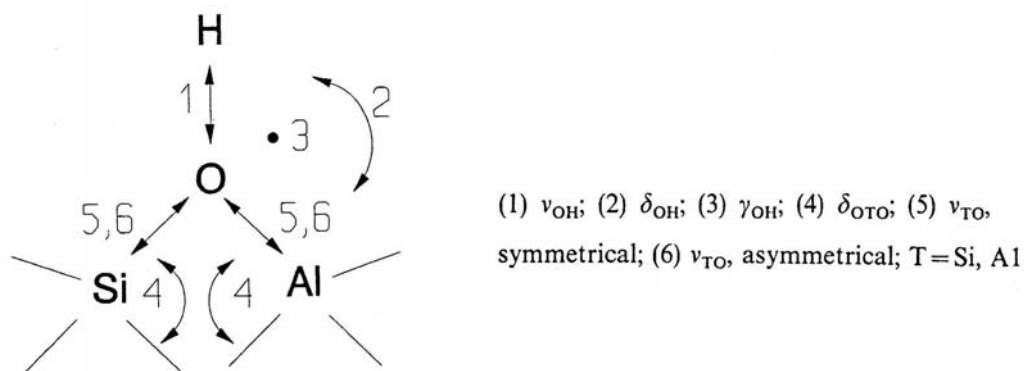
Fig. 7.17 Vibration modes in the local structure of bridging OH groups in acidic zeolites.
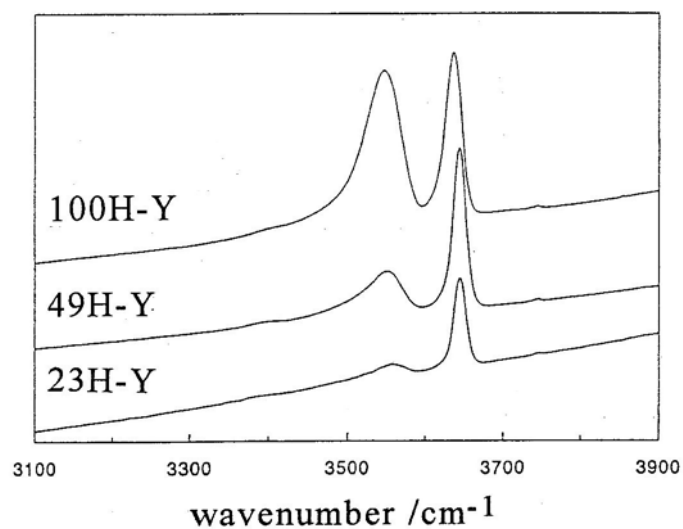
Fig. 7.18 O-H stretching vibrations ($\tilde{\nu}_{OH}$) of bridging OH groups in acidic zeolites H-Y with different cation exchange degrees.

Tab. 7.7 Survey on the different vibration modes in the local structure of bridging OH groups and of lattice vibrations of acidic zeolites H-Y and their combination modes.

v_{01}		γ		δ		δ_{OTO} [6,11] 470	$v_{TO,s}$ [6,11] 765	$v_{TO,as}$ [6,11] 1130	Calculated	Measured
lf 3548	hf 3640	lf 402	hf 310	lf 1057	hf 1028					
×		×								3950
	×		×							3950
×				×						4605
	×				×					4668
×						×			4018	in $v+\gamma$
	×					×			4110	4100
×							×		4318	4309
	×						×		4405	4392
×								×	4678	in $v+\delta$
	×							×	4770	in $v+\delta$
×						×	×		4783	in $v+\delta$
	×					×	×		4875	4855
×						×		×	5148	—a
	×					×		×	5240	—a
×		2×							4352	in $v+\delta_{OTO}$
	×		2×						4260	*ca.* 4200
×		×		×					5007	4950
	×		×		×				4978	4950
×				2×					5662	5670
	×				2×				5696	5670
×		2×		2×					6466	*ca.* 6500
	×		2×		2×				6316	*ca.* 6500

aOverlapped by bands due to atmospheric water vapour.
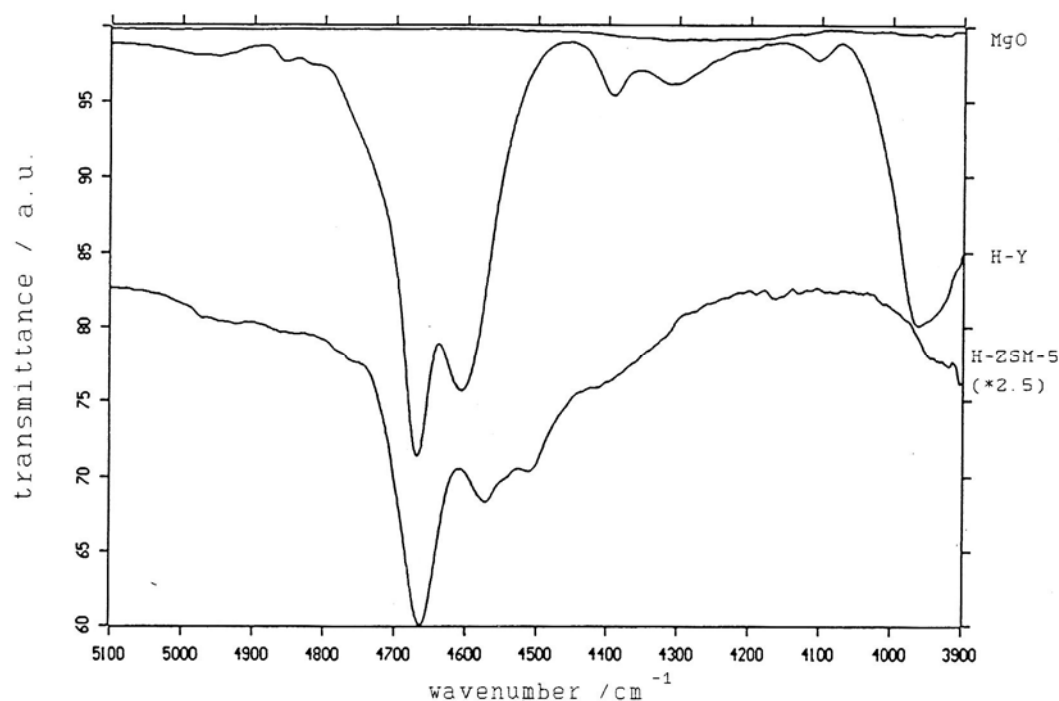
Fig. 7.19 NIR spectra of MgO and zeolites H-Y and H-ZSM-5 in the range of combination vibrations.
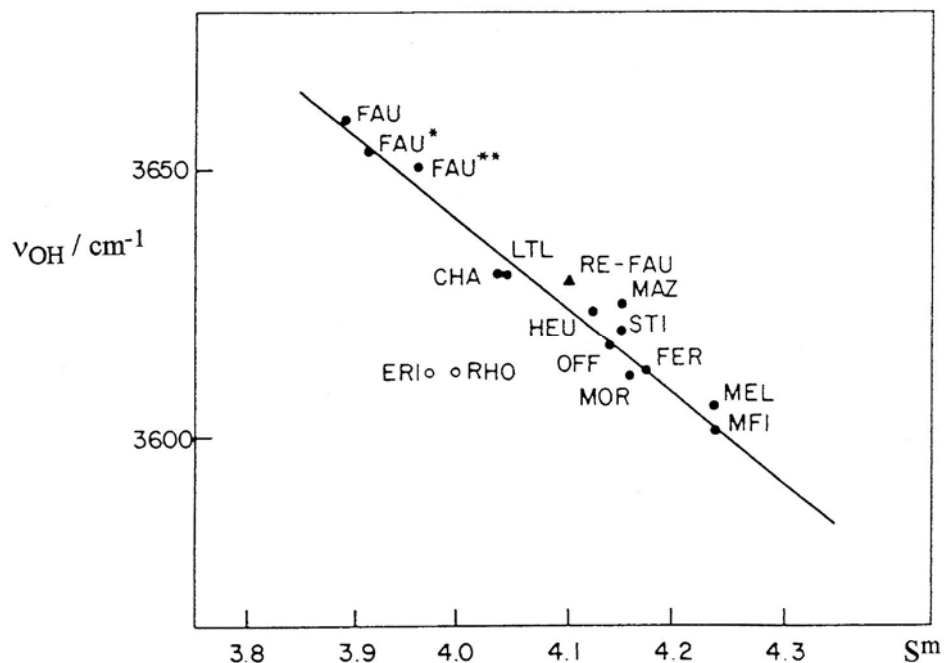
Fig. 7.20 Plot of the O-H stretching vibrations ($\tilde{v}_{OH}$) of bridging OH groups in acidic zeolites as the function of the mean Sanderson electronegativity S^m.
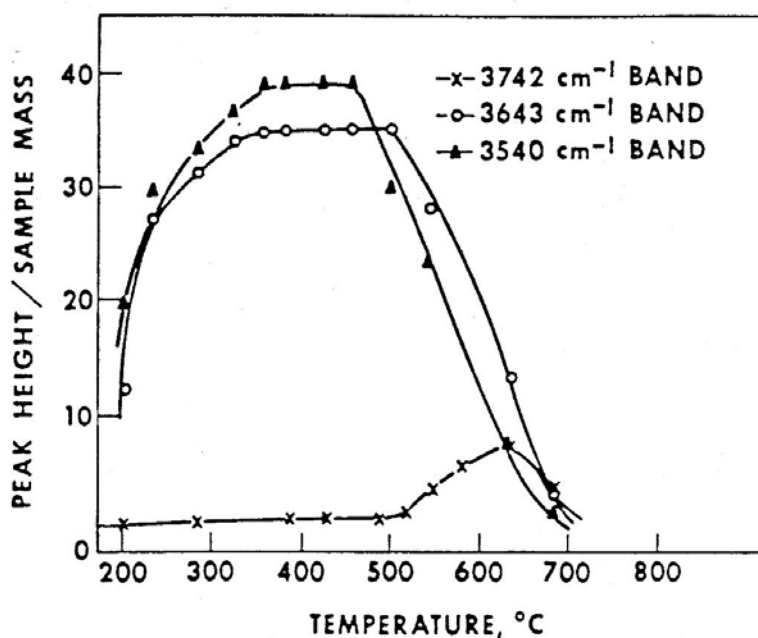
Fig. 7.21 Band intensities of O-H stretching vibrations ($\tilde{v}_{OH}$) of bridging OH groups in acidic zeolites H-Y upon calcination at 473 to 973 K.
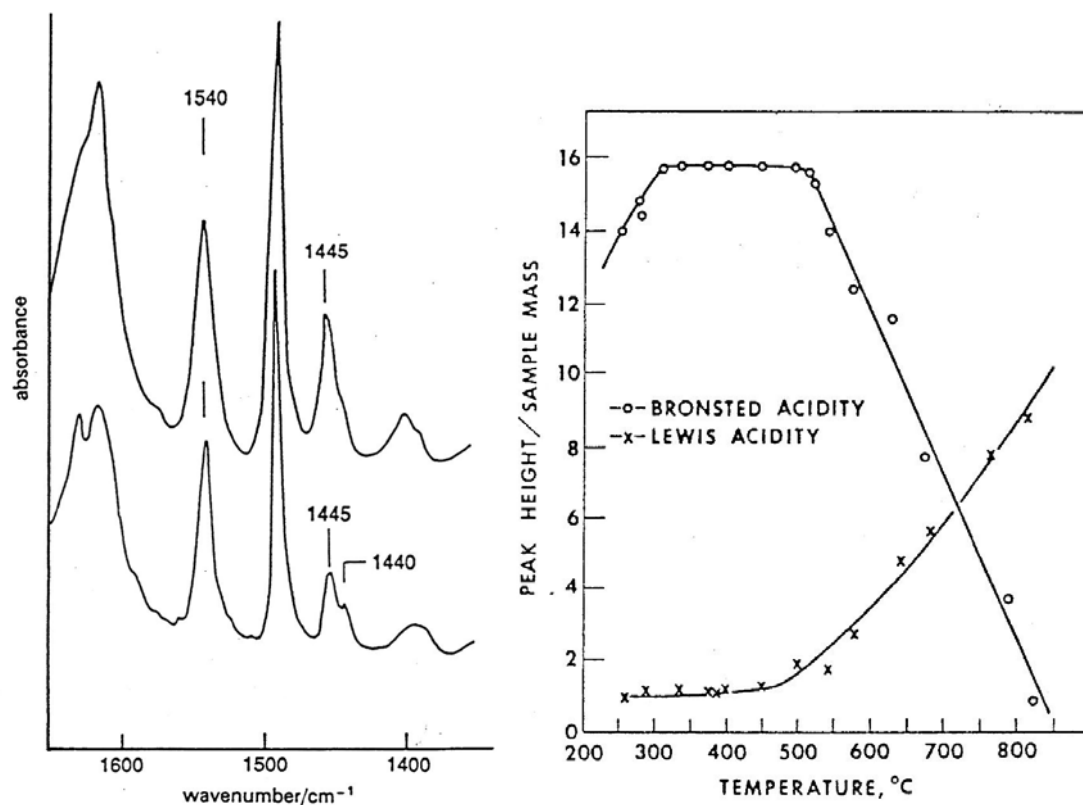
Fig. 7.22 FTIR spectra of pyridine adsorbed on zeolites H-Y (left) and plot of the intensities of IR bands due to pyridine interacting with Brønsted (1540 cm^{-1}) and Lewis (1445 cm^{-1}) acid sites (right).
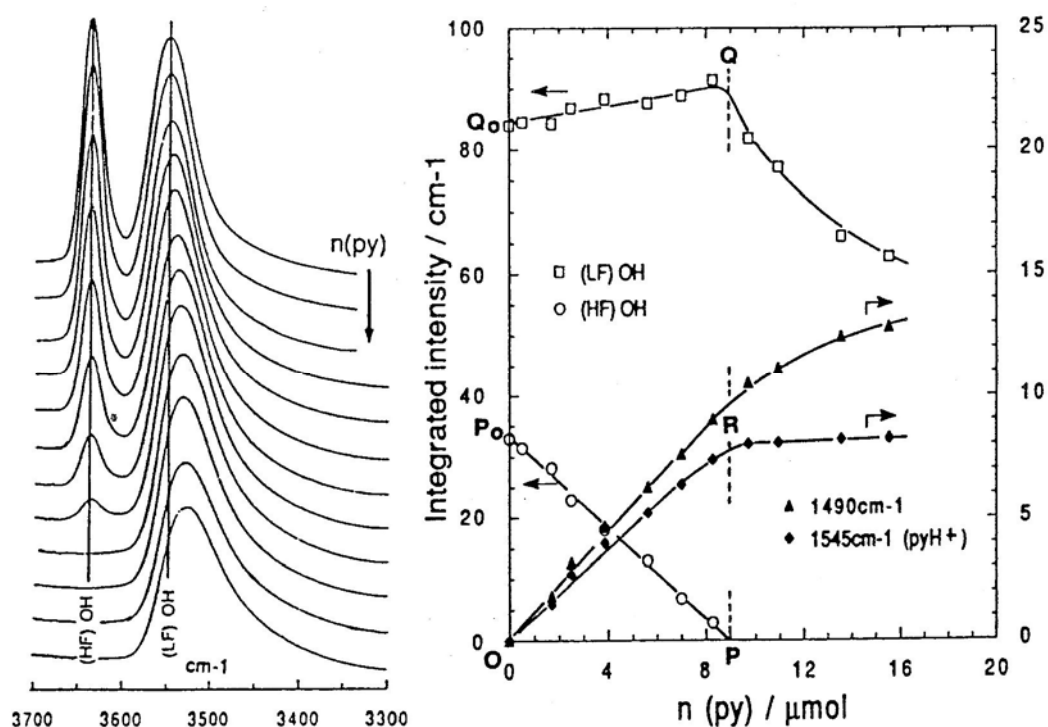
Fig. 7.23 O-H stretching vibrations of a zeolite H-Y upon stepwise adsorption of pyridine (left) and plot of the intensities of the IR bands due to LF and HF bands as well as pyridine interacting with Brønsted (1540 cm^{-1}) and Lewis (1445 cm^{-1}) acid sites (right).
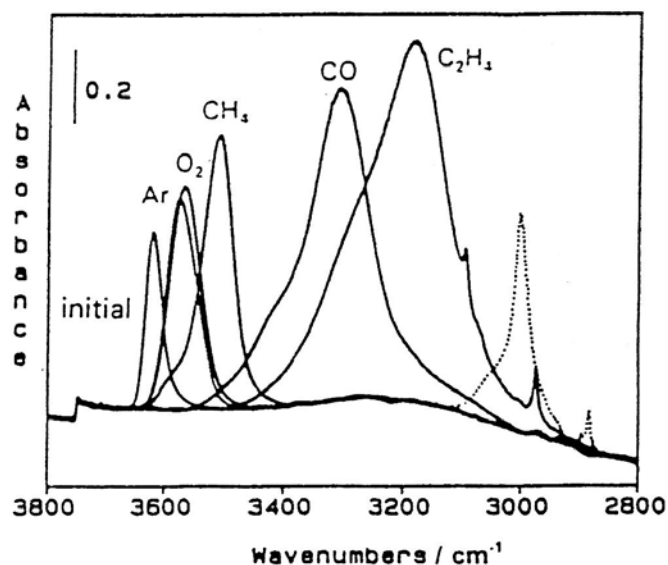
Fig. 7.24 FTIR spectra of acidic zeolites H-ZSM-5 recorded upon loading of probe molecules with different basicities.
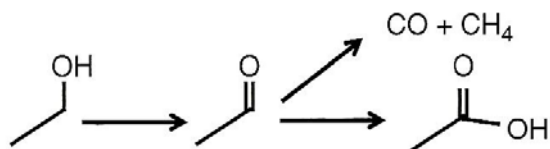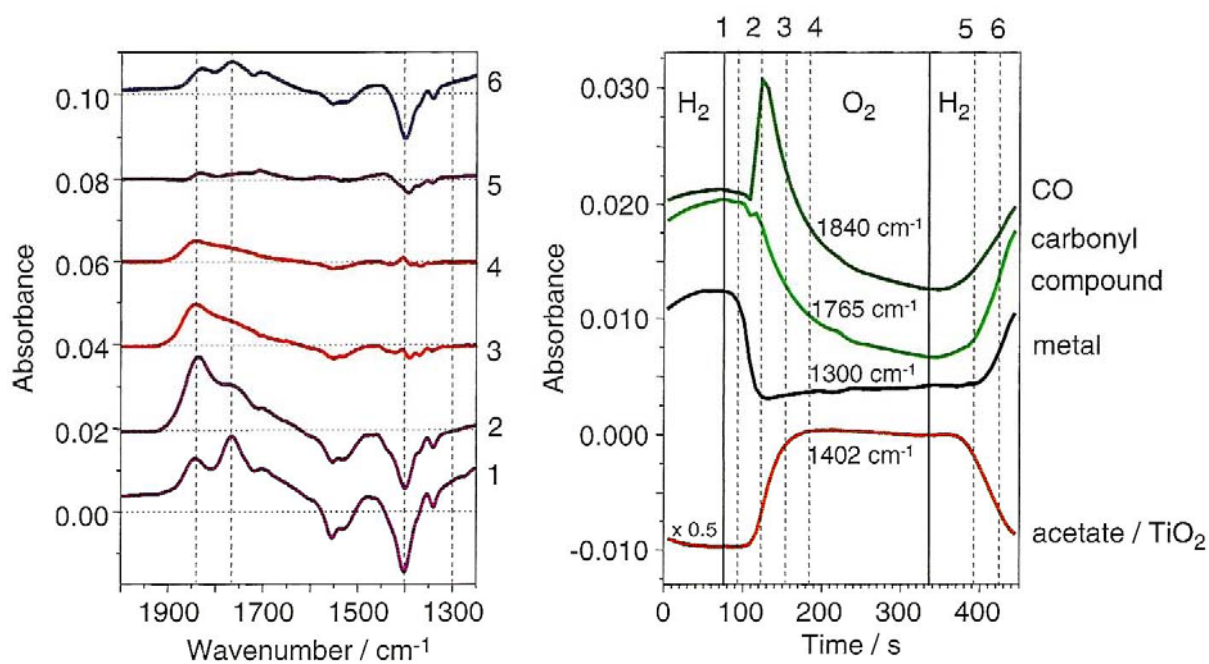
Fig. 7.25 ATR signals recorded during the ethanol oxidation at 298 K on a 5%Pd/TiO$_2$ catalyst recorded at different reaction times (points 1 to 6 at the right-hand side). At $t = 75$ s, the solvent flow was switched from hydrogen-saturated ethanol to oxygen-saturated ethanol and vice versa at $t = 335$ s.
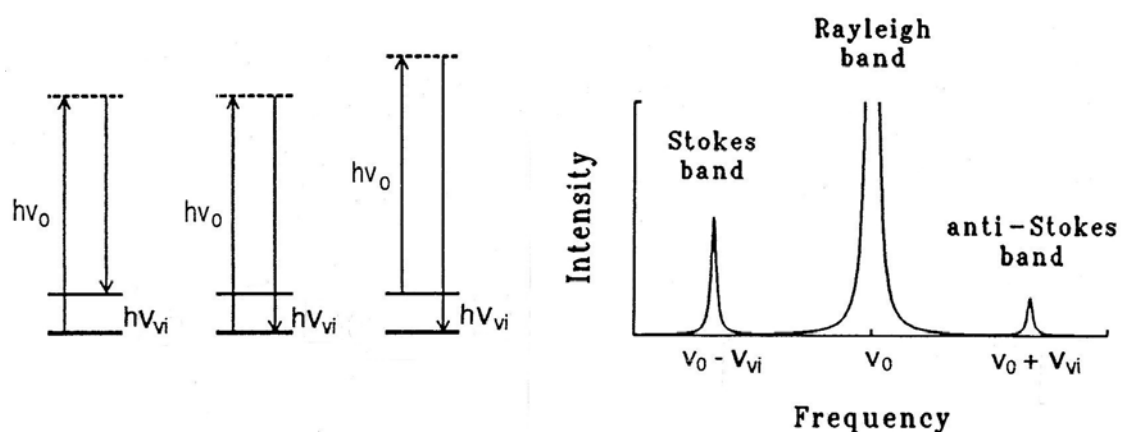
Fig. 7.26 Principles of the formation of Stokes and anti-Stokes bands in Raman spectroscopy.
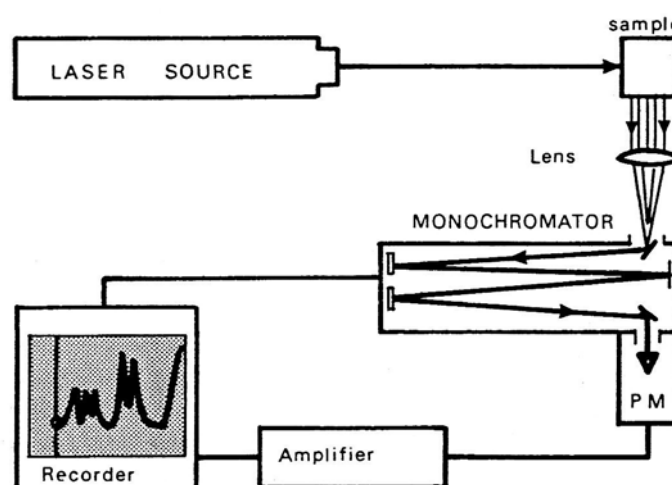
Fig. 7.27 Set up of a Raman spectrometer.
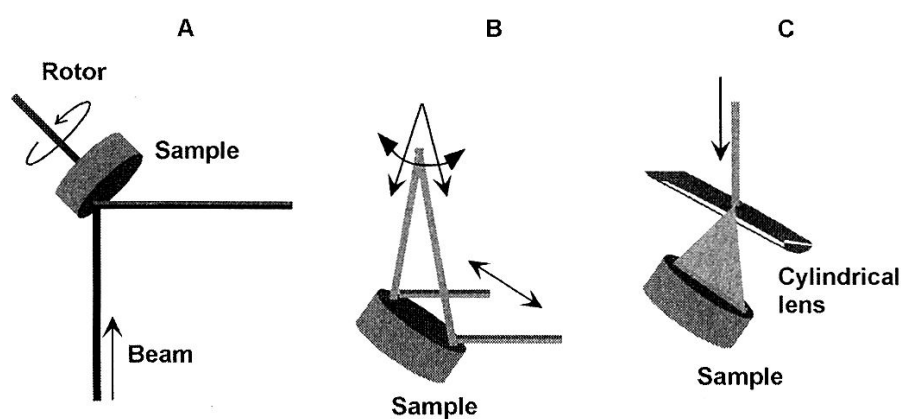
Fig. 7.28 Techniques for minimizing the local sample heating by sample rotation (A), motion of the Laser beam (B), and a cylindrical lens (C).
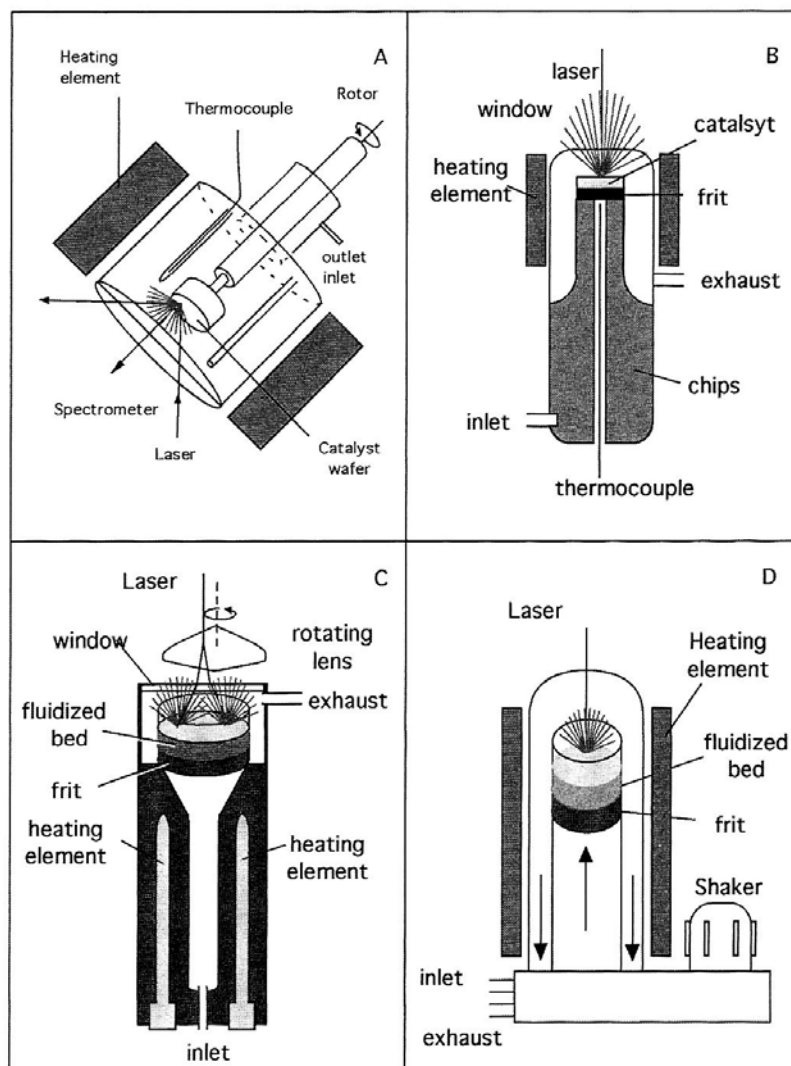
Fig. 7.29 In situ Raman cells for investigations under reaction conditions.
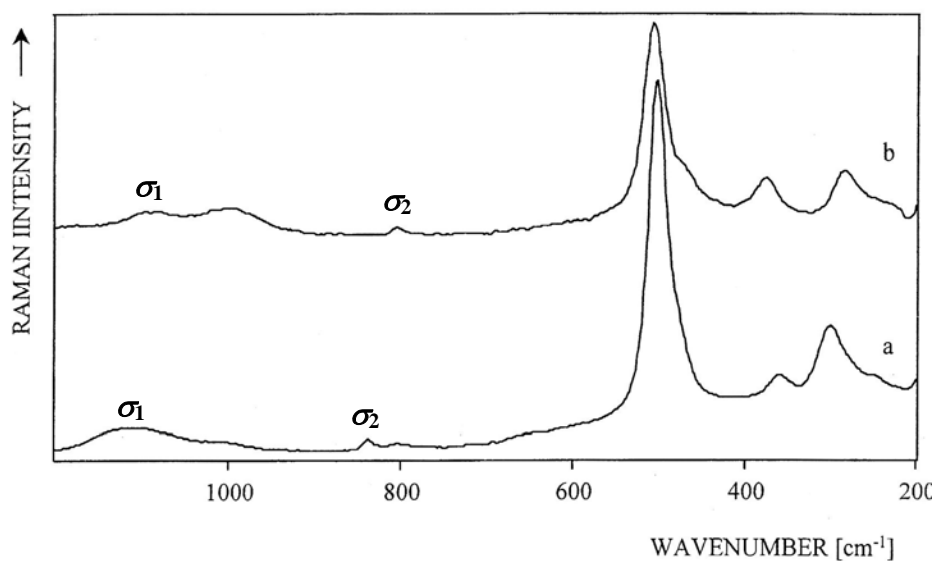
Fig. 7.30 Raman spectra of zeolites (a) Na-Y (Si/Al = 2.6) and (b) Na-X (Si/Al = 1.18).
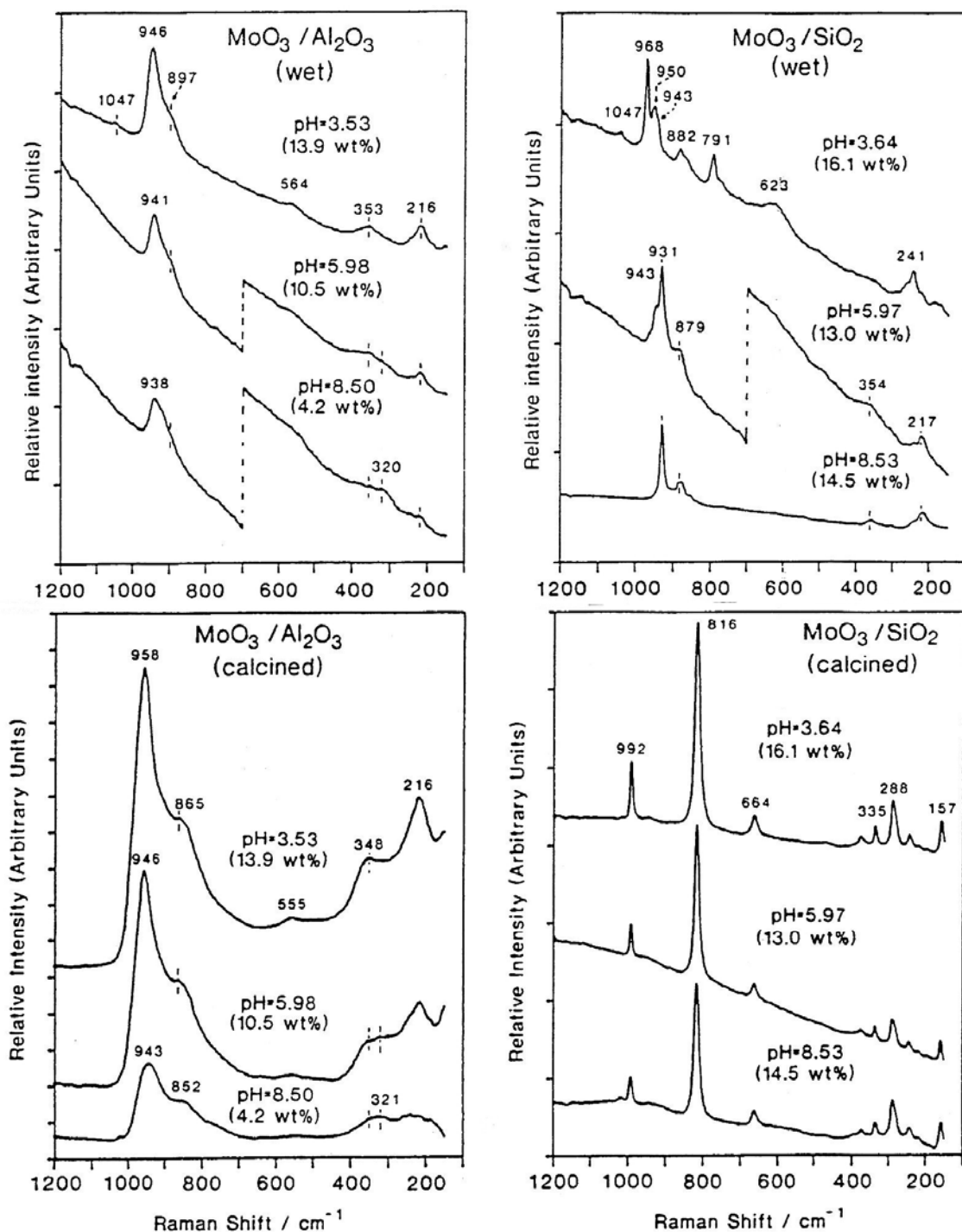
	$(NH_4)_6Mo_7O_{24} \cdot 4 H_2O$	$Mo_7O_{24}^{6-}$	$Mo_8O_{26}^{4-}$	MoO_4^{2-}
ν_s (Mo=O)	931	943	965	897
ν_{as} (Mo=O)	879	903	925	837
δ (Mo=O)	354	362	370	317
ν (Mo-O-Mo)		564	860	
δ (Mo-O-Mo)	217	219	230	

Fig. 7.31 Raman spectra of MoO_3/Al_2O_3 (left) and MoO_3/SiO_2 (right) catalysts before (top) and after (bottom) calcination at 775 K in air. The table gives a summary of the observed bands and their assignments.
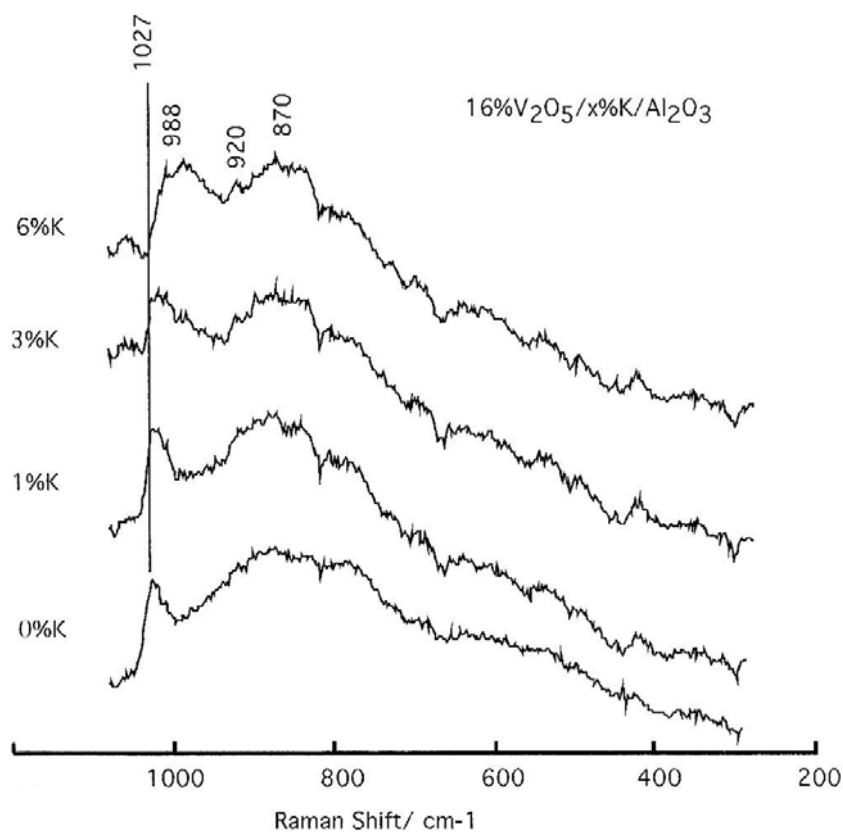
Fig. 7.32 Raman spectra of 16%V_2O_5/Al_2O_3 catalysts co-impregnated with different amounts of potassium hydroxide (x%K).
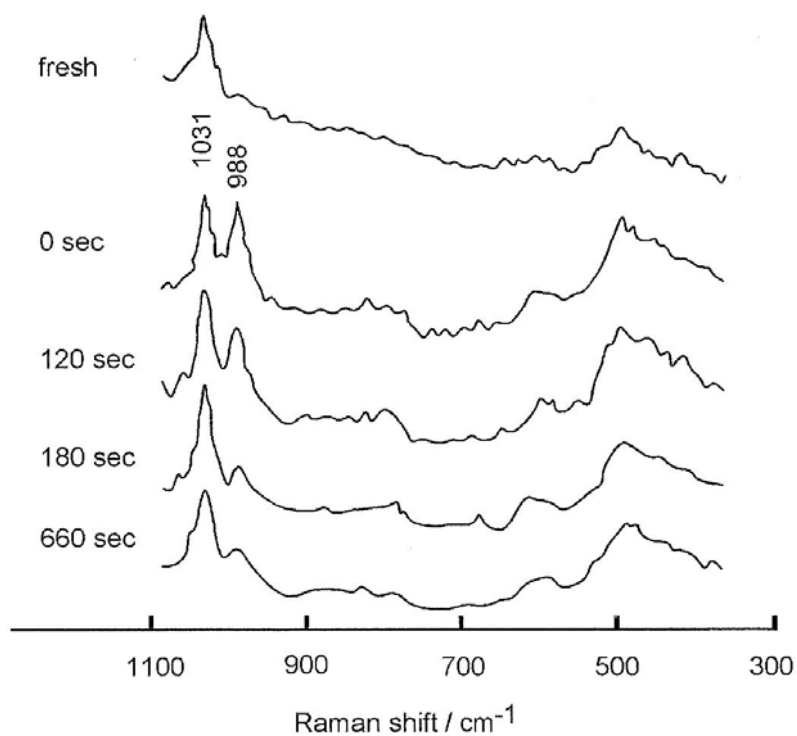
Fig. 7.33 Raman spectra of a 2%V_2O_5/SiO_2 catalyst before (fresh) and after treatment with $^{18}O_2$ (0 sec) and during ethane oxidation for maximum 11 minutes.
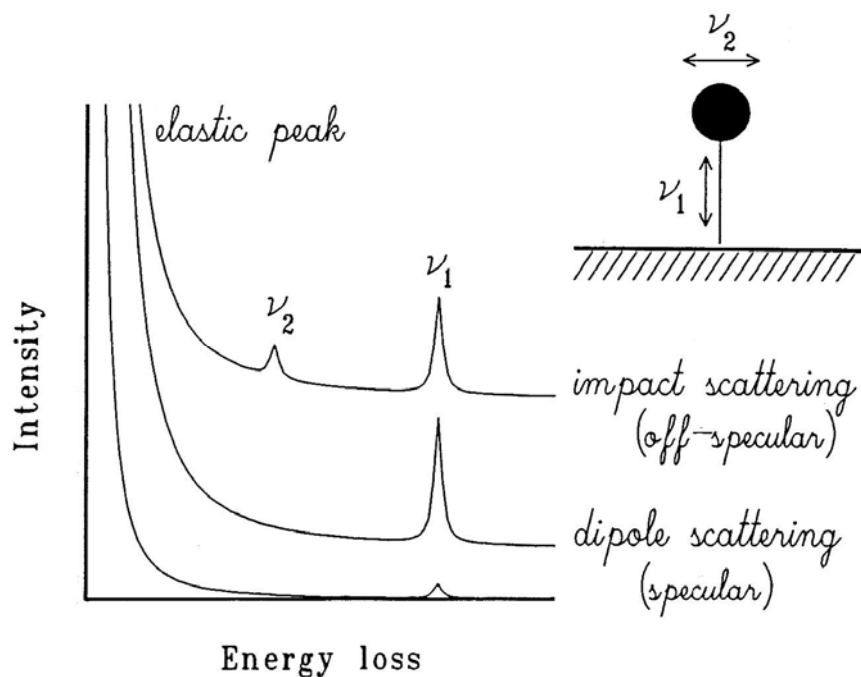
Fig. 7.34 Excitation mechanisms in electron energy loss spectroscopy (EELS): Dipole scattering (ν_1) and impact scattering (ν_1 and ν_2).
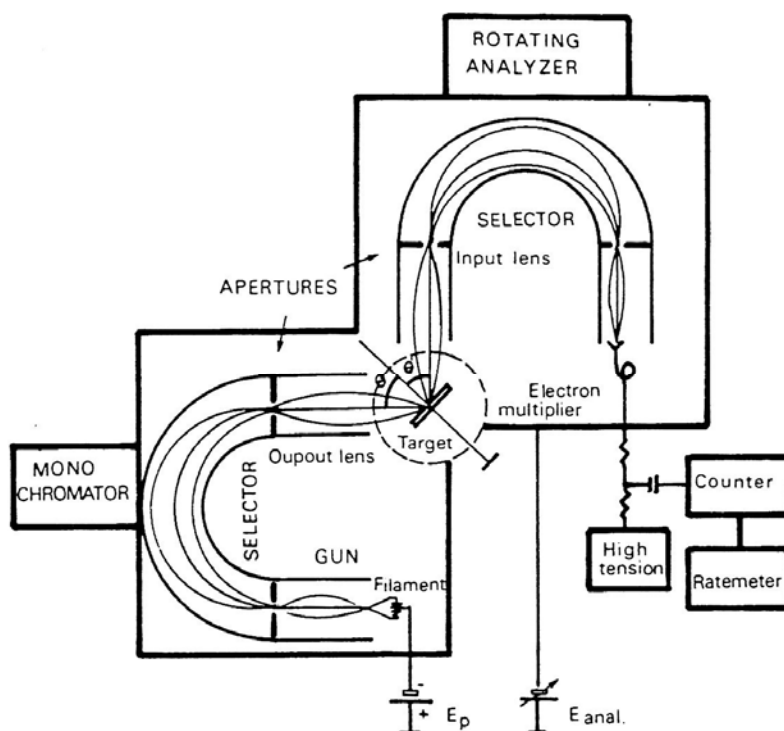
Fig. 7.35 Scheme of a high-resolution EELS spectrometer with hemispherical selectors.
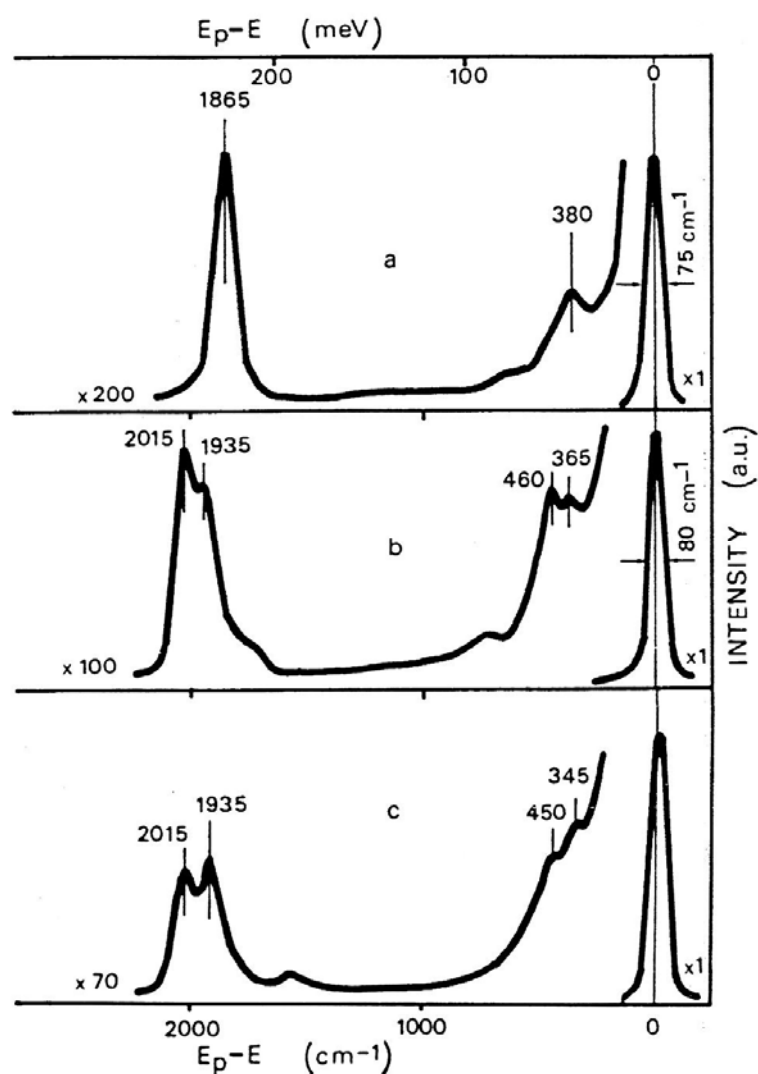
		Energy, cm^{-1}				
Surface		Ni(111)		Ni(100)		Ni(110)
Coverage θ_{CO}		Low	0.5	Low	0.5	Low	0.5
$\begin{array}{c}O\\ \mid\\ C\\ \mid\\ Ni\end{array}$ ν_{CO}				2000	2015	1990	2015
$\nu_{M\text{-}CO}$					460		~450
$\begin{array}{c}O\\ \mid\\ C\\ /\ \backslash\\ Ni\ Ni\end{array}$ ν_{CO}		1815	1910	1900	1935	1880	1935
$\nu_{M\text{-}CO}$		380	380		365		~345

Fig. 7.36 EELS spectra (top) of CO adsorbed at 300 K on (a) Ni(111), $\theta_{CO} = 0.2$; (b) Ni(100), $\theta_{CO} = 0.5$, and (c) Ni(110), $\theta_{CO} = 0.5$, as well as assignment of the observed bands (bottom).

8. UV/Vis and EPR spectroscopy

Tab. 8.1 Notations of electron transitions.

System	Symbols Ground state	Symbols Excited state	Examples	Correspondence
Kasha (MO representation)	σ, π, n	σ^*, π^*	$\sigma \to \sigma^*$ $\pi \to \pi^*$ $n \to \pi^*$ $n \to \sigma^*$	
Mulliken	N	Q, V, R	$V \leftarrow N$ $Q \leftarrow N$ $R \leftarrow N$	$\pi \to \pi^*$ or $\sigma \to \sigma^*$ $n \to \pi^*$ or $n \to \sigma^*$ Rydberg transition
Group theory	Irred. repr. incl. multiplicity	Irred. repr. incl. multiplicity	${}^1A_1 \leftarrow {}^1A_1$ ${}^1B_2 \leftarrow {}^1A_1$ ${}^1E_{1u} \leftarrow {}^1A_{1g}$	
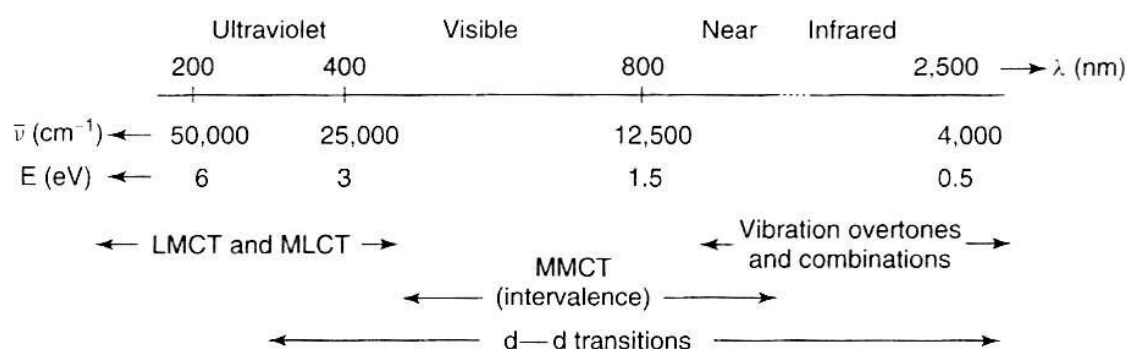
Fig. 8.1 Ultraviolet (UV), visible (Vis), and near-infrared (NIR) regions and assignments of the vibration and electron transitions.
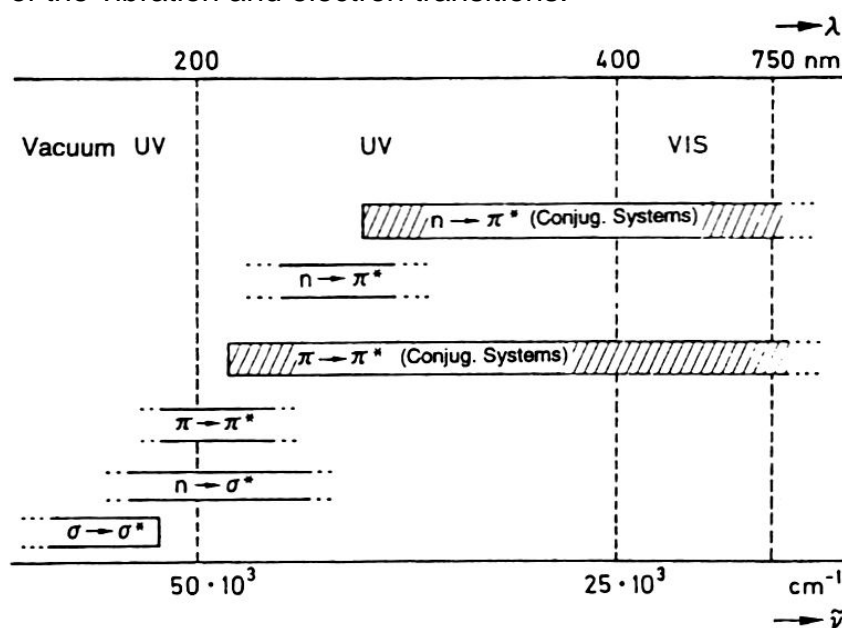
Fig. 8.2 Electron transitions in the ultraviolet (UV) and visible (Vis) ranges.
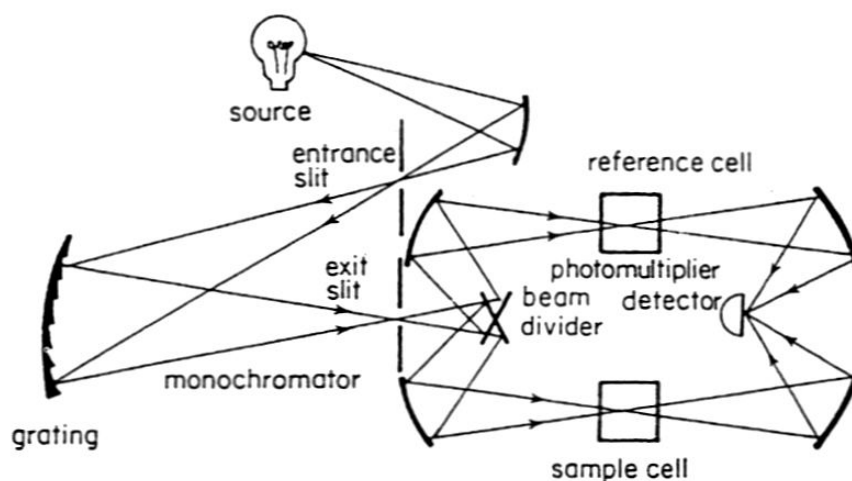
Fig. 8.3 Set up of a double-beam dispersive spectrometer. The grating, which is the dispersive element, selects the wavelength in front of the entrance into the sample cell.
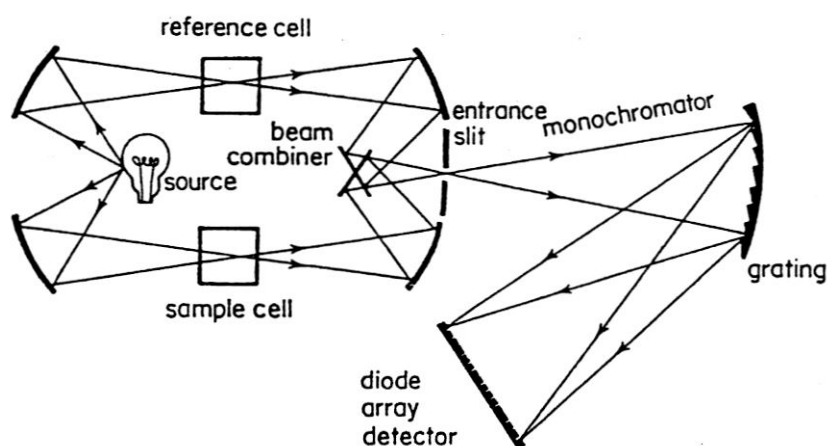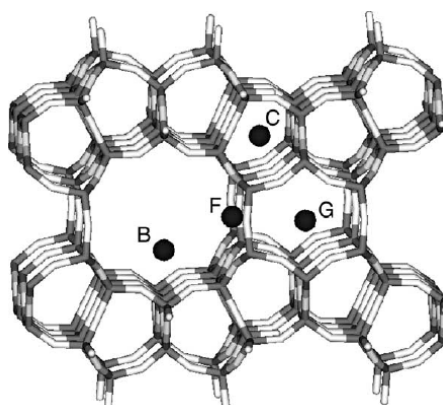

Fig. 8.4 Set up of a double-beam diode array spectrometer. The grating is arranged between the sample cell and the diode array.
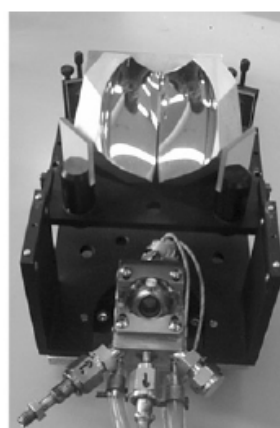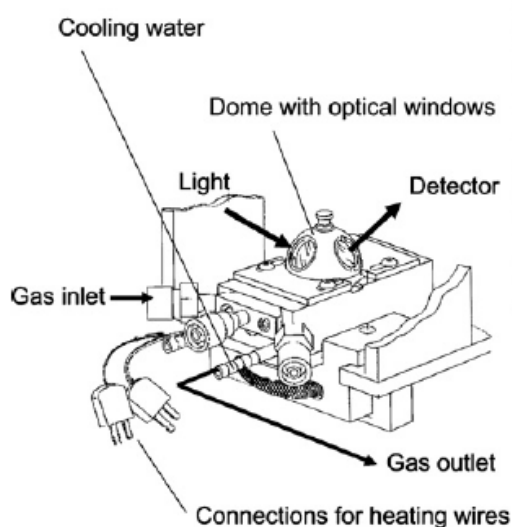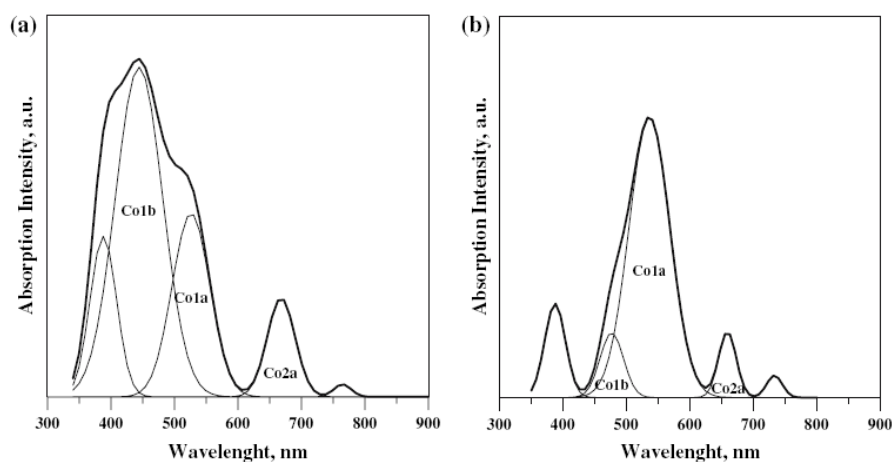

Fig. 8.5 Set up of a Praying Mantis UV/Vis sample cell for recording spectra of solid catalysts under working conditions.
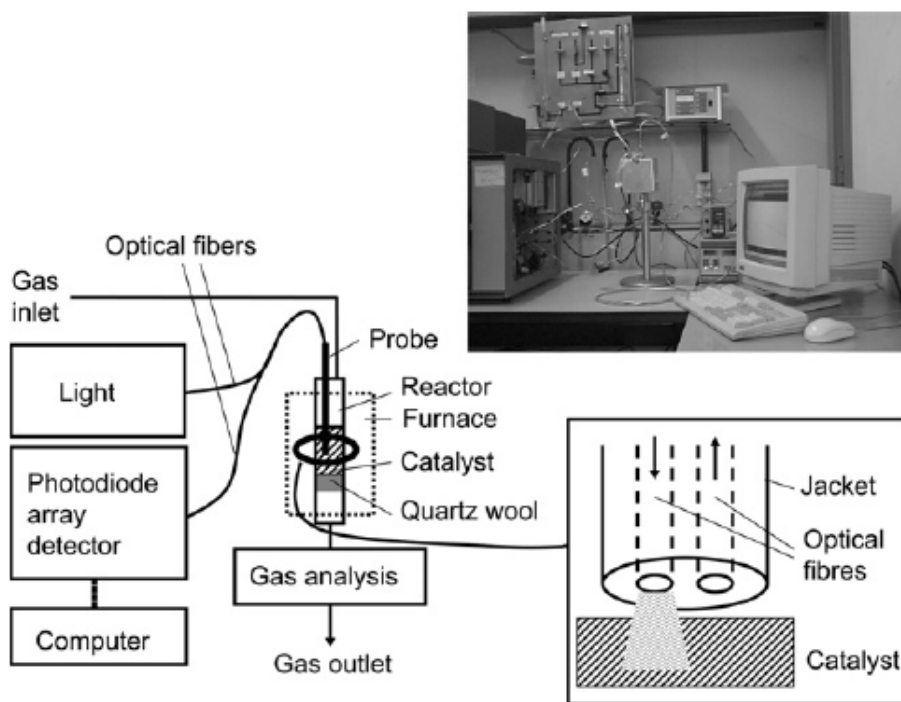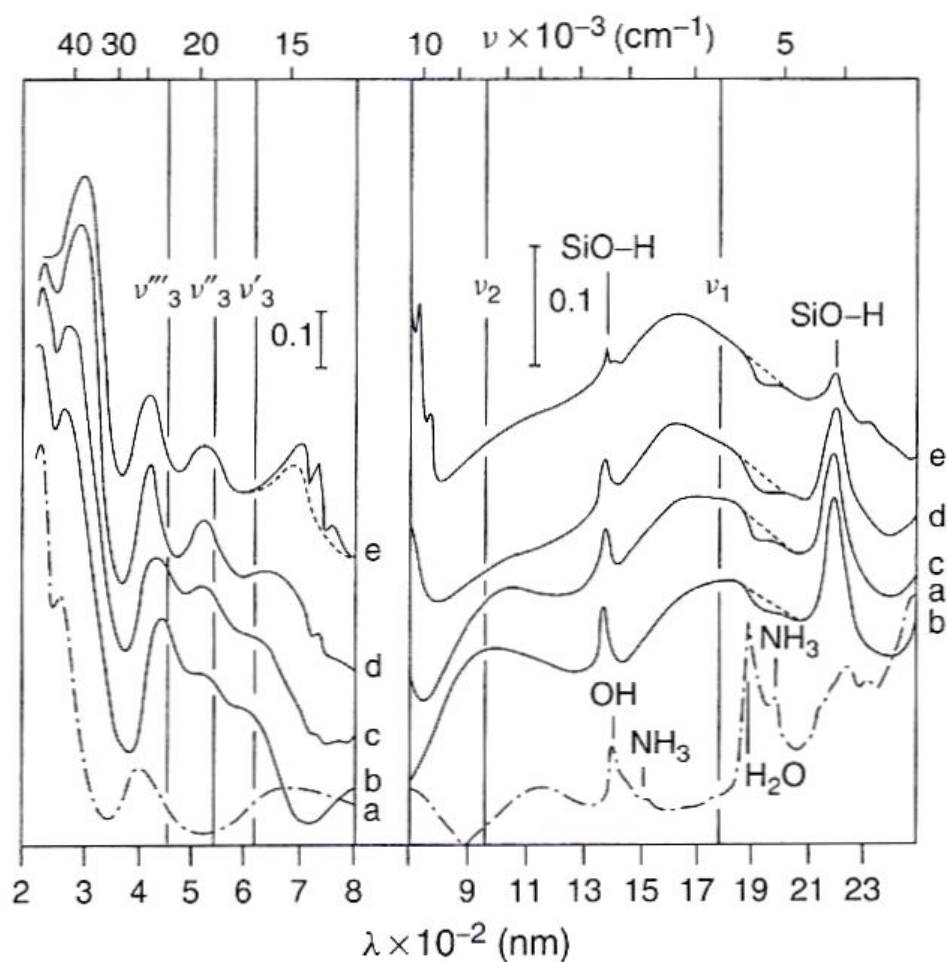
Fig. 8.6 Set up of a fixed-bed reactor equipped with a glass-fiber optics for on-line UV/Vis spectroscopy.

Fig. 8.7 Location of the extra-framework sites B, C, F, and G in ferrierite (FER). The view is directed along the 10-ring channels.

Fig. 8.8 UV/Vis spectra of Co-FER zeolite recorded before (a) and after (b) conversion of a mixture of NO, NO_2, CH_4, and O_2 in helium at 1073 K.

Fig. 8.9 UV/Vis and NIR spectra of Ni(NH₃)₆²⁺ complexes recorded after deposition on silica and further drying at 353 K (a), calcination in oxygen at 773 K (b), evacuation at 773 K for 1 h (c) or 15 h (d), and evacuation at 973 K (e).

Tab. 8.2 d-d transitions of Ni²⁺ model compounds (a: estimated value).

Complex	$\tilde{v}_1/cm^{-1}$	$\tilde{v}_2/cm^{-1}$	$\tilde{v}_3/cm^{-1}$
$Ni(H_2O)_6^{2+}$	8500	13800	25300
$Ni(NH_3)_6^{2+}$	10750	17500	28200
$NiCl_6^{4-}$	7700	12700	22600
$NiCl_4^{2-}$	$(3500)^a$	6550	14250
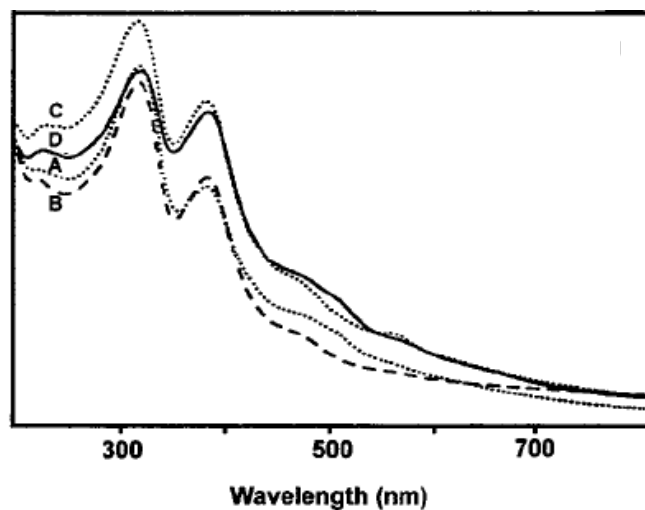
Fig. 8.10 UV/Vis spectra of zeolite La,H-Y recorded after conversion of 1-butene and isobutane in a ratio of 1 : 9 under batch conditions at 523 K (A), 623 K (B), 673 K (C), and 773 K (D).
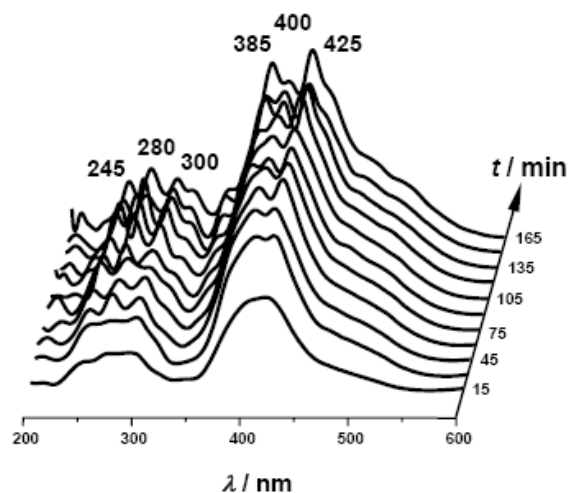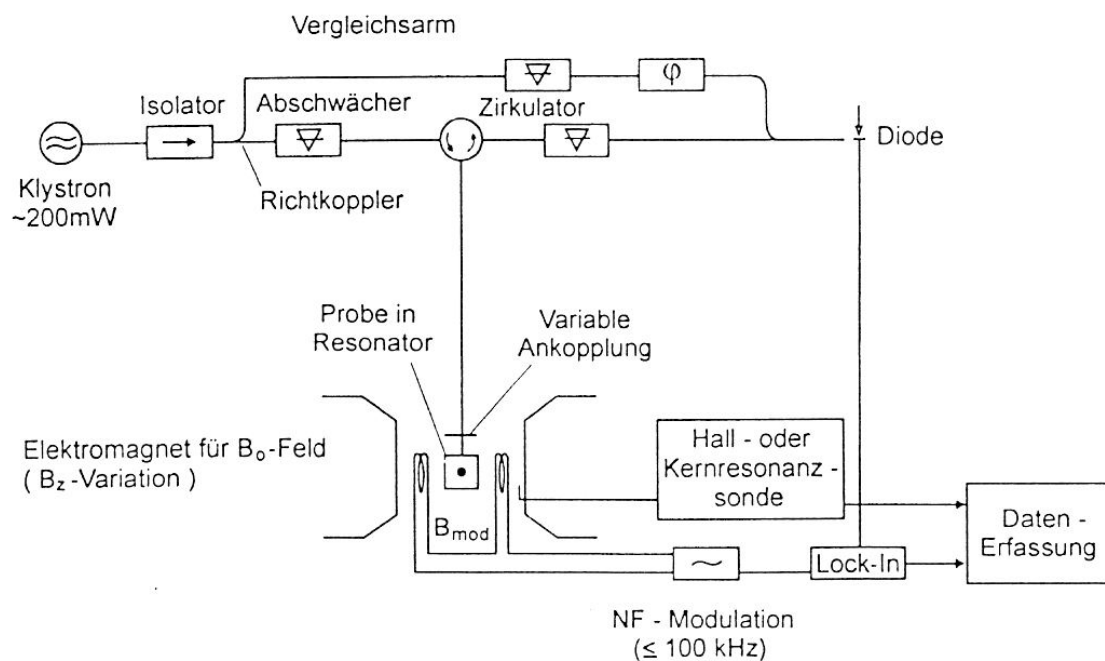

Fig. 8.11 Stack plot of UV/Vis spectra recorded during conversion of methanol on SAPO-34 at 673 K for 165 minutes.
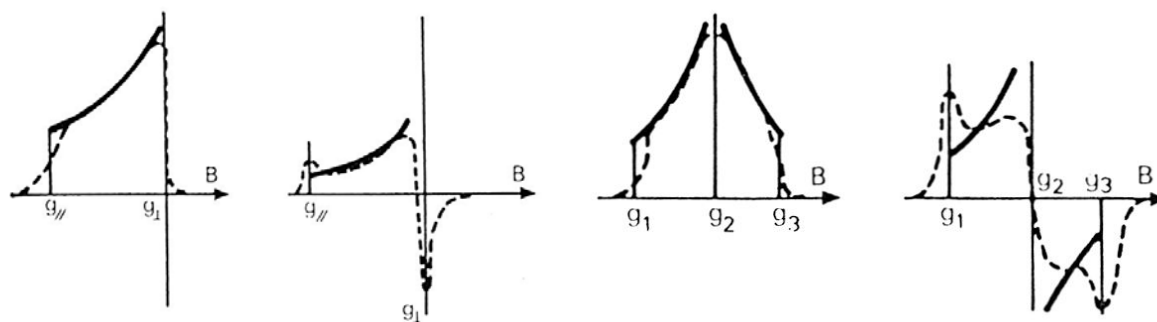
Fig. 8.12 Absorption and first-derivative powder EPR signals in the case of an axial (left) and orthorhombic symmetry (right).
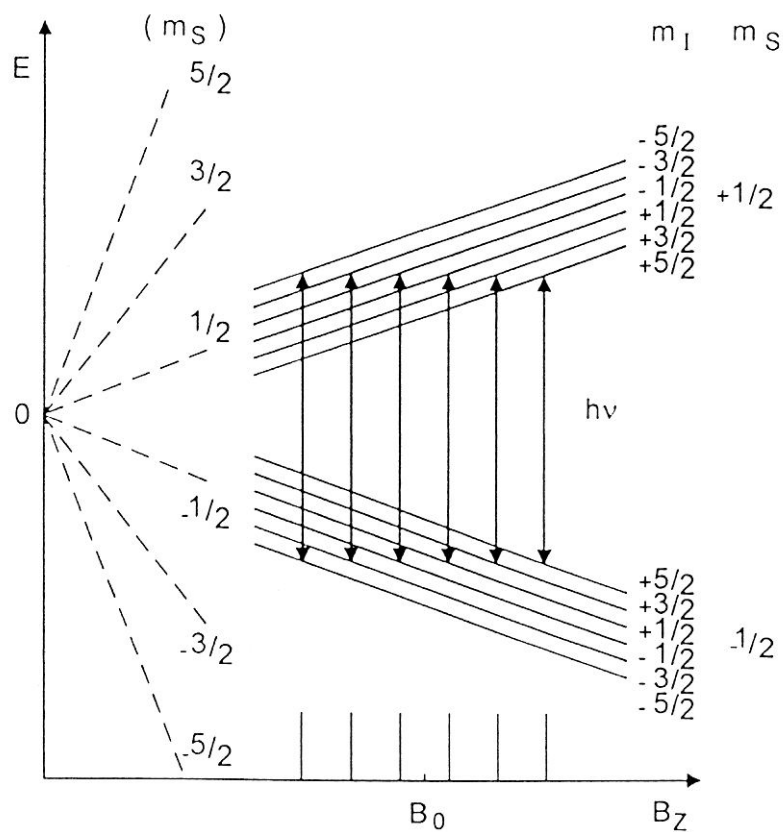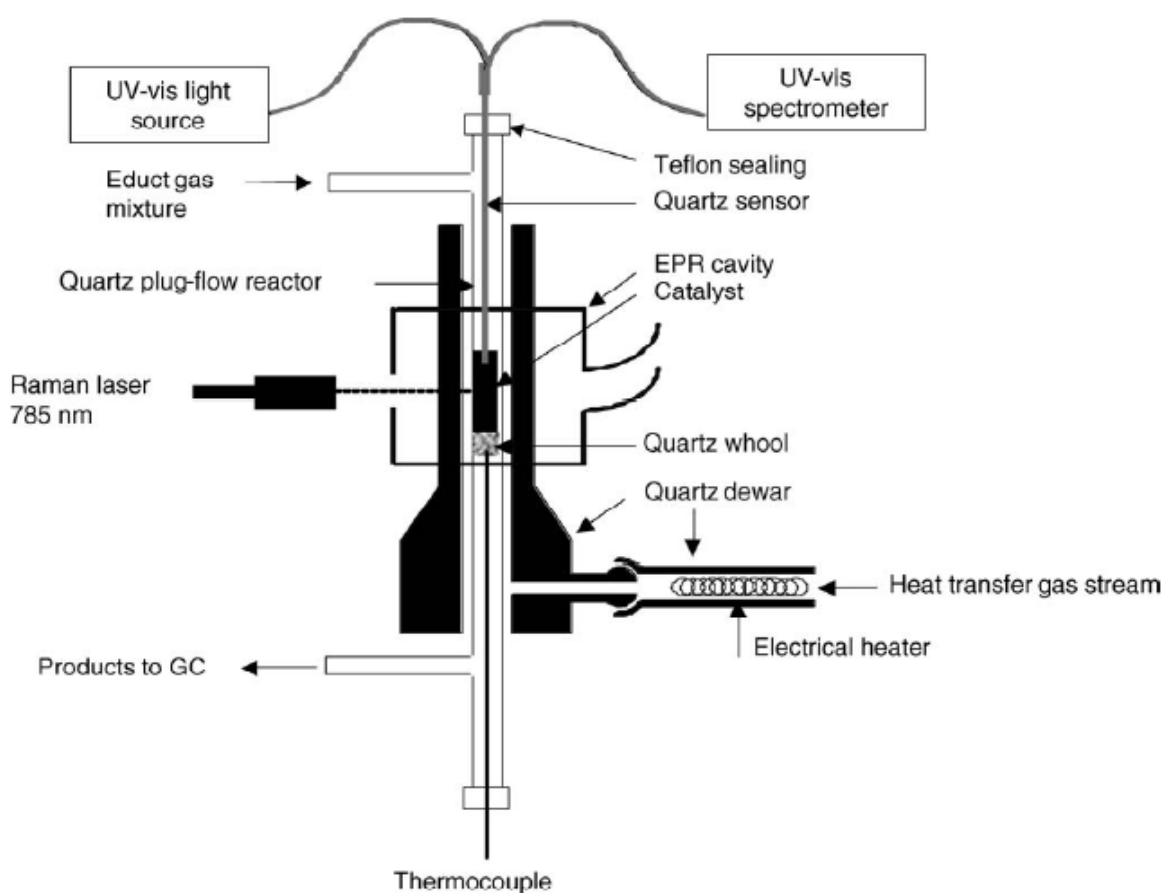
Fig. 8.13 Hyperfine coupling of Mn^{2+} ($S = 5/2$, $I = 5/2$, $g = 2$, $A < 0$).
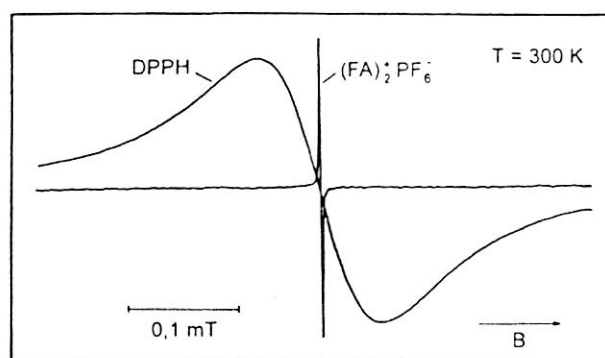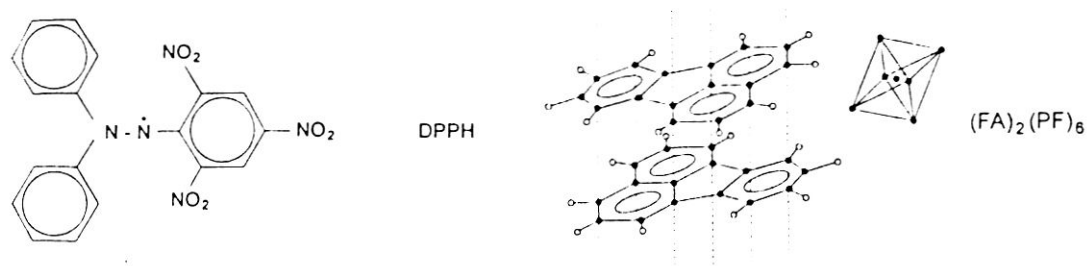

Fig. 8.14 Scheme of an EPR spectrometer with microwave bridge.

Tab. 8.3 Frequency ranges of EPR spectrometers and the corresponding wavelengths and magnetic fields.
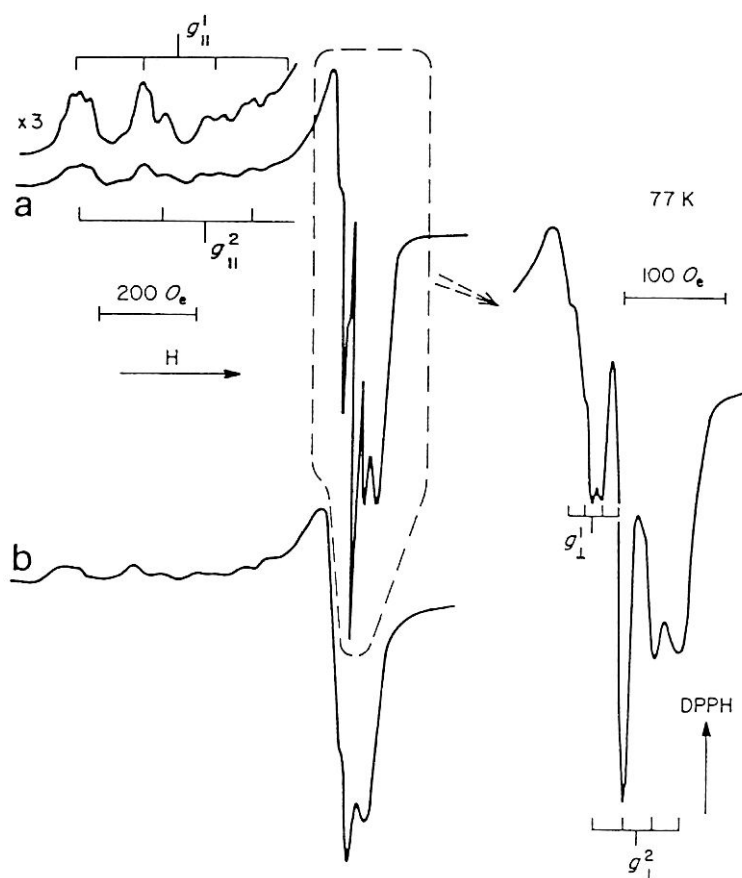
Band	λ	ν	$B_0(g=2)$
X	3 cm	9,5 GHz	0,35 T
K	12 mm	24 GHz	0,86 T
Q	8 mm	35 GHz	1,25 T
V	4 mm	70 GHz	2,5 T

Fig. 8.15 Set up of an EPR resonator equipped with glass-fiber optics suitable for UV/Vis and Raman spectroscopy.

Fig. 8.16 EPR signals of DPPH and $(FA)_2(PF)_6$ at 300 K.
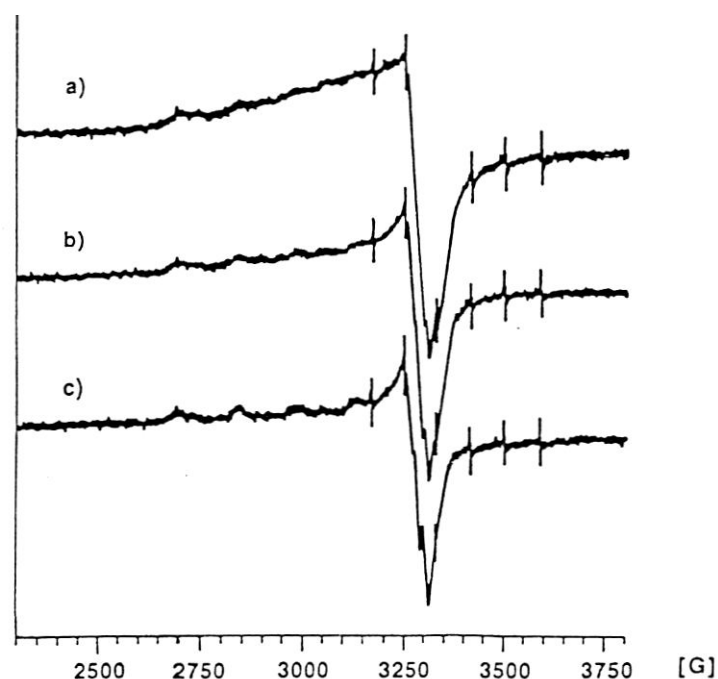

Fig. 8.17 EPR spectra of Cu,H-ZSM-5 zeolite recorded at 77 K after treatment in O_2 at 673 K and evacuation at 293 K (a) and in pure O_2 (b).

Tab. 8.4 Summary of the parameters of EPR signals due to Cu^{2+} ions in different mordenites and ZSM-5 zeolites.

| Sample	Calcination temperature (°C)	$g_{\parallel}$	$g_{\perp}$	$A_{\parallel}$ (Oe)	$A_{\perp}$ (Oe)
8CuHM	520 and 800	2.32	2.05	142	18.0
51CuHM	520	2.32	–	142	–
15CuNaM	520	2.32		140	
		2.28		168	
CuH-ZSM–5 and	520	2.33	2.07	142	17.5
CuNa-ZSM–5		2.27	2.045	172	29.0
CuH-ZSM–5	800	2.31	2.06	153	
		2.29	2.05	156	23.0
CuNH₄-ZSM–5	uncalcined	2.37	2.09	132	–
CuNH₄-ZSM–5	100	2.33	2.065	141	–
H-ZSM–5+Cu-hydroxycarbonate	800	2.31	2.06	153	
		2.29	2.05	156	23.0

Fig. 8.18 EPR spectra of Cu,H-ZSM-5 zeolite recorded after treatment with 5% O_2 in He (a) and 5% CH_4 in He for 3 minutes (b) and 30 minutes (c) at 773 K.
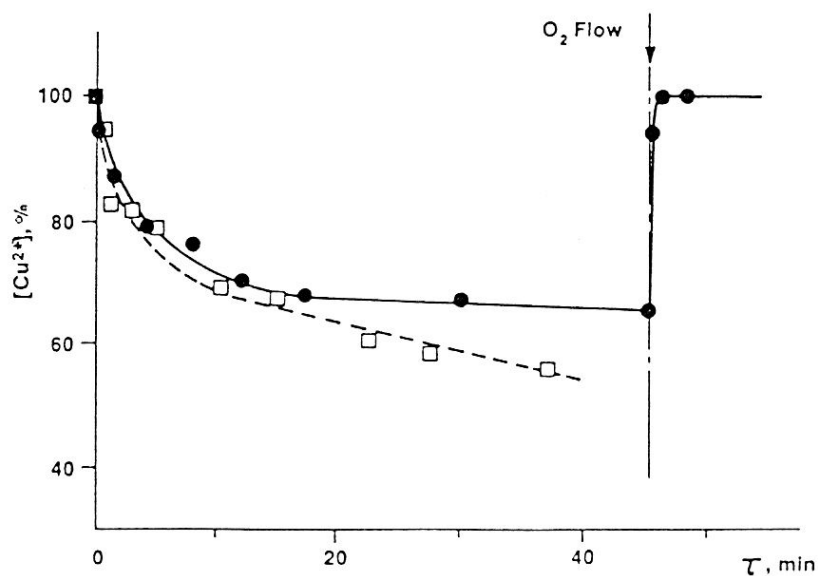
Fig. 8.19 Change of the integral intensity of the EPR signals of Cu^{2+} ions in Cu,H-ZSM-5 zeolite recorded during treatment with 5% CH_4 in He at 773 K (left) and upon switching to 3% O_2 in He (right). The dotted curve was obtained for non-purified helium.
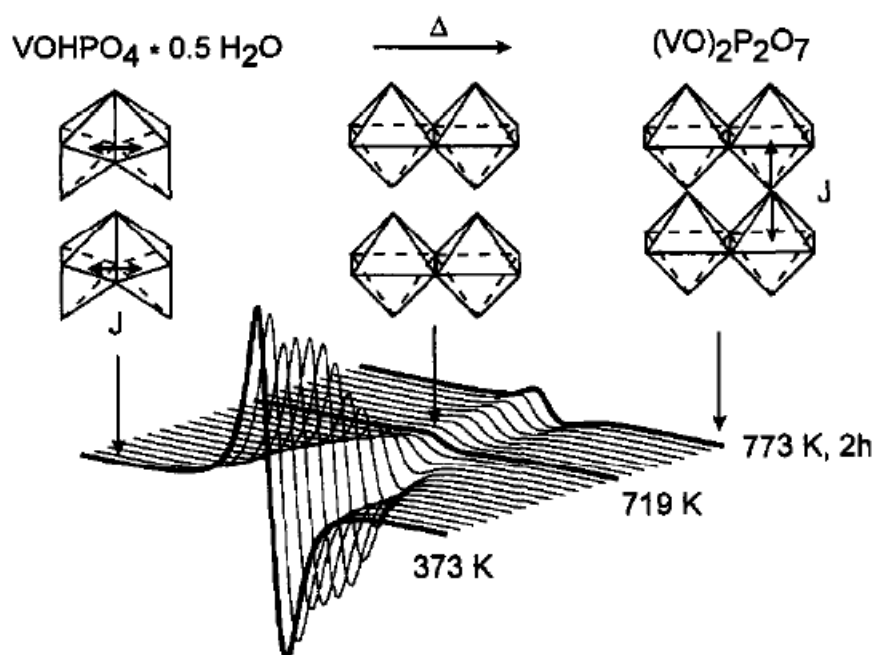

Fig. 8.20 In situ EPR spectra recorded during dehydration of $VOHPO_4 \cdot 0.5\ H_2O$ to $(VO)_2P_2O_7$.
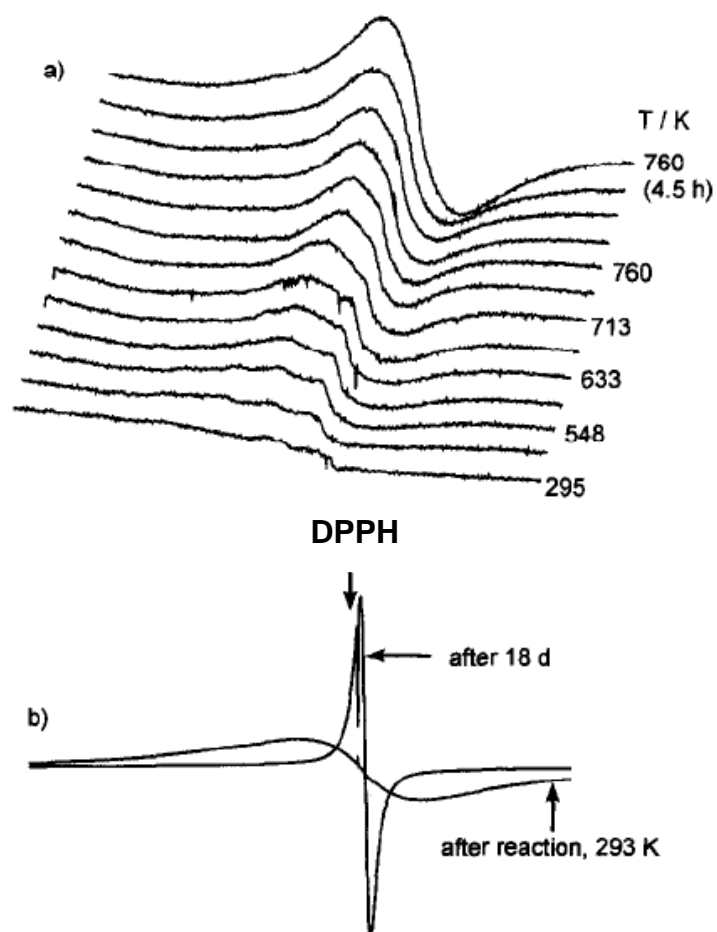
Fig. 8.21 Development of the EPR signal of V^{4+} species of a VPO catalyst during the selective oxidation of *n*-butane to maleic anhydride (a). In (b), the EPR spectrum obtained immediately after the reaction is compared with the spectrum recorded 18 days later.
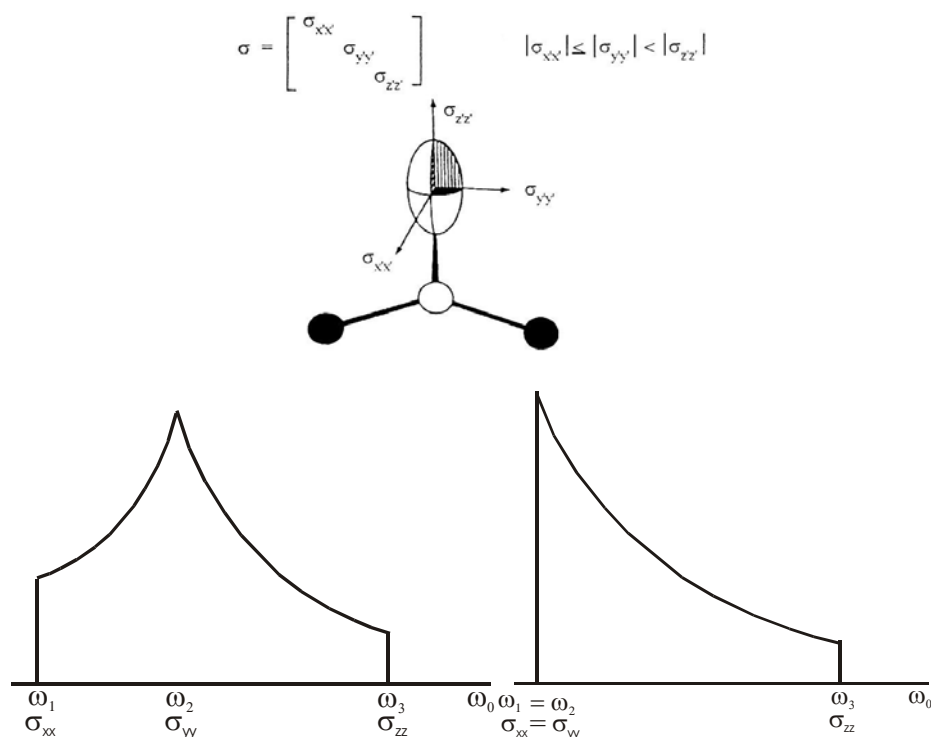
9. Solid-state NMR spectroscopy
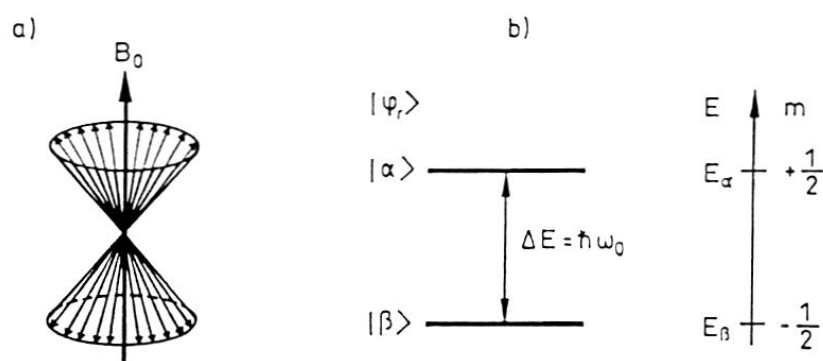
Fig. 9.1 Nutation of nuclear dipoles in an external magnetic B_0 field (a) and the corresponding energy levels (b).
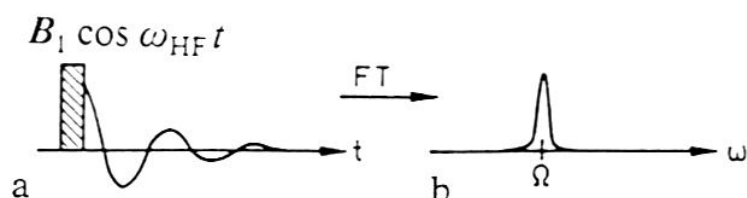

Fig. 9.2 Principle of nuclear spin excitation of by short radio-frequency pulses (a) and Fourier transform NMR spectroscopy (b).


Fig. 9.3 Scheme of the anisotropic shielding of nuclei by electrons (top) and the corresponding effects on the NMR line shape for the general case (bottom, left) and axial symmetry (bottom, right).
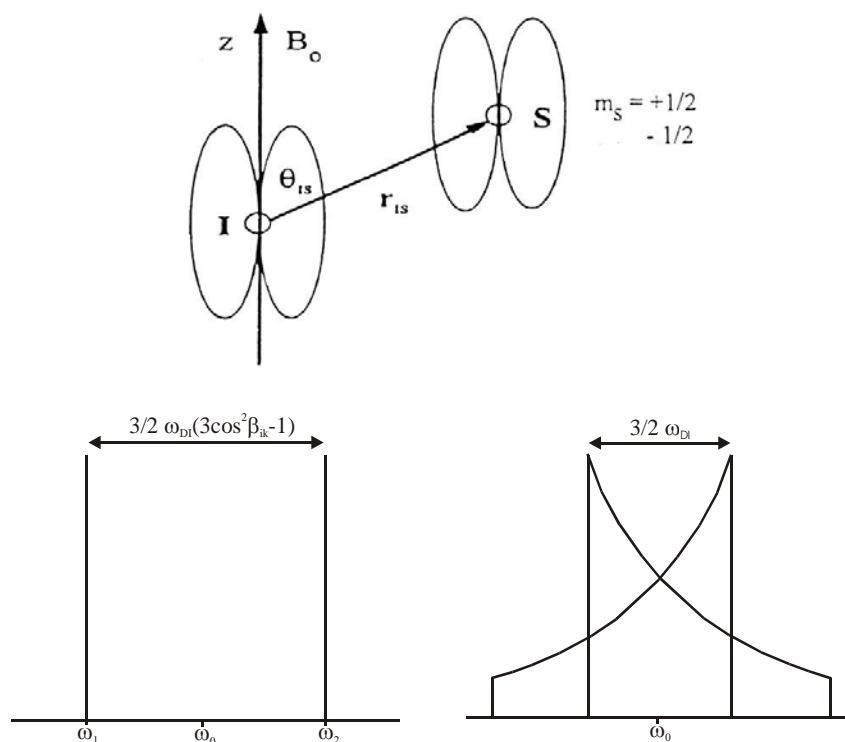
Fig. 9.4 Scheme of the dipolar interaction of neighbouring nuclear dipole moments (top) and the corresponding effects on the NMR line shape for a single crystal (bottom, left) and a powder sample (bottom, right).
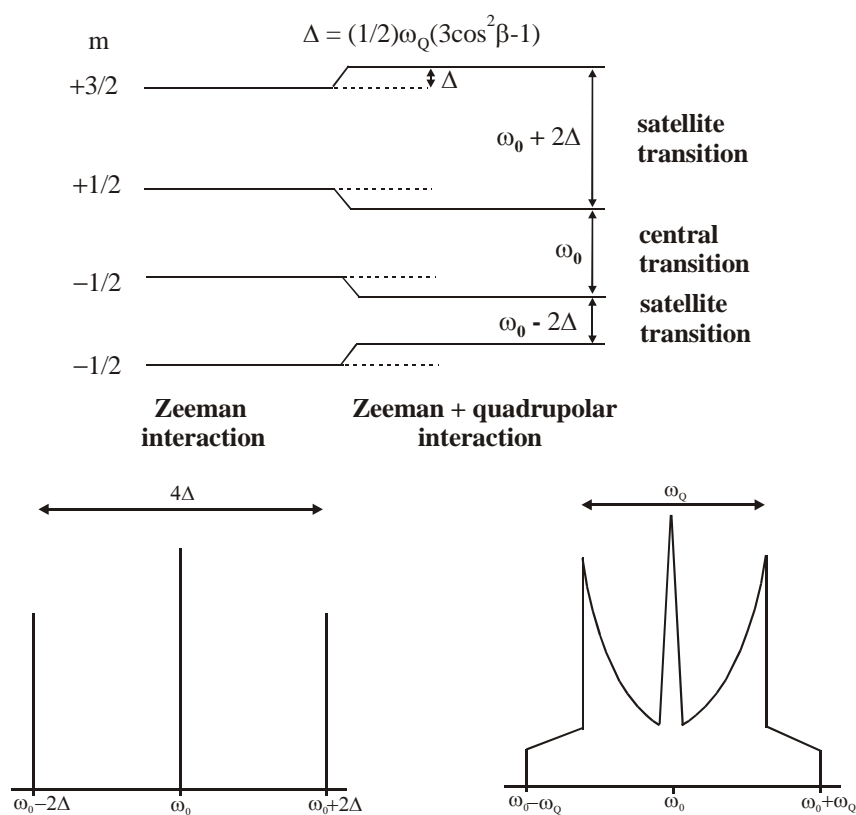

Fig. 9.5 Energy levels of nuclei with spin $I = 3/2$ demonstrating the effect of the quadrupolar interaction (top) and resulting NMR line shapes of a single crystal (bottom, left) and a powder sample (bottom, right)
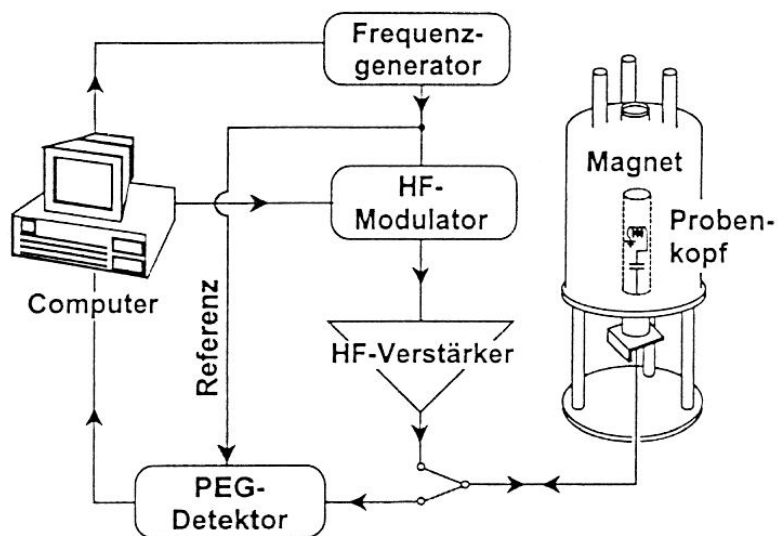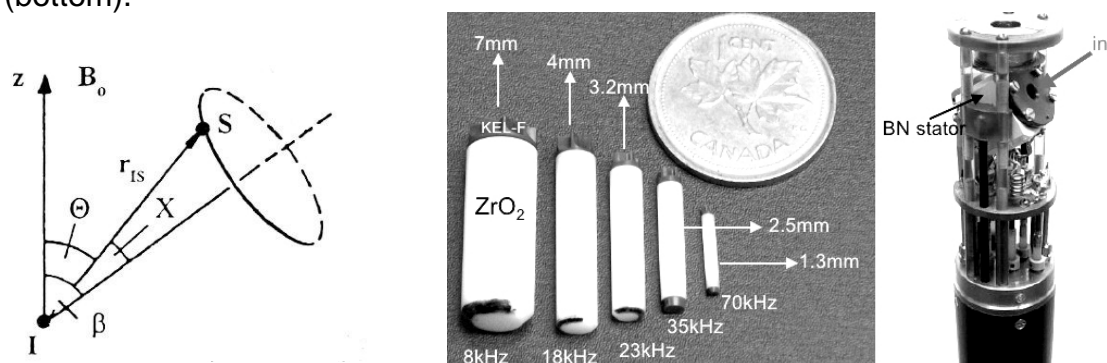
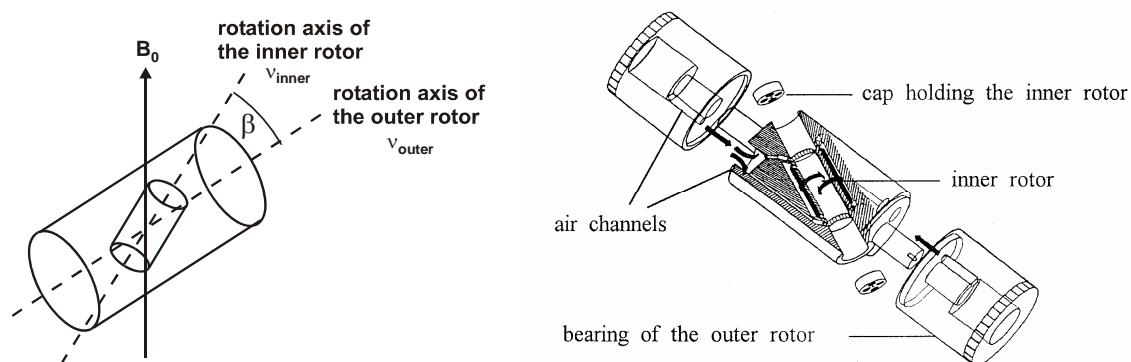**Fig. 9.6** Scheme of a Fourier transformation NMR spectrometer.
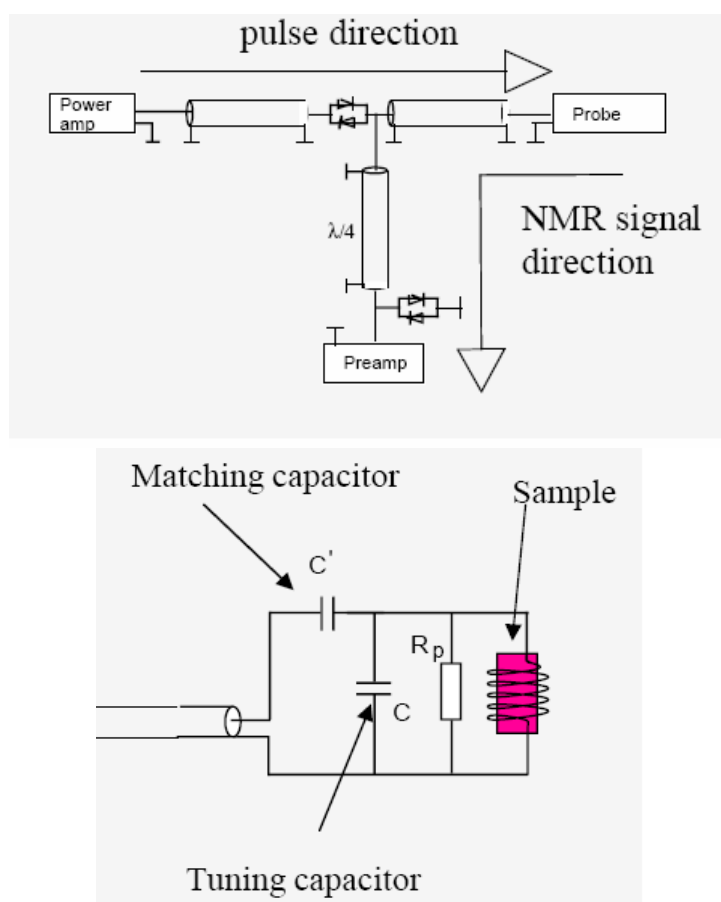
Fig. 9.7 Signal ways to the probe and the preamplifier (top) and scheme of a single resonance NMR probe (bottom).
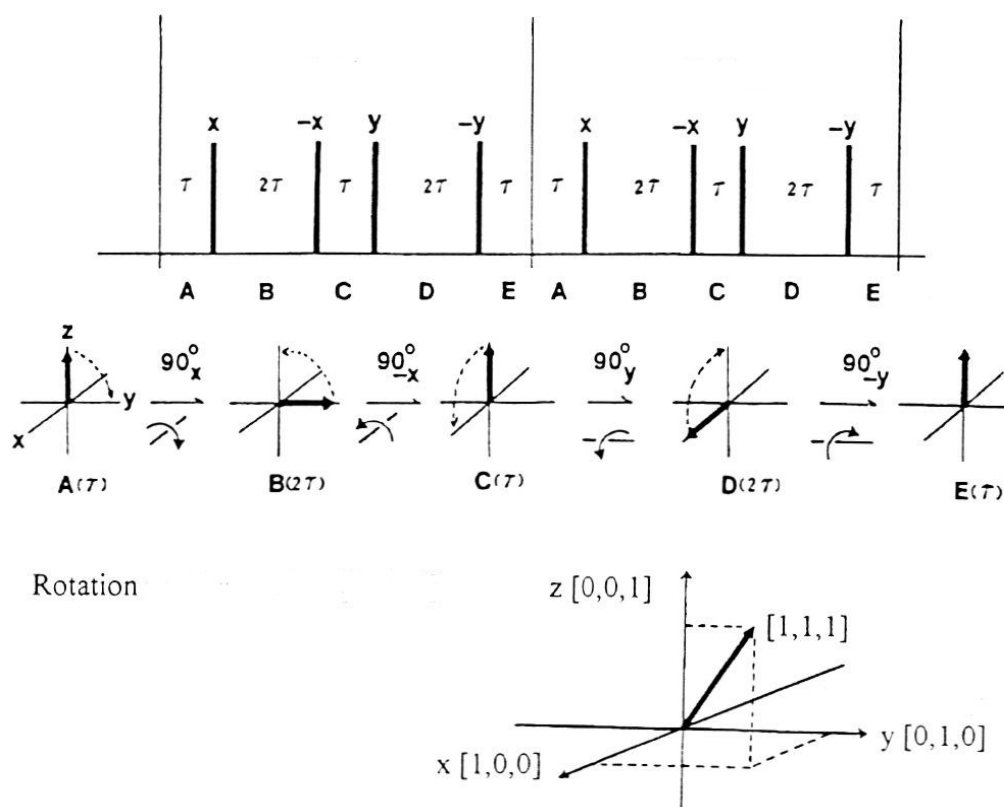
Fig. 9.8 Scheme of the multiple-pulse sequence WHH-4 (top) and the effect on the spin system (bottom).
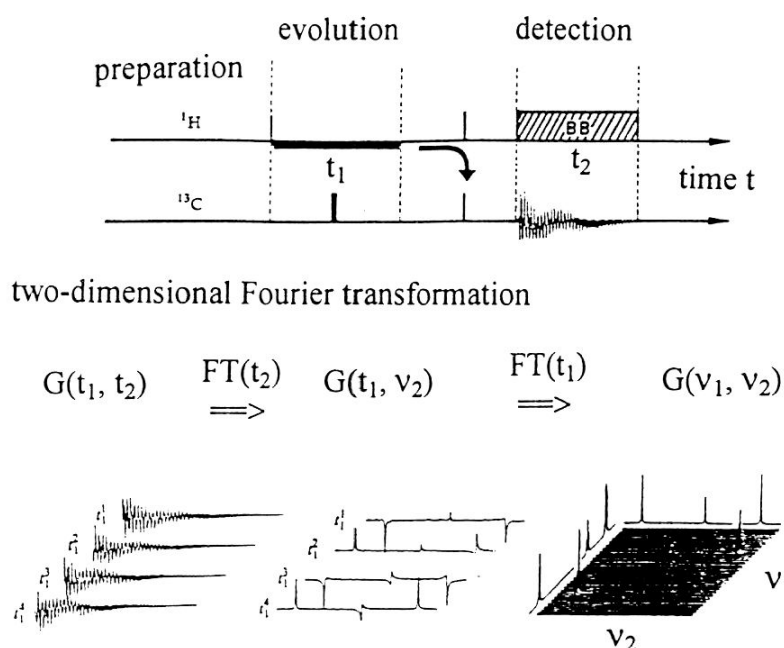

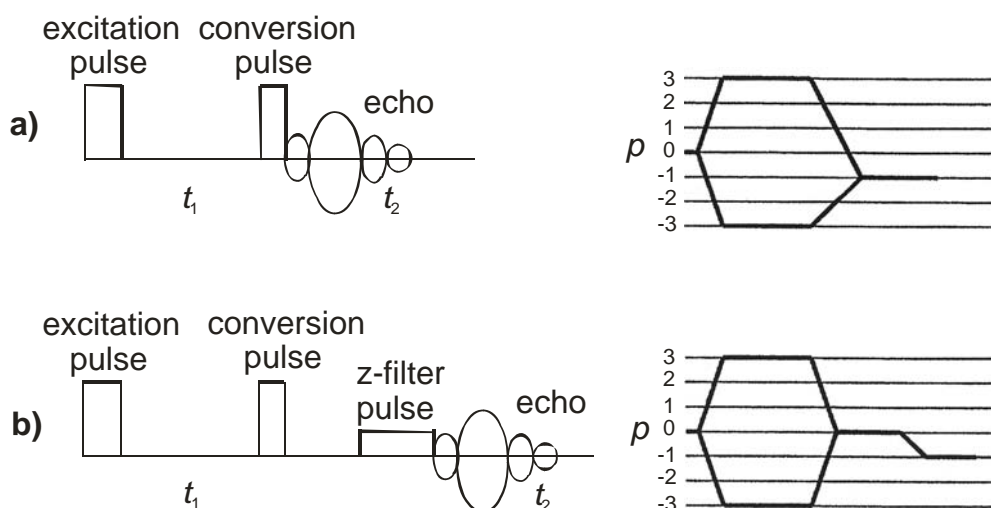**Fig. 9.9** Principle of the magic angle spinning (MAS) technique.

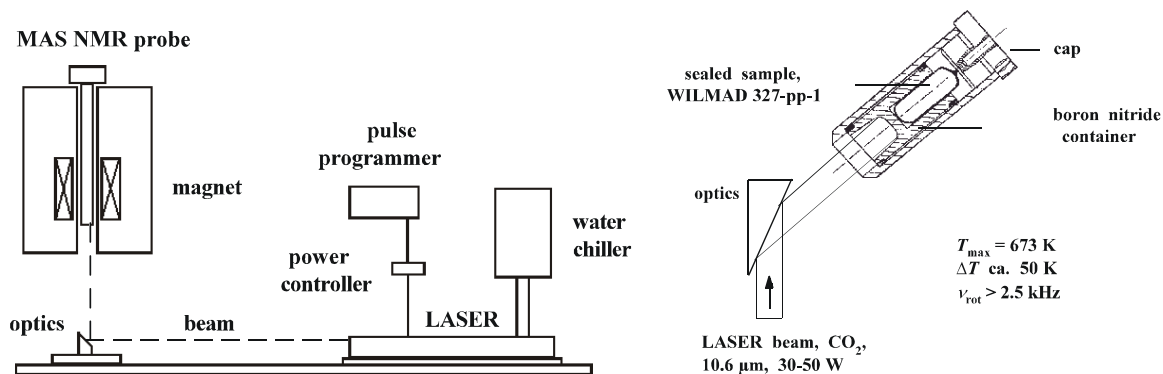**Fig. 9.10** Principle of double oriented rotation (DOR) and scheme of a DOR rotor.

Fig. 9.11 Principle of two-dimensional NMR experiments with twofold Fourier transformation.

Fig. 9.12 Sequences (left) of two- (a) and three-pulse (b) multiquantum (MQ) NMR experiments and the corresponding coherence transfer pathways (right).

Fig. 9.13 Scheme of a high-temperature MAS NMR probe with Laser heating system.
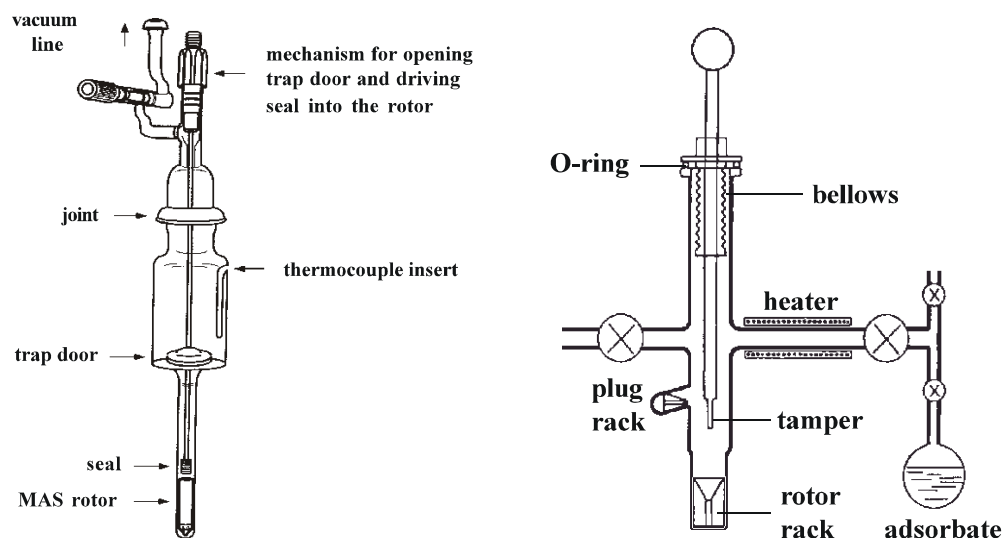
Fig. 9.14 Equipment utilized for the preparation of catalysts in vacuum (left) and under flow conditions (right).
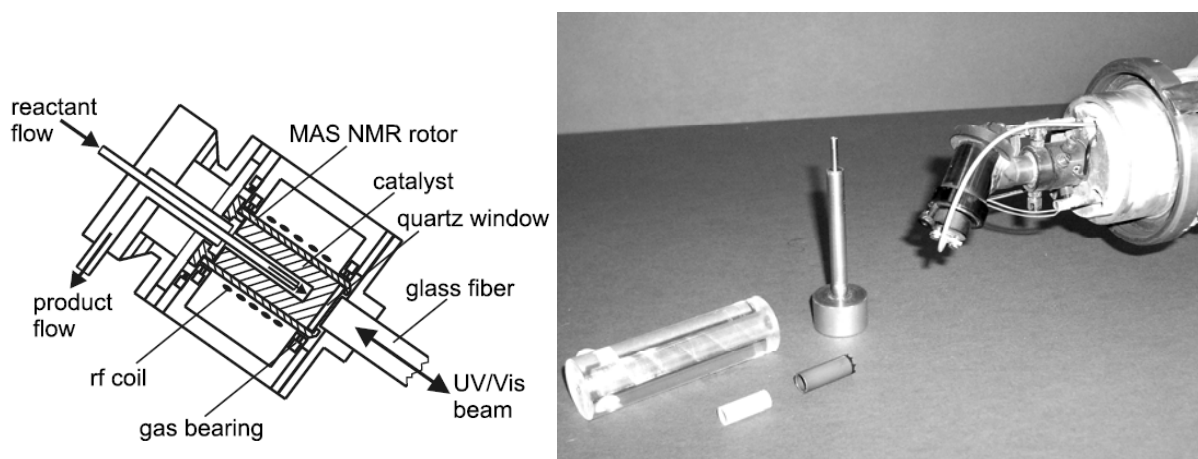
Fig. 9.15 MAS NMR turbine equipped with a gas injection system and a glass-fiber for simultaneous UV/Vis studies.

Fig. 9.16 Combination of in situ MAS NMR and UV/Vis spectroscopy.

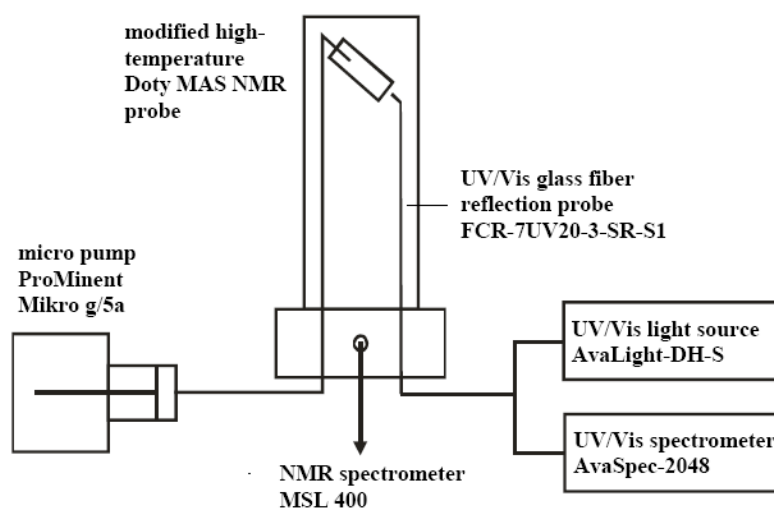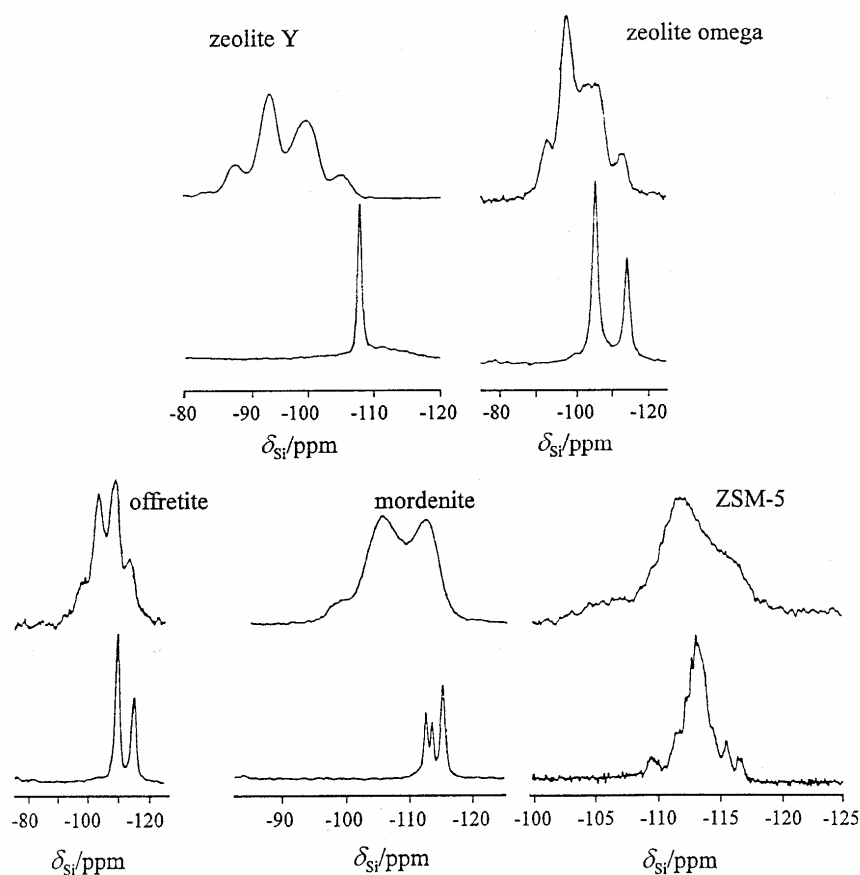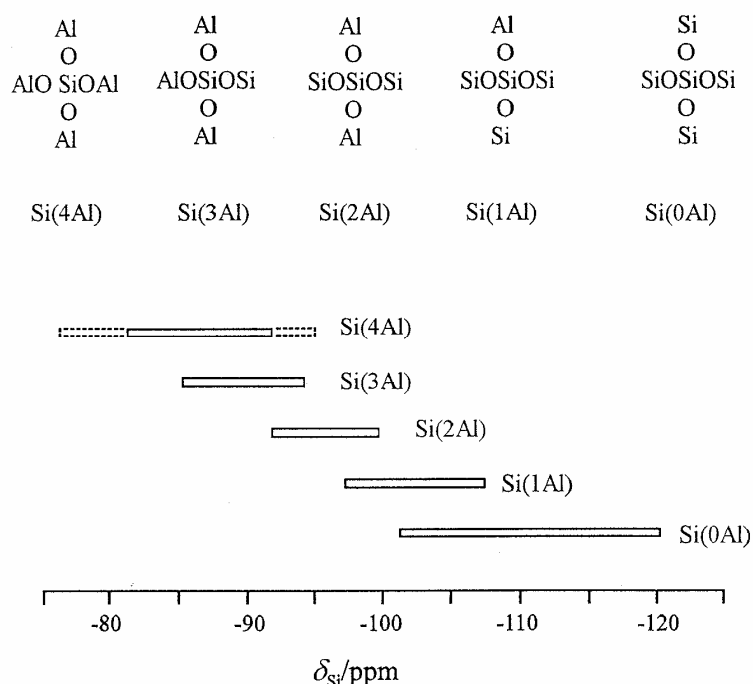**Fig. 9.17** ^{29}Si MAS NMR spectra of zeolites with (top) and without (bottom) aluminum atoms at T positions.

Tab. 9.1 Examples for ^{29}Si chemical shifts of Si(nAl) units in zeolites.

Zeolite	n_{Si}/n_{Al}	Site	Si(4Al)	Si(3Al)	Si(2Al)	Si(1Al)	Si(0Al)
Y	2.5	T	-83.8	-89.2	-94.5	-100.0	-105.5
	∞	T					-107.8
Omega	3.1	T1		-89.1	-93.7	-98.8	-103.4
		T2	-89.1	-93.7	-98.8	-107.0	-112.0
	∞	T1					-106.0
		T2					-114.4
mordenite	5.0	T1 to				-100.1	-105.7	-112.1
		T4					
	∞	T1					-112.2
		T4					-113.1
		T2 + T3					-115.0
ZSM-5	20	T1 to				-106.0	-112.0
		T12					

|				
Al	Al	Al	Al	Si
O	O	O	O	O
AlO SiOAl	AlOSiOSi	SiOSiOSi	SiOSiOSi	SiOSiOSi
O	O	O	O	O
Al	Al	Al	Si	Si
Si(4Al)	Si(3Al)	Si(2Al)	Si(1Al)	Si(0Al)

Fig. 9.18 Dependence of the ^{29}Si NMR chemical shifts of tetrahedrally coordinated framework silicon atoms on the aluminum occupation of neighbouring T sites.
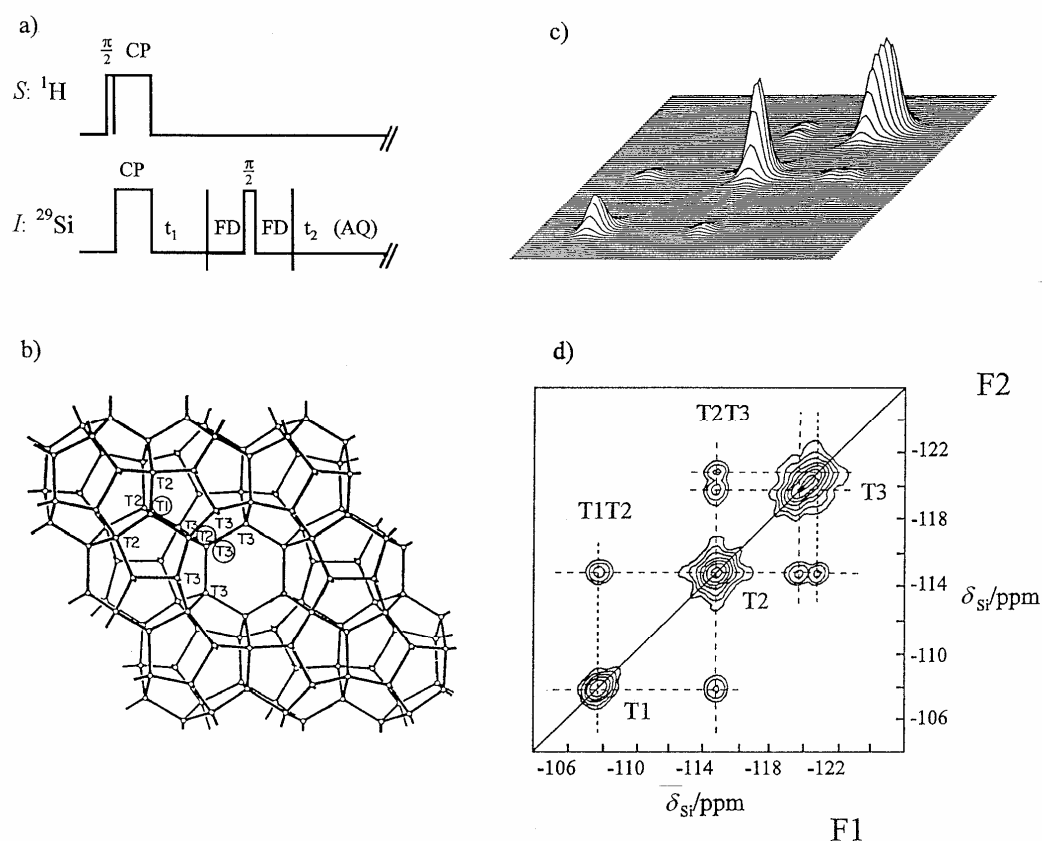

Fig. 9.19 Connectivities of silicon atoms in zeolite ZSM-39 studied by sampling the J-coupling (ca. 110 Hz) with the two-dimensional ^{29}Si COSY MAS NMR experiment: a) pulse sequence (parameter FD is a fixed delay of 5 ms), b) zeolite structure with T sites, c) 2D COSY MAS NMR spectrum (stacked plot), and d) 2D COSY MAS NMR spectrum (contour plot).
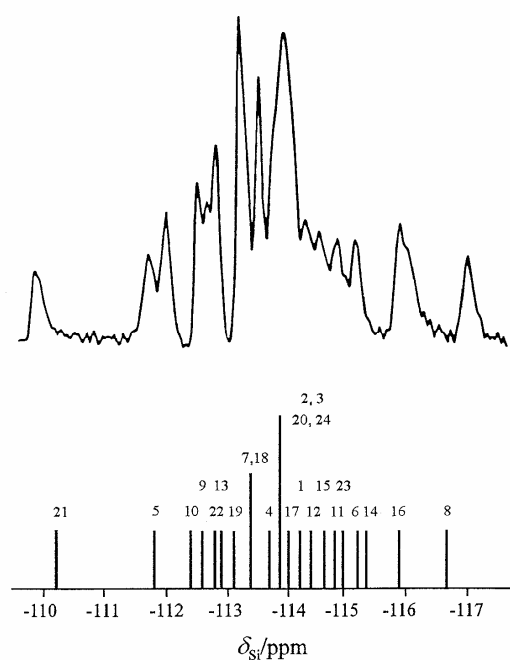
**Fig. 9.20** Experimental (top) and calculated (bottom) ^{29}Si MAS NMR spectrum of siliceous zeolite ZSM-5 with 24 different T sites.
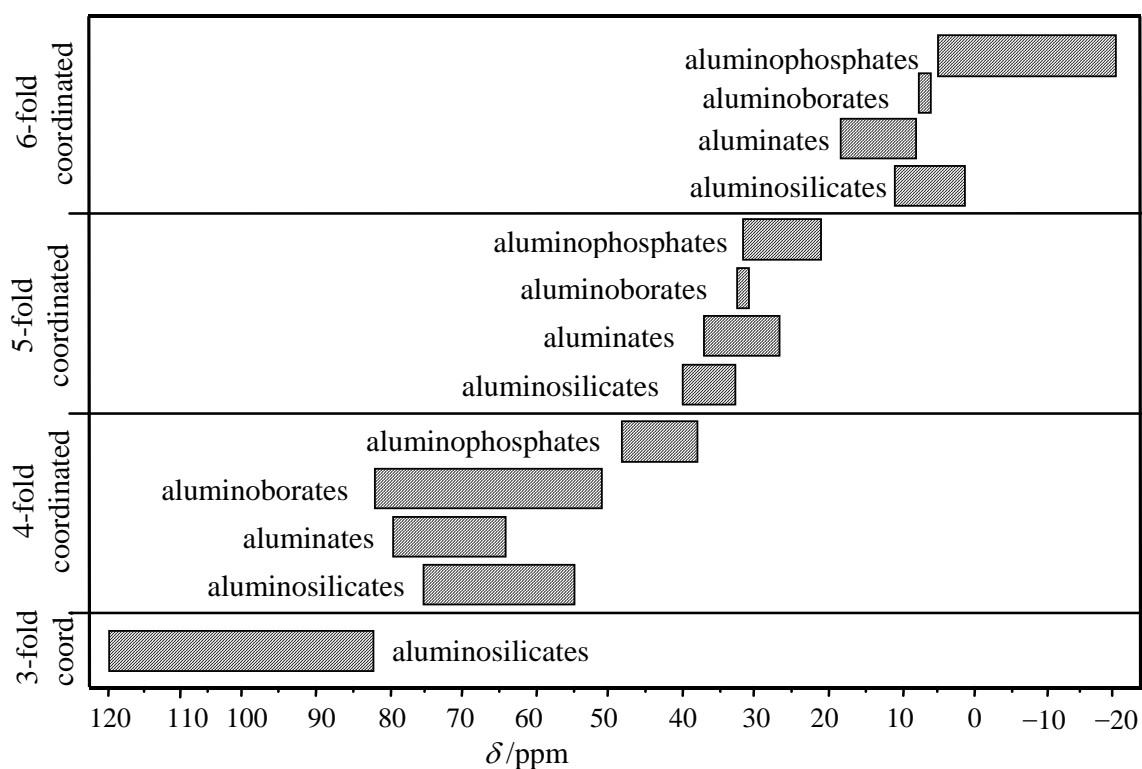

Fig. 9.21 Dependence of the ^{27}Al NMR chemical shifts of aluminum atoms on their oxygen coordination.
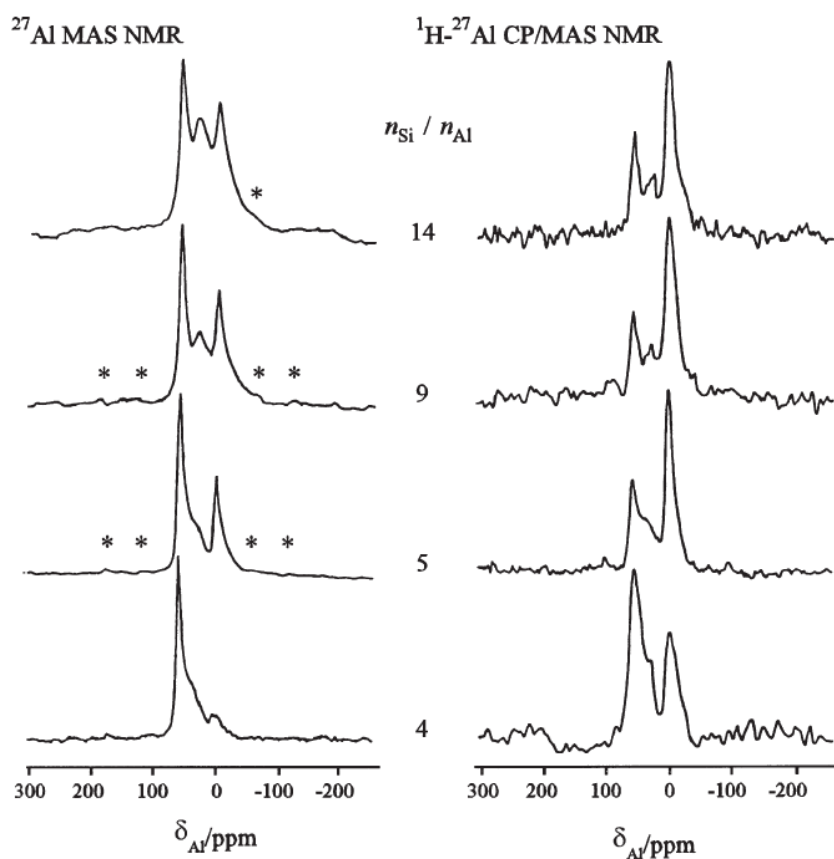
Fig. 9.22 ^{27}Al MAS NMR spectra of hydrated zeolites H-Y with different framework aluminum contents (n_{Si}/n_{Al} ratios) recorded via direct excitation (left) and by cross polarization (right).
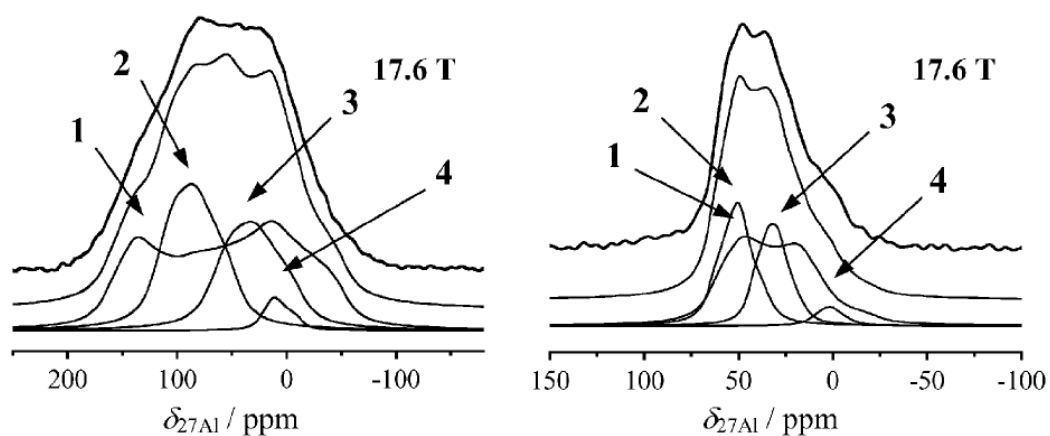
Fig. 9.23 ^{27}Al NMR spectra of dealuminated zeolites H-Y in the dehydrated state, recorded without (left) and with (right) application of MAS.
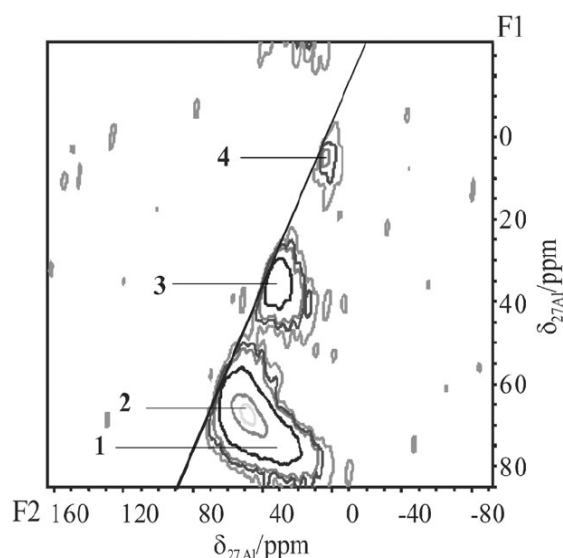
Fig. 9.24 ^{27}Al MQMAS NMR spectra of dealuminated zeolites H-Y in the dehydrated state with signal assignments according to Figure 9.23.
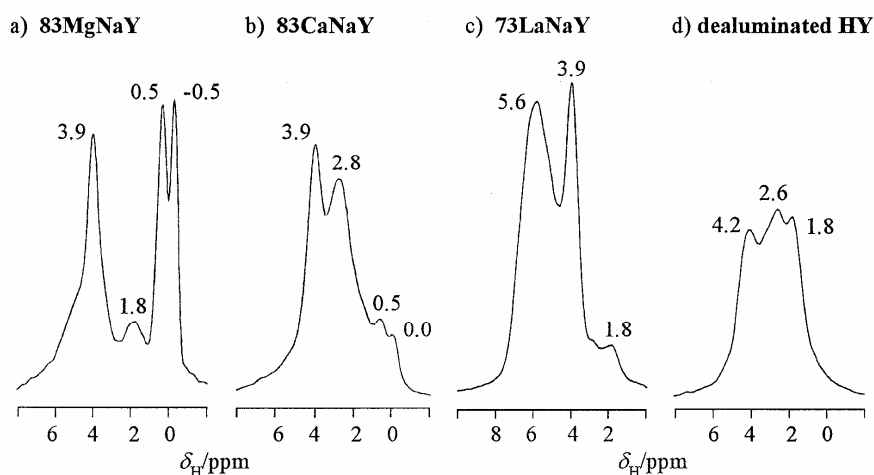

Fig. 9.25 ^{1}H MAS NMR spectra of hydroxyl groups in zeolites Y exchanged with different multivalent cations (a-c) and after dealumination (d).

Tab. 9.2 Assignments of ^{1}H MAS NMR signals of surface OH groups.

| ^{1}H NMR shift, δ_{1H} /ppm	Abbreviation	Type of hydroxyl group
−0.5 to 0.5	MeOH	Metal or cation OH groups in large cavities or at the outer surface of particles
1.2−2.2	SiOH	Silanol groups at the external surface or at lattice defects
2.4−3.6	AlOH	OH groups bonded to extra-framework aluminum species located in cavities or channels involved in hydrogen bonding
2.8−6.2	CaOH′, AlOH′, LaOH′	Cation OH groups located in sodalite cages of zeolite Y and in channels of ZSM-5 involved in hydrogen bonding
3.6−4.3	SiOHAl	Bridging OH groups in large cavities or channels of zeolites
4.6−5.2	SiOH′Al	Bridging OH groups in small channels and cages of zeolites
5.2−8.0	SiOH′Al	Perturbed bridging OH groups in zeolites H-ZSM-5, H-Beta and MCM-22
∼15	SiOH′	Internal SiOH groups involved in strong hydrogen bonding
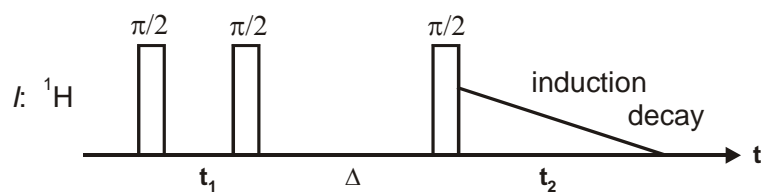
Fig. 9.26 Scheme of a two-dimensional spin-exchange experiment for studying the dipolar coupling between hydroxyl protons.

a) **SAPO-5**
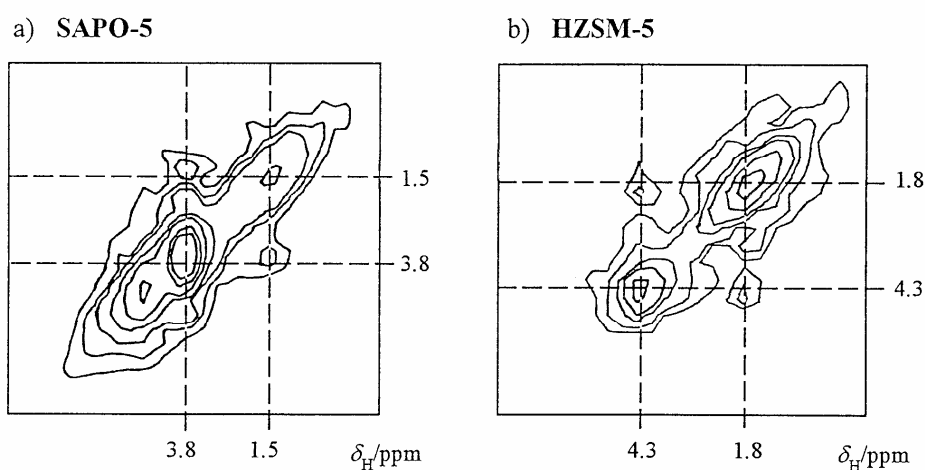
b) **HZSM-5**

Fig. 9.27 2D ^{1}H spin-exchange MAS NMR spectra of the dehydrated silicoaluminophosphate SAPO-34 (a) and zeolite H-ZSM-5 (b).
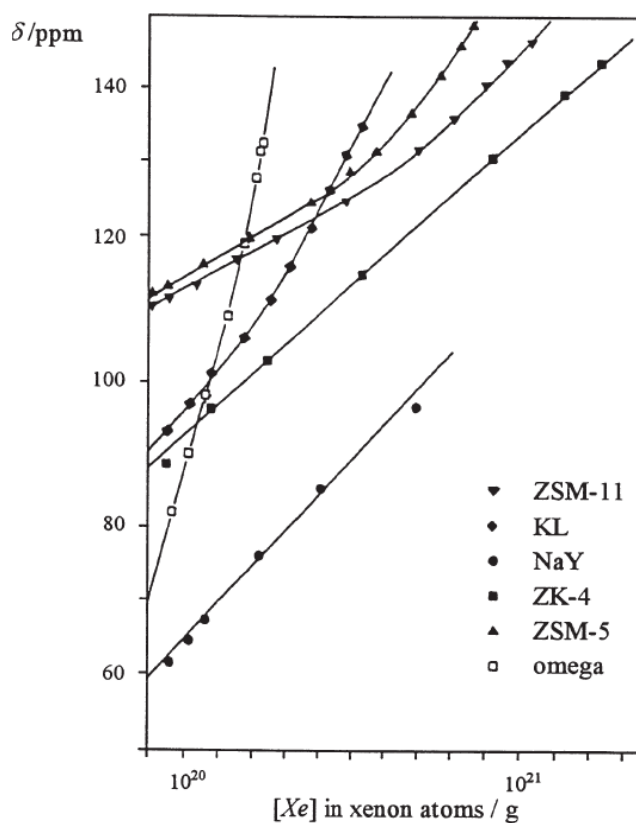
Fig. 9.28 ^{129}Xe NMR chemical shifts of xenon adsorbed on different zeolites.

Tab. 9.3 Survey on the [129]Xe NMR chemical shifts of xenon adsorbed on different zeolites and extrapolated to the gas pressure of $p = 0$.

| Zeolites	δ_S/ppm	Cages and pore sizes
X and Y	60	Spherical supercages with $\varnothing \approx 1.3$ nm
Omega	73	Unidimensional 12-ring pores with openings of 0.74 nm
A and ZK4	87	Spherical cages with $\varnothing \approx 1.14$ nm, six 8-ring openings with $\varnothing \approx 0.4$–0.5 nm
L	90	Unidimensional 12-ring pores with openings of $\varnothing \approx 0.71$ nm, maximum $\varnothing \approx 0.9$ nm
ZSM-11	110	Three-dimensionally interconnecting 10-ring pores, 0.51×0.55 nm
Ferrierite	110	Pseudo-spherical cages with $\varnothing \approx 0.7$ nm, two 8-ring openings, 0.34×0.48 nm
	165	Bidimensionally interconnecting 10-ring pores, 0.43×0.55 nm
ZSM-5	113	Three-dimensionally interconnecting 10-ring pores, 0.51×0.55 nm and 0.54×0.56 nm
Rho	114	Three-dimensionally interconnecting pores forming spherical cages with $\varnothing \approx 1.0$ nm
	230	Prisms, 8-ring, 0.39×0.51 nm
Mordenite	115	Unidimensional 12-ring pores, 0.67×0.70 nm
	250	8-ring side-pockets, 0.29×0.57 nm
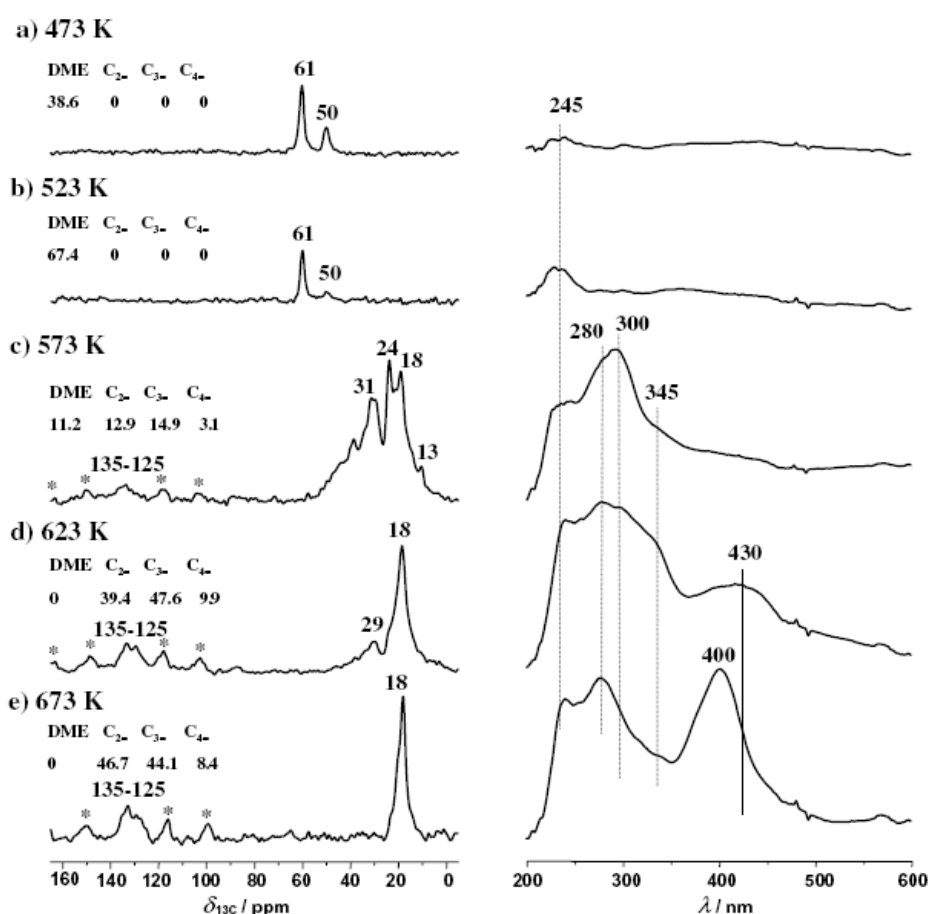
Fig. 9.29 ^{13}C MAS NMR (left) and UV/Vis spectra (right) recorded during conversion of methanol on SAPO-34 at 473 to 673 K (a to e).
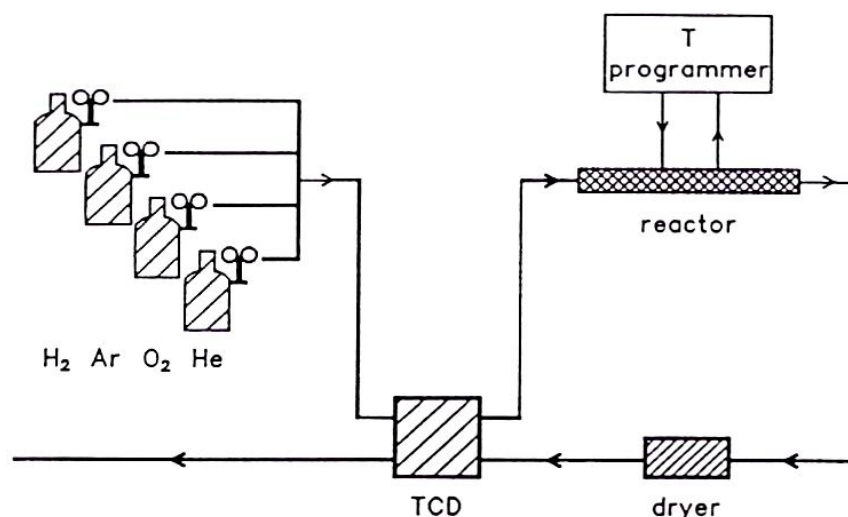
10. Thermal surface characterization methods

**Tab. 10.1** Phases occurring after reduction of metal oxides in hydrogen at 673 K.

| Metal	Oxide	$(p(H_2O)/p(H_2))_{eq}$
Cr	Cr_2O_3	$3\cdot10^{9}$
Mn	MnO_2	10
	MnO	$2\cdot10^{-10}$
Fe	Fe_2O_3	0.7
	FeO	0.1
Co	CoO	50
Ni	NiO	500
Cu	CuO	$2\cdot10^{8}$
	Cu_2O	$2\cdot10^{6}$
Mo	MoO_3	40
	MoO_2	0.02
Ru	RuO_2	10^{12}
Rh	RhO	10^{13}
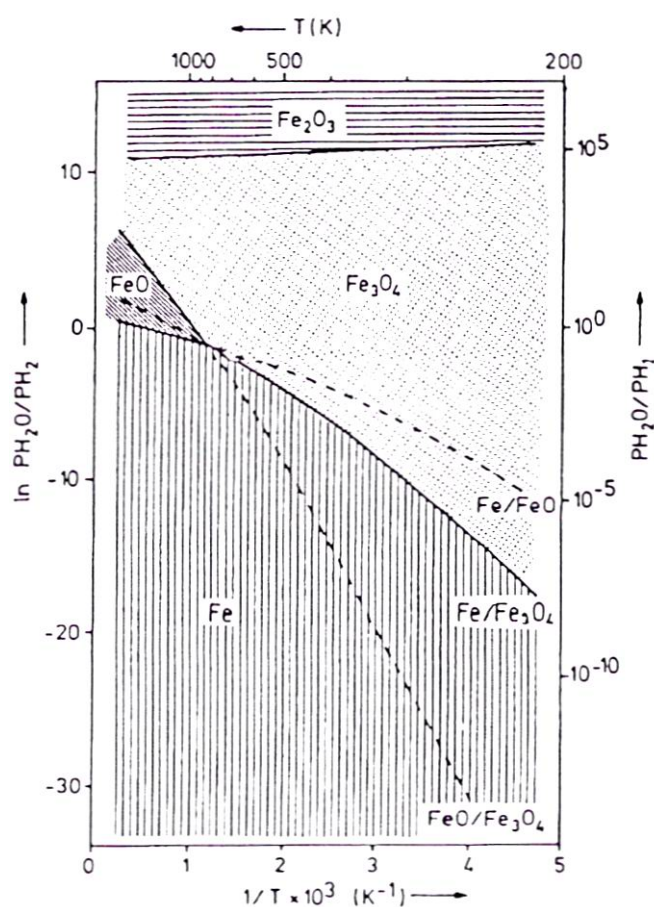
Fig. 10.1 Phase diagram of the iron oxide system exposed to a mixtures of H_2 and H_2O.
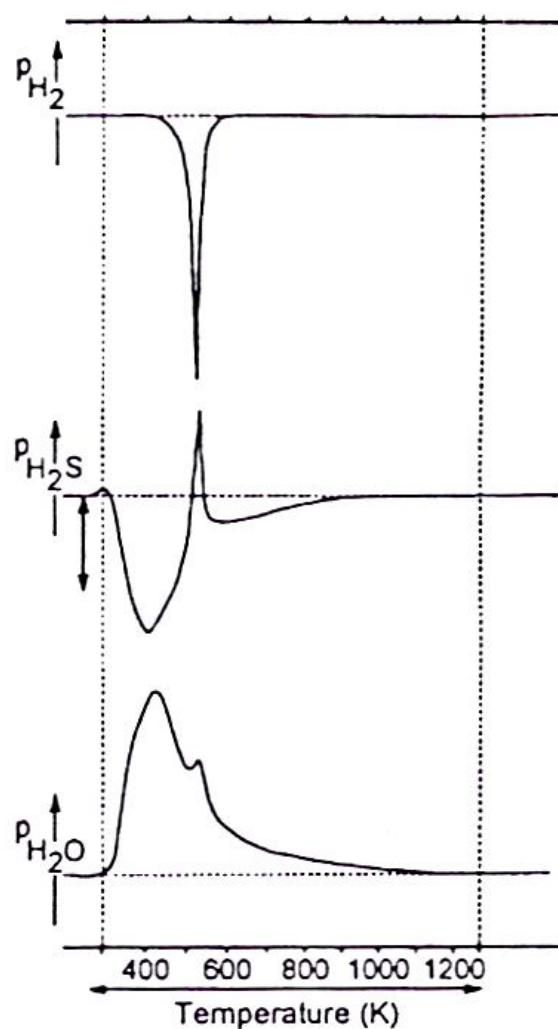
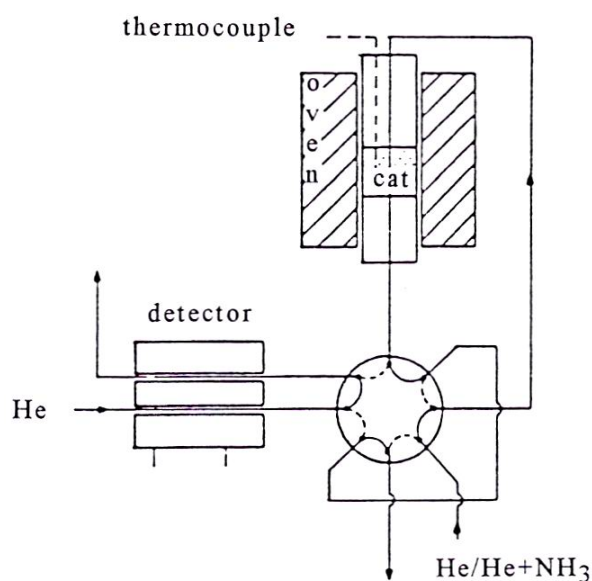**Fig. 10.2** Experimental set up for temperature-programmed reduction (TPR).
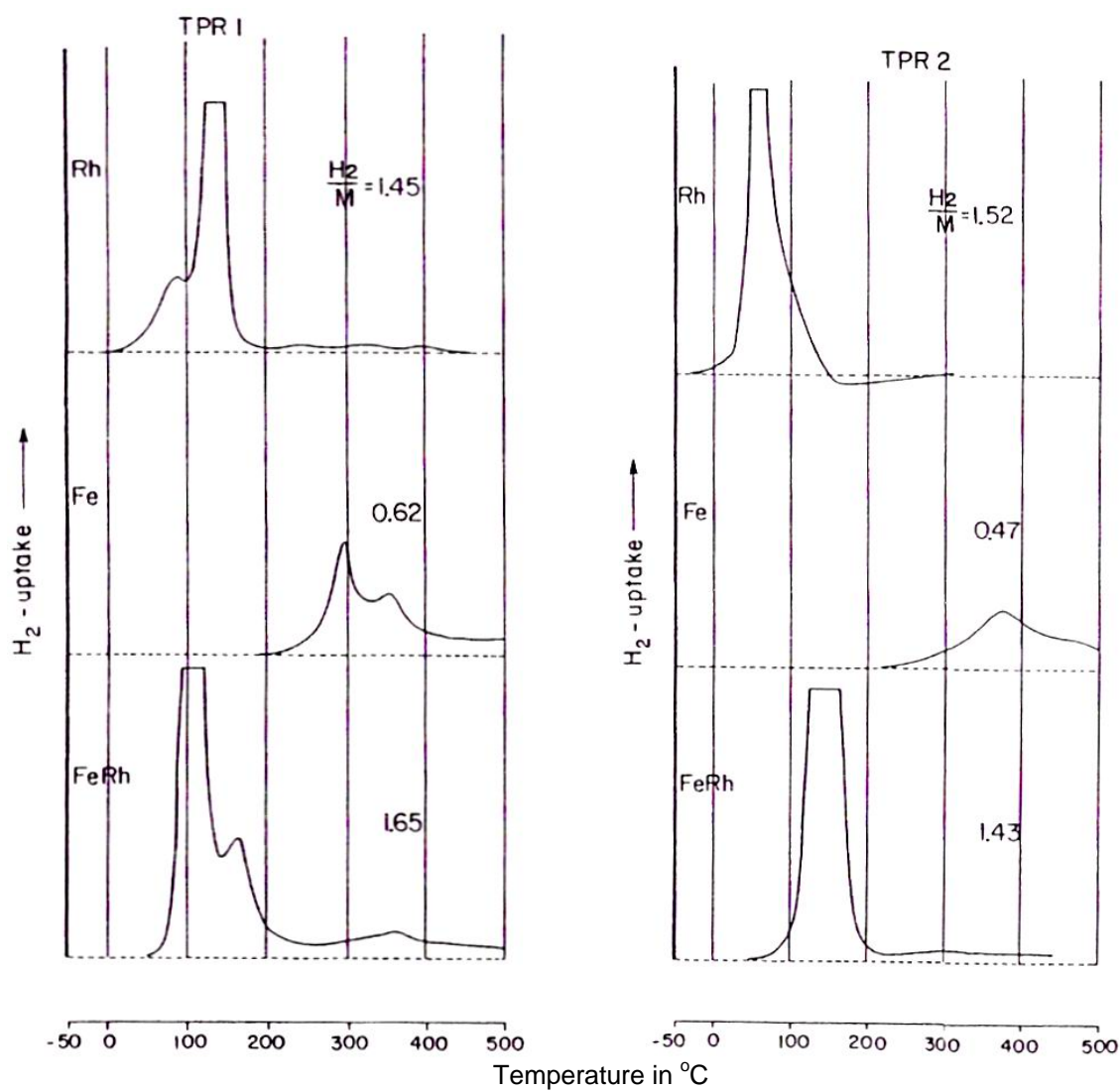
Fig. 10.3 TPR curves of silica-supported Rh, Fe, and Fe-Rh catalysts. The left curves were obtained for the freshly prepared samples, while the right curves were recorded after complete oxidation.
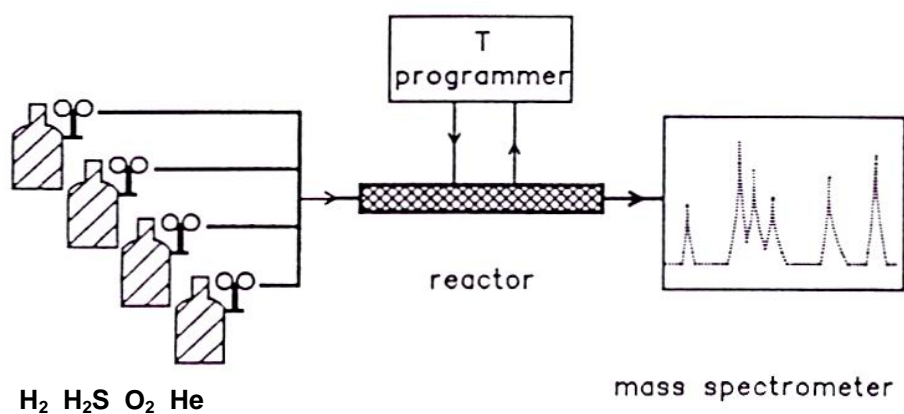
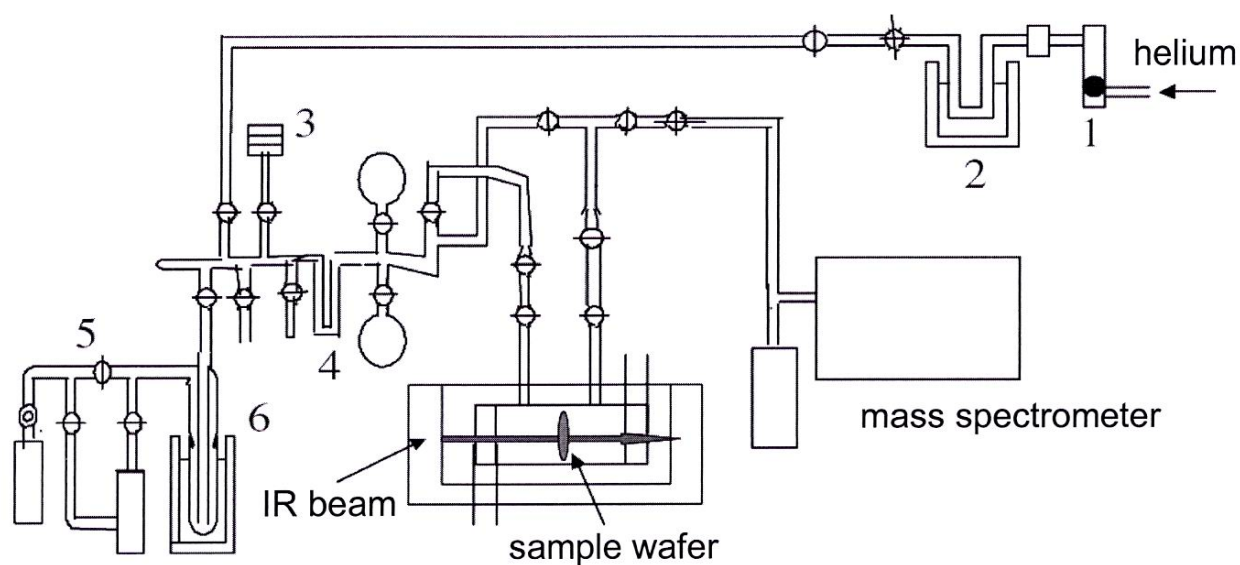**Fig. 10.4** Experimental set up for temperature-programmed sulfurization (TPS).

Fig. 10.5 TPS curves of a MoO$_3$/Al$_2$O$_3$ catalyst exposed to a mixture of H$_2$S and H$_2$ showing the consumption of these gases and the production of H$_2$O.

Fig. 10.6 Experimental set up of a temperature-programmed desorption (TPD) equipment.


Fig. 10.7 Set up for the temperature-programmed desorption of ammonia (TPDA) in combination with infrared and mass spectroscopy (IRMS) consisting of a flow meter (1), a liquid nitrogen trap with silica gel column (2), a vacuum meter (3), a sampling loop for calibration (4), a vacuum pump (5), and a liquid nitrogen trap (6).
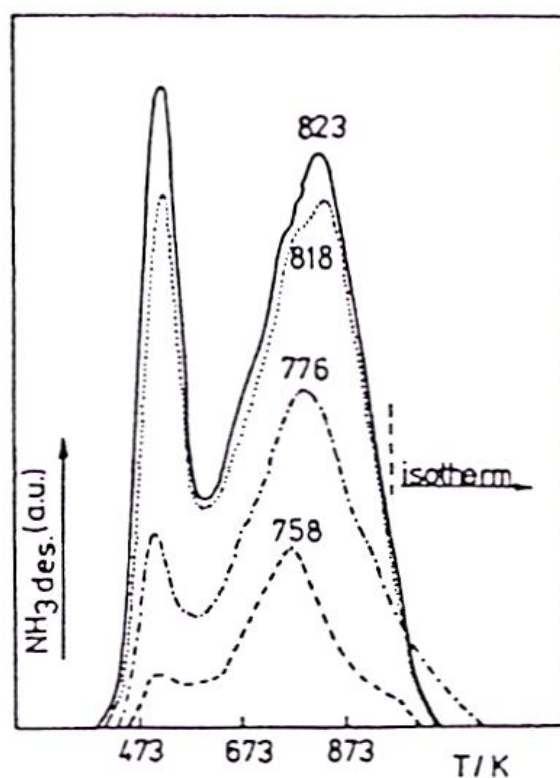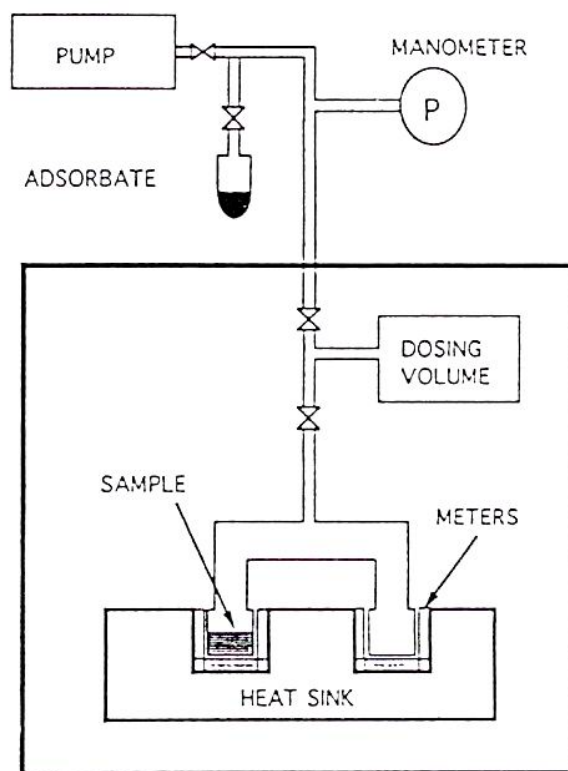
Fig. 10.8 Ammonia TPD curves of mordenites with framework n_{Si}/n_{Al} ratios of 6 to 18.
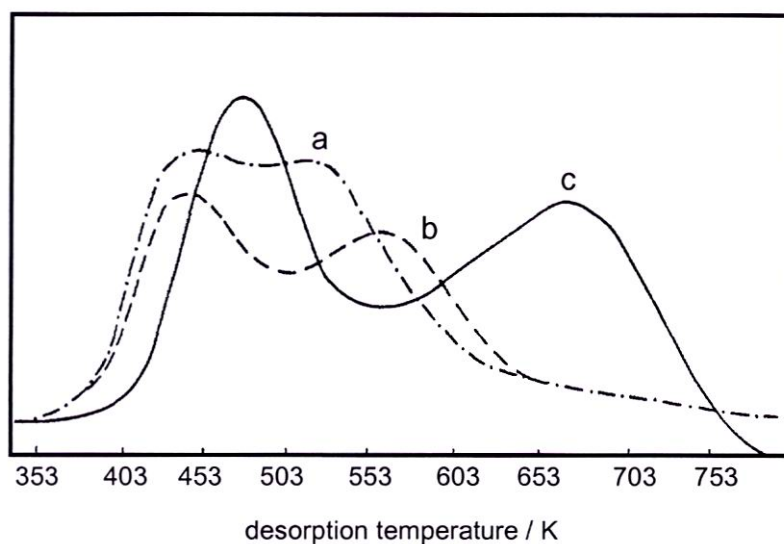
Fig. 10.9 Ammonia TPD curves of the silicoaluminophosphates H-SAPO-5 (a) and H-SAPO-11 (b) and zeolite H-ZSM-5 (c).

Fig. 10.10 Experimental set up of a Tian-Calvet type microcalorimeter with sample chamber (left) and reference chamber (right).
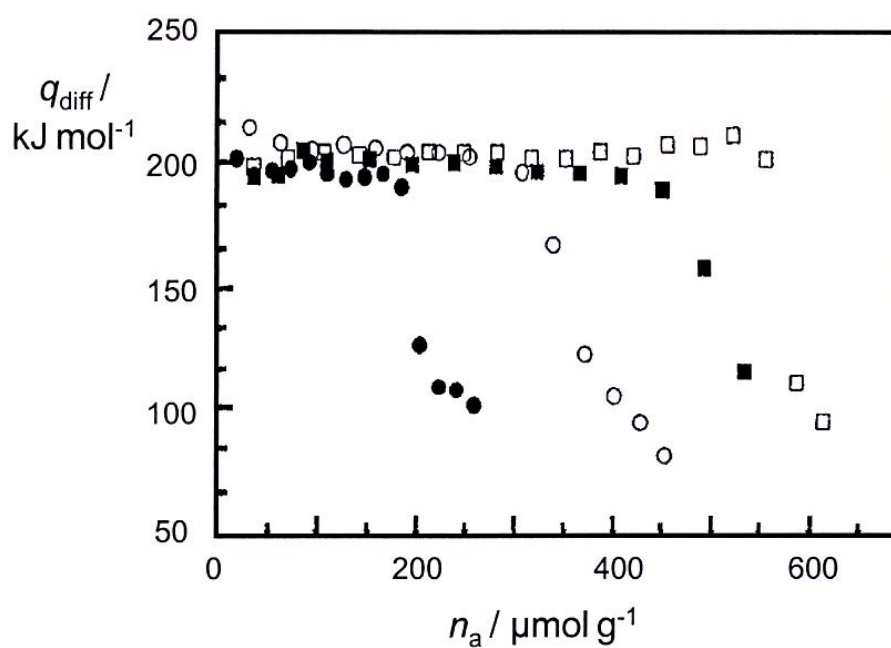
Fig. 10.11 Differential heats, q_{diff}, obtained for the adsorption of pyridine on zeolites H-ZSM-5 with aluminum contents of 180 (●), 370 (○), 530 (■), and 600 µmol/g (□).

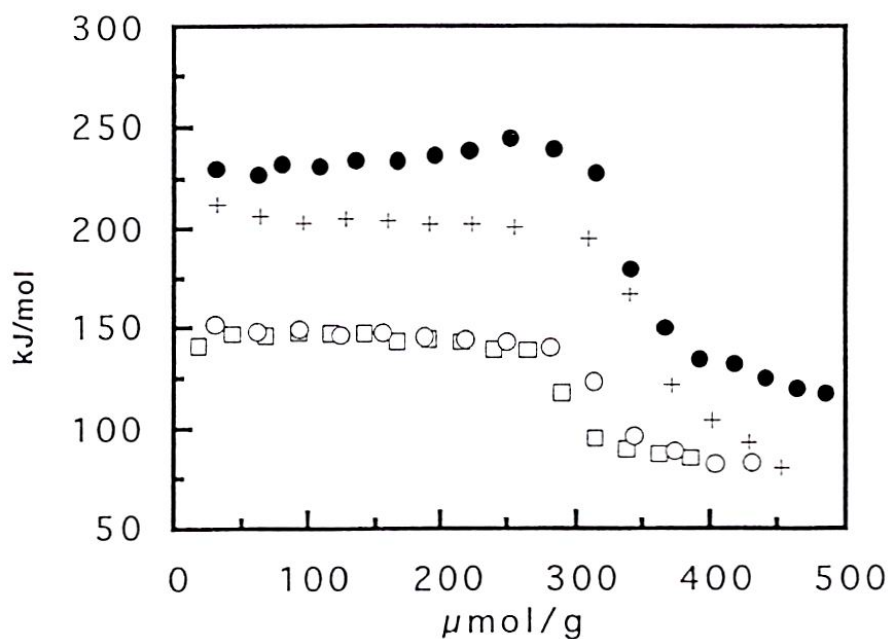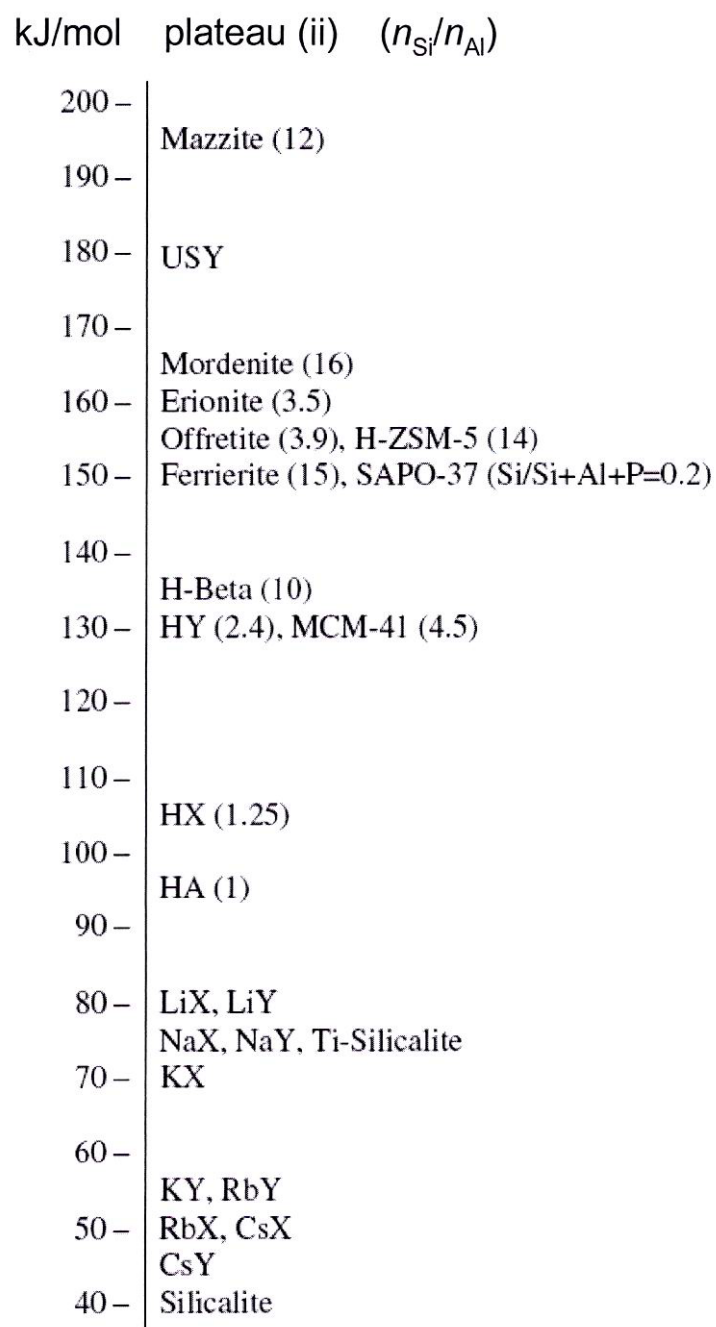**Fig. 10.12** Differential heats, q_{diff}, obtained for adsorption of ammonia ($\square$: 1.0 g zeolite, $\bigcirc$: 0.5 g zeolite), pyridine (+), and isopropylamine ($\bullet$) on zeolite H-ZSM-5 at 480 K.

Tab. 10.2 Differential heats, q_{diff}, determined for adsorption of ammonia, pyridine, and isopropylamine on different zeolite catalysts.

zeolite	ammonia: $\Delta H/kJmol^{-1}$	pyridine: $\Delta H/kJmol^{-1}$	isopropylamine: $\Delta H/kJmol^{-1}$
H-Y	135 - 150	175 - 185	185 - 195
H-ZSM-5	150	195	230 - 245
H-[Fe]ZSM-5	145	195	—
H-[Ga]ZSM-5	150	200	—
H-M	160	180 - 200	215 - 220

kJ/mol   plateau (ii)   (n_{Si}/n_{Al})

```
200 –
        Mazzite (12)
190 –

180 –   USY

170 –
        Mordenite (16)
160 –   Erionite (3.5)
        Offretite (3.9), H-ZSM-5 (14)
150 –   Ferrierite (15), SAPO-37 (Si/Si+Al+P=0.2)

140 –
        H-Beta (10)
130 –   HY (2.4), MCM-41 (4.5)

120 –

110 –
        HX (1.25)
100 –
        HA (1)
 90 –

 80 –   LiX, LiY
        NaX, NaY, Ti-Silicalite
 70 –   KX

 60 –
        KY, RbY
 50 –   RbX, CsX
        CsY
 40 –   Silicalite
```

Fig. 10.13 Differential heats, q_{diff}, obtained for ammonia adsorption on various zeolites and mesoporous materials with different structure types and n_{Si}/n_{Al} ratios (in parenthesis) at 423 K.